Microbubble Disperse Flows about a Lifting Surface

Patrick Russell

B.Sc (Hons), M.Teach

National Centre for Maritime Engineering and Hydrodynamics

Australian Maritime College

Submitted in fulfilment of the requirements

for the degree of Doctor Of Philosophy,

University of Tasmania

June, 2020

Declarations

Authority of Access

Statement of Originality

This thesis contains no material which has been accepted for a degree or diploma by the University or any other institution, except by way of background information and as duly acknowledged in the text, and to best of my knowledge and belief no material previously published or written by another person except where due acknowledgement is made in the text of the thesis, nor does the thesis contain any material that infringes copyright.

Signed: ______________________ Date: 25 / 06 / 2020

Patrick Russell

Statement of Co-Authorship

The following people and institutions contributed to the publication of work undertaken as part of this thesis:

Candidate –	Mr Patrick Russell	University of Tasmania.
Author 1 –	Prof. Paul Brandner	University of Tasmania.
Author 2 –	Dr. Bryce Pearce	University of Tasmania.
Author 3 –	Dr. James Venning	University of Tasmania.
Author 4 –	Prof. Steve Ceccio	University of Michigan.
Author 5 –	Dr. Luka Barbaca	University of Tasmania.
Author 6 –	Dr. Dean Giosio	University of Tasmania.
Author 7 –	Mr. Guillaume Maj	YLec Consultants, France.
Author 8 –	Mr. Vivien Aumelas	YLec Consultants, France.

Contribution of work by co-authors for each paper:

Paper 1: Located in Chapter 2

Russell, P. S., Giosio, D. R., Venning, J. A., Pearce, B. W., Brandner, P. A. and Ceccio, S. L. (2016) Microbubble generation from condensation and turbulent breakup of sheet cavitation. In *Proceedings of the 31st Symposium on Naval Hydrodynamics*, pages 1–13. Office of Naval Research Science and Technology, Monterey, California, United States of America.

Conceived experiment design: Candidate, Author 1, Author 2, Author 4
Performed experiments: Candidate, Author 6
Data analysis: Candidate, Author 3, Author 6
Manuscript preparation: Candidate, Author 1, Author 2, Author 3, Author 4, Author 6

Paper 2: Located in Chapter 3

Russell, P. S., Venning, J. A., Pearce, B. W., Brandner, P. A., Giosio, D. R., Ceccio, S. L. (2018). Microbubble Disperse Flow about a Lifting Surface. In *32nd Symposium on Naval Hydrodynamics*. Office of Naval Research Science and Technology. Hamburg, Germany.

Conceived experiment design: Candidate, Author 1, Author 2, Author 4, Author 6

Performed experiments: Candidate, Author 3
Data analysis: Candidate, Author 3
Manuscript preparation: Candidate, Author 1, Author 2, Author 3

Paper 3: Located in Chapter 4

Russell, P. S., Venning, J. A., Pearce, B. W., & Brandner, P. A. (2020). Calibration of Mie scattering imaging for microbubble measurement in hydrodynamic test facilities. *Experiments in Fluids* 61(93) . https://doi.org/10.1007/s00348-020-2927-7.

Conceived experiment design: Candidate, Author 1, Author 2, Author 3
Performed experiments: Candidate
Data analysis: Candidate, Author 3
Manuscript preparation: Candidate, Author 1, Author 2, Author 3

Paper 4: Located in Chapter 5

Russell, P. S., Barbaca, L., Venning, J. A., Pearce, B. W., & Brandner, P. A. (2020). Measurement of nuclei seeding in hydrodynamic test facilities. *Experiments in Fluids*, 61(79). https://doi.org/10.1007/s00348-020-2911-2

Conceived experiment design: Candidate, Author 1, Author 2, Author 3
Performed experiments: Candidate, Author 3, Author 5
Data analysis: Candidate, Author 3
Manuscript preparation: Candidate, Author 1, Author 2, Author 3, Author 5

Paper 5: Located in Appendix 1

Russell, P. S., Giosio, D. R., Venning, J. A., Pearce, B. W., Brandner, P. A., Aumelas, V., and Maj, G., (2018). Towards real-time optical measurement of microbubble content in hydrodynamic test facilities. *In 10th Symposium on Cavitation (CAV2018)* (pp. 1056-1061).
Conceived experiment design: Candidate, Author 1, Author 2, Author 6
Performed experiments: Candidate
Data analysis: Candidate, Author 3
Contributed material component: Author 7, Author 8
Manuscript preparation: Candidate, Author 1, Author 2, Author 3, Author 6

We, the undersigned, endorse the above stated contribution of work undertaken for each of the published (or submitted) peer-reviewed manuscripts contributing to this thesis:

Signed: ____________________ Date: 25 / 06 / 2020

Mr. Patrick Russell
Candidate
National Centre for Maritime Engineering and Hydrodynamics
Australian Maritime College, University of Tasmania

Signed: ____________________ Date: 26/06/2020

Prof. Paul Brandner
Primary Supervisor
National Centre for Maritime Engineering and Hydrodynamics
Australian Maritime College, University of Tasmania

Signed: ____________________ Date: 26/06/2020

Dr. Vikram Garaniya
Head of School
National Centre for Maritime Engineering and Hydrodynamics
Australian Maritime College, University of Tasmania

Acknowledgements

The privilege of undertaking this doctorate would not have been possible without the generous support from many individuals.

I am indebted to my supervisors Prof. Paul Brandner, Dr. Bryce Pearce, and Dr. James Venning for their guidance, expertise and willingness to give of their time to support me in this research. While undertaking this research I have been fortunate in being able to work alongside some excellent researchers and would like to thank Dr. Dean Giosio, Dr. Luka Barbaca, and Mr. Matthew Khoo for their support and insight. I have also had the opportunity to meet with some international collaborators. In particular, it has been a honour to meet, and work with, Prof. Steven Ceccio, Dr. Ki-han Kim, and Dr. Sung-Eun Kim. Their willingness to sit and engage with someone who is such a small part of all the projects they are in charge of highlights that their exceptional character is in keeping with their intellect. The same is true of my supervisors and I am grateful for the opportunities they have given to me.

Many of the experiments contained in this research would not have been possible without the skill possessed by the technical staff at the Cavitation Research Laboratory. I would like to thank Mr Robert Wrigley and Mr Steven Kent for their dedication and expertise as they put in many long hours to see that these experiments could take place.

I would like to thank the two main sponsors of this research: Australia's Department of Defence - Defence Science and Technology Group (DST-G) and the support of Dr. Dev Ranmuthugala, and Dr David Clarke, and the U.S. Office of Naval Research, and in particular Dr. Ki-Han Kim (Program Officer) and Dr. Sung-Eun Kim (ONR Global).

Without hyperbole, this has been the most difficult journey of my life and I would have not have been up to the challenge without the cumulative support of my friends and family. First I would like to thank my grand-parents (Stanley and Bernice Russell, and Gordon and Amy Drake) you raised my wonderful parents to be the loving people they are. Without Timothy and Robyn Russell, and my sister Bridget Russell I would not have been up to the task. Thank you all for your inexhaustible love, support and sacrifices you have made. At this point I must mention two friends that have also been with me through my candidature, Zachary Larsen and Rhys Paul. Thank you for keeping me sane and grounded through it all.

The greatest support throughout this process has been from my wife Elizabeth. As hard as I have worked she has exceeded it with love and kindness in supporting me. You are incredible and I love you more every day. It has also been a rare gift that at the end of a day, I can explain the current challenges in my work and she has the requisite knowledge to understand the complexities involved. I am truly blessed to be wed to you.

I cannot express my gratitude to these people enough and thank God for his kindness in placing them in my life every day.

Abstract

The formation, size and concentration of microbubbles generated in the wake of a cavitating hydrofoil were investigated experimentally in a variable pressure water tunnel for several Reynolds and cavitation numbers, with and without freestream nuclei. In the absence of freestream nuclei, interactions between the cavity, the overlying boundary layer and associated interfacial effects were investigated qualitatively and quantitatively using a combination of still and high speed photography. The influence of these features on the physics of cavity breakup and condensation, and subsequent microbubble formation, were examined. Coherent spatial and temporal features of the sheet cavitation were found to be functions of both Reynolds and cavitation numbers. Long range microscopic shadowgraphy was used to measure the dense bubble populations present in the wake, and additionally implemented as a reference technique in the development of the Mie-Scattering Imaging (MSI) technique described below. For the range of microbubble sizes measured, concentrations are shown to increase with Reynolds number and reduce with decreasing cavitation number. The presence of freestream nuclei markedly alters cavity topology, and their effect on flow features and associated microbubble production was also evaluated. Wake microbubble concentrations were found to increase when low concentrations of nuclei were introduced but to then decrease with further increase in nuclei seeding. Regardless of seeding concentration, microbubble populations in the wake increased as the cavitation number was reduced. For high cavitation numbers the increase in concentration is primarily in bubbles of smaller size, whereas the increase in wake concentration at lower cavitation numbers occurs over a greater size range.

These experiments demonstrate the importance of cavitation nuclei measurement in hydrodynamic test facilities. Application of an interferometric technique known as Mie-Scattering Imaging (MSI) for the measurement of sparse nuclei seeding populations in such facilities has been developed. A separate pressure chamber, with similar optical path properties to the tunnel test section, was used to develop the technique. Monodisperse bubbles (with diameters between 30 and 150 µm) were generated by a microfluidic 'T' junction, and individual bubbles were simultaneously imaged with shadowgraphy and MSI. In development of the MSI technique, approximations from Lorenz-Mie theory were experimentally validated, and the influence of fringe uniformity and intensity for each polarisation (perpendicular or parallel) on measurement precision was investigated. Parallel polarisation was preferred for its more uniform fringe spacing despite a lower intensity. The inverse relation between fringe wavelength and bubble diameter was demonstrated at a measurement angle of 90°. The wavelength of the scattered fringe pattern is predicted using Lorentz-Mie theory and the calibration constant for fringe spacing was obtained. A practical method for the calibration of a second constant related to the imaging optics has also been developed. Using this approach the measured bubble diameters from the shadowgraphy and MSI compared to within 1 µm. The precise bubble location within the beam was measured with shadowgraphy and with this information a method for determining the size dependent measurement volume for both axisymmetric and arbitrary beam profiles was developed. Once refined, the technique was used to characterise the concentrations and range of microbubble sizes produced by a nuclei seeding system for various tunnel conditions. Nuclei concentrations between 0-24 bubbles per mL were measured and the distribution of bubble sizes was found to follow a power law for high nuclei concentrations.

Contents

List of Figures

List of Tables

Nomenclature

Symbol	**Definition**	**Unit**
α	Flow incidence angle	$^\circ$
	Light collection angle	$^\circ$
γ	Surface tension	$(\mathrm{kg} \cdot \mathrm{m})/(\mathrm{m} \cdot \mathrm{s}^2)$
λ	Wavelength	m
$\lambdabar$	Angular wavelength	$^\circ$
ν	Kinematic viscosity	m^2/s
ρ	Water density	kg/m^3
σ	Cavitation number	-
σ_{gen}	Bubble generator cavitation number	-
θ	Scattering angle	$^\circ$
ϕ/ψ	Polarisation angle	$^\circ$
χ	Mie parameter	-
A	Angular wavelength calibration constant (also C)	$^\circ\mathrm{px}^{-1}$
c	Root chord length	m
C	Angular wavelenth calibration constant (also A)	$^\circ\mathrm{px}^{-1}$
	Concentration	cm^{-3}
d	Bubble diameter	µm
d_i	Bubble diameter using Mie scattering imaging	µm
d_s	Bubble diameter using shadowgraphy	µm
d_p	Bubble diameter when in the tunnel plenum	µm
d_t	Bubble diameter when in the tunnel test section	µm
D_{px}	Distance in pixels	px
DO_2	Dissolved Oxygen content	% of saturation concentration at atmospheric pressure
E	Electromagnetic wave vector	a.u.

H	Henry's constant	atm/mol
I	Intensity value	a.u.
K	Mie scattering calibration constant	µm °
m	Refractive index ratio	-
n_a	Refractive index of air	-
n_w	Refractive index of water	-
N	Bubble concentration	cm^{-3}
p	Freestream static pressure	Pa
p_s	Saturation vessel pressure	Pa
p_p	Pressure in the plenum	Pa
p_v	Vapour pressure	Pa
p_t	Pressure in the tunnel test section	Pa
Δp_{gen}	Pressure difference between the saturation vessel and tunnel plenum	Pa
r	Bubble radius	m
Re	Reynolds number	-
Sc	Schmidt number	-
Sh	Sherwood number	-
S_1	Perpendicular polarised scatter light component	a.u.
S_2	Parallel polarised scatter light component	a.u.
U/U_t	Velocity	m/s
w	Wake width	m

Abbreviations

AMC	Australian Maritime College
CCD	Charge Coupled Device
CFD	Computational Fluid Dynamics
CRL	Cavitation Research Laboratory
CSM	Cavitation Susceptibility Meter
DSLR	Digital Single Lens Reflex (camera)
FFT	Fast Fourier Transform
GTH	Grand Tunnel Hydrodynamique
IMI	Interferometric Mie Imaging (see also MSI)
KH	Kelvin Helmholtz
LMT	Lorentz-Mie Theory
LMS	Long-Range Microscopy Shadowgraphy
MSI	Mie Scattering Imaging
PIV	Particle Imaging Velocimetry
STP	Standard Temperature and Pressure

Chapter 1

General Introduction

Oceans and waterways exhibit background bubble populations that vary greatly in size and concentration. These populations are the result of various oceanographic mechanisms including wind induced breaking waves, spilling waves and sea-spray (Blanchard and Woodcock, 1957; Chanson and Cummings, 1994; Terrill et al., 2001; Deane and Stokes, 2002; Kiger and Duncan, 2012). Such populations fluctuate with temperature, sea-state, and location (O'Hern, 1987; O'Hern et al., 1988; Gowing and Shen, 2001). While large bubbles are confined to near surface regions due to buoyancy, microbubbles can be advected to surprising depths (Gindroz, 1995). Their presence influences or controls a wide range of mechanical and chemical properties of water, including the propagation of shock and acoustic waves (Brennen, 2005), turbulence (Mazzitelli et al., 2003), the diffusion of gasses into the liquid (Yu and Ceccio, 1997), and cavitation inception and dynamics (Gindroz and Billet (1998); Brennen (2014)). Consequently their measurement is of interest in many naval hydrodynamic applications.

Surface ships are also a profuse source of bubbles. Breaking bow waves (Waniewski et al., 2000) and turbulence from the hull (Masnadi et al., 2019) ingest large volumes of air that becomes dispersed about the wider flow field. Cavitation from propulsion and control equipment may also generate dense populations in their wake through diffusion and liberation of dissolved gas (Yu and Ceccio, 1997). These populations are subsequently modulated by turbulence produced by the hull and other control surfaces (Li et al., 2019). Upon a bubble splitting, the number and size of products is stochastic (Qian et al., 2006), however the rate of turbulence dissipation can be used to draw generalised trends (Vejražka et al., 2018). The coalescence of bubbles is dependent on their number and size, but also chemistry, as surfactants and particles may coat the bubble surface (Ata, 2008). These flows are then challenging to study due to the many length scales, time scales and phenomena involved. Insights tying these together such as the Hinze scale, below which the restorative force of surface tension of a bubble exceeds the destructive forces available, aid in the development of computational models (Deane and Stokes, 2002). Extensive numerical work has been conducted to model these processes in a marine context (Qin et al., 2003a; Hsiao and Chahine, 2005; Hsiao et al., 2016; Qian et al., 2006; Ma et al., 2017; Hsiao et al., 2017, 2019). However, while investigations predicting bubble populations for an entire ship have been conducted (Carrica et al., 1999; Castro and Carrica, 2013; Castro et al., 2014), they are certainly not yet routine.

The role of free stream nuclei in cavitation continues to be of significant interest in cavitation research as indicated by the following selection of publications from the last three decades (Meyer et al., 1992; Ran and Katz, 1994; Liu and Brennen, 1998; Gindroz and Billet, 1998; Hsiao and Chahine, 2005; Van Rijsbergen and Van Terwisga, 2011; Nagaya et al., 2011; Brandner et al., 2015; Mørch, 2015; Zhang et al., 2016; Park and Seong, 2017). As a part of this extensive activity there has also been publication also on nuclei measurement techniques, both optical (Lebrun et al., 2011; Ebert et al., 2016), mechanical (Khoo et al., 2016), and acoustic (Chahine et al., 2001; Chahine and Kalumuck, 2003), with a number of studies making comparisons between the various techniques (Billet and Gates, 1981; Katz et al., 1984; Mées et al., 2010). As reflected on by Billet (1986), the volume of literature on the topic indicates the complexity of the problem, largely due to its multi-phase and inherently statistical nature. From this it is clear that each of these measurement techniques have their advantages and disadvantages. A summary of where key techniques are applicable for different settings is discussed by Brandner (2018) and shown in Fig. 1.1.

For the background population ever present in cavitation test facilities (red in fig 1.1), bubbles are less than few wavelengths of visible light in diameter and sparsely dispersed so that conventional optical techniques are impractical. Alternative methods utilising mechanical or acoustic principles such as a cavitation susceptibility meter (CSM) have been developed for application in this region. These devices have their own limitations, for CSM measurements the rate of bubble activations can saturate so that individual events cannot be distinguished (Khoo et al., 2016). In addition, bubbles larger than 50 µm are activated by pressures approaching vapour pressure, limiting the precision of diameter measurements in this range. In contrast, acoustic methods are able to measure bubbles larger in size (Chahine and Kalumuck, 2003; Duraiswami et al., 1998), and have previously been employed to measure oceanographic bubble populations (Breitz and Medwin, 1989). In AMC tunnel flows involving developed or attached cavitation the free-stream nuclei content has been found to not have a significant role Holl and Carroll (1981); Lecoffre (1999). In the case of unsteady/cloud cavitation about a sphere, nucleation of the next cavity cycle was observed to stem from remnant bubbles from the previously shed cavity (de Graaf et al., 2017). However in some instances, e.g. flows involving Tip Vortex Cavitation (TVC), these background populations play an active role in the cavitation inception and related dynamics (Gowing et al., 1995; Khoo et al., 2017, 2019).

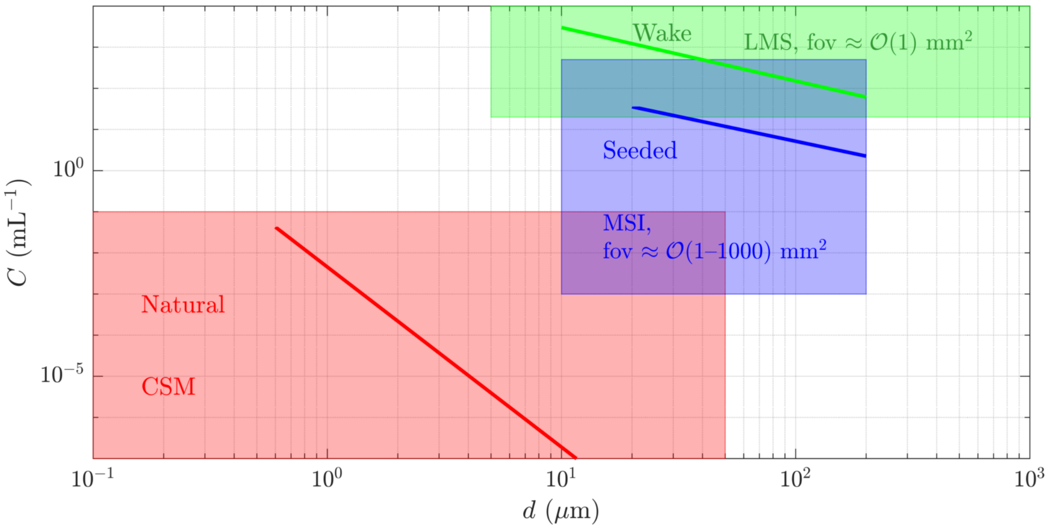

Figure 1.1: Nuclei/microbubble cumulative histograms from various experiments in the University of Tasmania cavitation tunnel measured using three different methods depending on the population size/critical pressure and concentration range. A Cavitation Susceptibility Metre (CSM), Mie Scattering Imaging (MSI), and Long-range Microscopic Shadowgraphy (LMS). The shaded regions show the application range of each technique. The CSM has been used for measurement of the tunnel natural or background nuclei population, MSI for seeded nuclei populations and LMS for microbubble populations generated from collapse and condensation of large-scale sheet and cloud cavitation. These demonstrate the large range of sizes/critical pressures and concentrations in microbubble disperse flows and the need for several techniques for their measurement. (Brandner, 2018) (Figure image and caption reproduced with permission from the Author).

For the highest concentrations in Fig. 1.1 (green), populations are typical of bubbles found in the far wake of ships or from cavitating propulsors and other lift producing surfaces. Limited experimental surveys of bubble distributions generated by cavitation show typical concentrations are on the order of 10^1 to 10^4 bubbles per cm^3 (Maeda, 1991; Yu and Ceccio, 1997; De Graaf et al., 2014). The dominant population generated are on the order of 10-100 µm in size. When measuring over a limited range of sizes, bubble concentrations are typically reported in terms of their number per standard volume, (typically N/cm^3), as in some settings they may not be representative of the total void fraction. Populations in this region afford measurement with long-range microscopic shadowgraphy (LMS), a non-intrusive technique capable of measuring the high concentrations present, though with a field-of-view (FOV) of $\mathcal{O}$(1mm) giving essentially a point measurement.

The intermediate population (blue in fig 1.1) characterises flows upstream of surface ship propulsors which can also be modelled in some hydrodynamic facilities with artificial seeding capabilities (Lecoffre et al., 1987; Brandner et al., 2006, 2007). Non-intrusive interferometric optical methods have been developed that are capable of measuring within this diameter and concentration range. While the most developed of these methods, Laser Doppler and Phase Doppler, are essentially point measurement techniques (Albrecht et al., 2013), some techniques are capable of measurement over a wide field of view (Damaschke et al., 2002; Ebert, 2015). These populations can result in travelling bubble cavitation (Ceccio and Brennen, 1991; Brennen, 2002), and their presence has been shown to modify the appearance and characteristics of cavitation dynamics (Briançon-Marjollet et al., 1990; Brennen, 2014).

This research is concerned with experimental measurements of microbubbles and cavitation in the two uppermost regions of figure 1. Both the generation of bubbles by cavitation and the influence of microbubbles on cavitation is explored. In addition, bubble measurement techniques are extended, and then applied to rigorously characterise the range of seeding produced in the test section of the University of Tasmania - Australian Maritime College cavitation tunnel.

The objectives of the present research are as follows:

- To investigate the physics of microbubble generation from condensation/collapse of macroscopic cavities.
- Quantify microbubble populations produced in the wake of a cavitating lifting surface and how these populations are dispersed.
- Investigate the effect of free stream nuclei on cavitation dynamics and subsequent bubble generation.
- To validate and implement a non-intrusive optical technique for the measurement of seeded microbubble cavitation nuclei in a cavitation tunnel for semi-sparse bubble populations.

The research questions answered by this research are:

- How do the Reynolds and cavitation numbers influence the development of sheet cavitation geometry and topography, and subsequent breakup and microbubble generation?
- How does free-stream seeding concentration affect cavity geometry and topography, and subsequent microbubble generation?
- Can off-the-shelf imaging components be used to produce a rigorously calibrated interferometric microbubble measurements system suitable to measure semi-sparse populations in a cavitation water tunnel or other hydrodynamic test facilities?
- With such an interferometric method, what seeding populations are produced in the CRL hydrodynamic test facilities with changing tunnel operating conditions?

The individual chapters presented in this thesis are written in article form and are either published in full-length refereed conference proceedings, or submitted for publication in the journal of Experiments in Fluids. A short form refereed conference paper in supplement to the main body of work has been attached as an appendix. The publishing details for each article are given at the start of each chapter. An outline of the chapters, and their contribution to research objectives, are stated below:

Chapter 2: The formation, size and concentration of microbubbles generated in the wake of stable sheet cavitation about a hydrofoil, without the activation of free-stream nuclei, are investigated experimentally for several Reynolds and cavitation numbers. Interactions between the cavity, overlying boundary layer, and associated interfacial effects are investigated qualitatively and quantitatively. Their impact on the physics of cavity breakup and condensation are discussed in relation to the subsequent microbubble formation. Coherent spatial and temporal features of the sheet cavitation are shown to be functions of the Reynolds and cavitation numbers, and have been related to the microbubble populations measured in the wake at multiple downstream locations.

Chapter 3: The effect of free-stream nuclei on sheet cavitation and subsequent microbubble generation is investigated for a variety of nuclei seeding concentrations and cavitation numbers. The dispersion of microbubbles generated by the cavity and travelling bubble cavitation were measured across the transverse wake profile. The influence of cavity features on the observed wake populations and bubble generation physics is investigated.

During testing limitations of the optical measurement methods were identified. For LMS, the high degree of magnification required to measure 10µm bubbles limited the maximum size measurable so that multiple magnifications would be required to resolve the full range of bubbles sizes present in the wake. In addition, calibration methods of the interferometric technique for large scale test facilities were not able to be rigorously validated for standard multi-element lenses and imaging components.

Chapter 4: Simultaneous single bubble measurements using LMS and MSI from a mono-disperse bubble generator were used to meticulously validate the sizing of bubbles, and the measurement volume, for the MSI technique. A discussion of the optimisation and selection of measurement parameters is presented from Lorentz-Mie scattering theory and validated experimentally. This experiment enabled the development of a calibration procedure suitable for use in large test facilities with off-the-shelf lenses and cameras.

Chapter 5: The MSI measurement technique developed in Chapter 4 is implemented in the cavitation tunnel at the University of Tasmania CRL to measure the range of microbubble nuclei produced by the facilities seeding system. The size and concentration of nuclei are measured for changing tunnel operating conditions to establish the effect of tunnel velocity and pressure on the seeding distributions and the range of concentrations able to be produced for testing.

Chapter 2

Microbubble Generation from Condensation and Turbulent Breakup of Sheet Cavitation

This chapter is presented in article form, and has been published in the proceedings of the *31st Symposium on Naval Hydrodynamics*.

The citation for the paper is:

Russell, P. S., Giosio, D. R., Venning, J. A., Pearce, B. W., Brandner, P. A. and Ceccio, S. L. (2016) Microbubble generation from condensation and turbulent breakup of sheet cavitation. In *Proceedings of the 31st Symposium on Naval Hydrodynamics*, pages 1–13. Office of Naval Research Science and Technology, Monterey, California, United States of America.

2.1 Abstract

The formation, size and concentration of microbubbles generated in the wake of a cavitating hydrofoil are investigated experimentally for several Reynolds and cavitation numbers. The present work is restricted to bubble generation from stable sheet cavitation. In this context 'stable' describes a cavity which remains attached and covers a nominally constant area of the hydrofoil, free from full span shedding cycles that cause the stream-wise length to fluctuate. Interactions between the cavity, the overlying boundary layer and associated interfacial effects are investigated qualitatively and quantitatively using high-resolution and high-speed photography. The physics of cavity breakup and condensation

and microbubble formation are also investigated using high-speed photography. Size and concentration of microbubble populations are measured in the far wake using diffused laser shadowgraphy. The optical setup of the shadowgraphy permitted microbubbles in the size range of 5 to 300 µm to be resolved. Coherent spatial and temporal features of the sheet cavitation are shown to be functions of both Reynolds and cavitation numbers. For the range of microbubble sizes measured, concentrations are shown to increase with Reynolds number and reduce with decreasing cavitation number. In contrast, void fraction increases with decreasing cavitation number indicating a greater production of larger diameter bubbles.

2.2 Introduction

Dispersed bubbly flows generated or modulated by ships and submarines may persist for a long period of time following the passing of a vessel. In addition to background populations, ships are prolific sources of polydisperse bubble populations due to the significant surface disturbances and turbulence they generate. Considerable volumes of air are ingested and dispersed about the hull and by the propulsion and control equipment. Various mechanisms are involved including plunging jets and captured air volumes generated by breaking waves as described by Castro et al. (2014), while surface turbulence may also be sufficient for the hull boundary layer to entrain air (Washuta et al., 2016; Kim et al., 2014). Lifting surfaces are also of interest here in regards to cavitation occurrence and the consequent contribution to microbubble generation (Yu and Ceccio, 1997). New insights into the dynamics of developed cavitation are being gained both experimentally (Brandner et al., 2010a; Ganesh et al., 2014), and numerically (Gnanaskandan and Mahesh, 2014), however, the mechanisms by which cavitating flows generate microbubbles remain largely to be investigated.

As the techniques advance, Computational Fluid Dynamics (CFD) is being used to model fluid flows of increasing complexity, including in the area of turbulent multiphase flow prediction (Balachandar and Eaton, 2010; Fox, 2012). Recent numerical work specifically on turbulent cavitating flows has been reported by Gnanaskandan and Mahesh (2015). These numerical techniques all involve some use of modelling, particularly at small scales, so the flow physics is only captured accurately to varying degrees. While CFD provides valuable detailed full field information, careful comparison with experimental data is required to ensure fidelity. In many aspects numerical techniques have currently progressed ahead of available experimental data.

The numerical calculation of the full flow field about cavitating hydrofoils and propellers has been developing, in particular since the early 1990's, with ongoing interest in the topic (e.g. Huang et al., 2013; Ji et al., 2013, 2015). Qin et al. (2003a,b) reported on the unsteady turbulent far wake behind a cavitating hydrofoil. While gross flow effects were adequately simulated, it was found that only when the effect of dissolved gas content was included in the numerical model, local quantities such as the wake velocity distributions were captured accurately. This was also the case in an earlier study by Kjeldsen et al. (2000), where deviations in the numerical flow prediction downstream of a foil were linked to dissolved gas content in the wake.

There are limited reported experimental surveys of the bubble distribution within the wake of a cavitating hydrofoil. Maeda (1991) investigated the microbubble population within cloud cavitation occurring about a NACA 0015 hydrofoil (Reynolds number (Re) – $6.2{\times}10^5$, cavitation number (σ) – 1.96, incidence (α) – 8.36° and a dissolved oxygen content of 10 to 15% of saturation at atmospheric pressure). The dominant bubble size was found to be of the order of 10 to 20 µm. Yu and Ceccio (1997) reported similar size distributions at a single measurement point within the turbulent wake of two cavitating wedges at $Re = 1.1 \times 10^5$ and σ between 1.5 and 1.6, for an oxygen content of 27%. More recently, De Graaf et al. (2014) performed a spatial survey in the wake of a modified NACA 63A015 hydrofoil at a single operating condition of $Re = 0.5 \times 10^6$, $\sigma = 0.37$, and $\alpha = 3.5°$, and found the dominant bubble size to vary in the spanwise and streamwise (at mid-span) directions between 25 and 40 µm.

A related study on the effect of freestream velocity on the bubble size distribution within the wake of a non-cavitating, ventilated NACA 0015 hydrofoil was reported by Karn et al. (2015). Two bubble size 'modes' were observed, the more dominant being of the order of 300 µm, while the second mode was around 620 µm. As the Re was varied from 2.4×10^5 to 8.1×10^5 the probability density function of the first mode was found to increase while the second decreased. The Sauter Mean Diameter — the average bubble size calculated using the ratio of bubble volume to surface area rather than the arithmetic mean diameter — was also shown to decrease with increasing Re. The local physics of bubble breakup and coalescence is complex (Liao and Lucas, 2009, 2010) and the relative contributions of these processes to resultant bubble distributions in the wake of cavitating or ventilated bodies is a focus of current research.

Microbubbles respond dynamically to the changing pressure field about a hydrofoil resulting in an uneven diffusion during advection which remains to be fully understood. Not only is the size of the bubble important but the velocity of the bubble relative to that of the surrounding fluid. Given a sufficient velocity difference smaller bubbles can grow from their initial radius by an order of magnitude (Smith and Peterson, 1984). This emphasises the importance of eliminating free stream microbubble content when investigating wake bubble size distributions produced from cavitation. As discussed in the following section the facility used in the present study has the capability for control of the dissolved gas content and removal of all free bubbles from the incoming freestream.

The aim of the present study is to gain a more detailed understanding of sheet cavity formation and breakup physics, including the resultant microbubble population in the downstream wake, for a range of flow conditions. The findings, as part of an ongoing study, are expected to serve as data for comparison and validation of numerical models for the prediction of these types of flows.

2.3 Experiment Details

Experiments were carried out in the Cavitation Research Laboratory (CRL) variable pressure water tunnel at the University of Tasmania. A schematic of the facility architecture with a description of the main features is shown in Figure 2.1. The tunnel test section is 0.6 m square by 2.6 m long in which the operating velocity and pressure ranges are 2 to 12 m/s and 4 to 400 kPa absolute, respectively. The tunnel volume is 365 m^3, which is filled with demineralised water (conductivity of order 1 µS/cm).

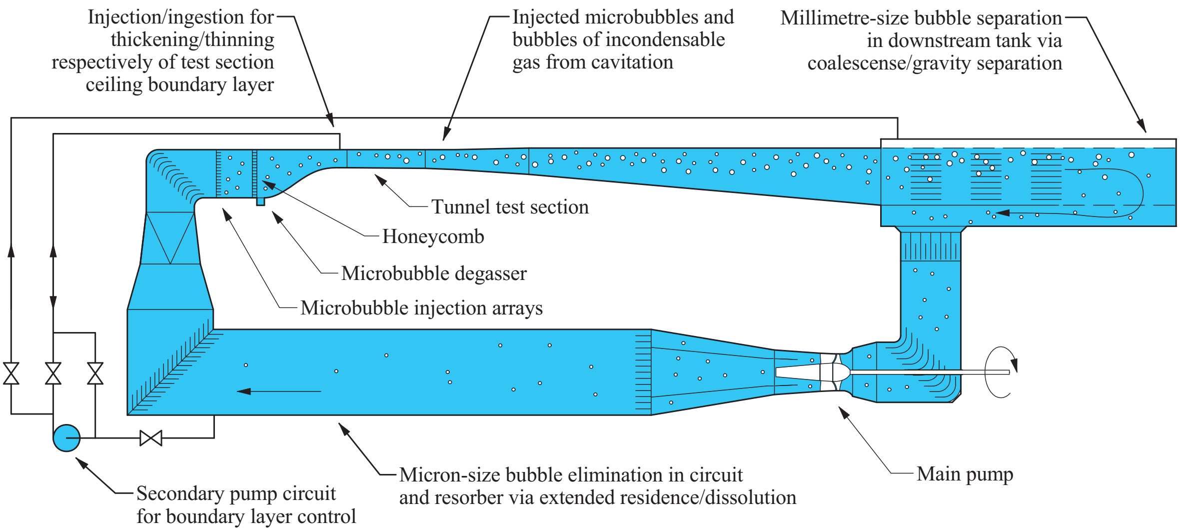

Figure 2.1: Schematic of the CRL water tunnel circuit. The facility is designed for continuous injection and separation of incondensable gas and cavitation nuclei via processes of coalescence/gravity separation of bubbles greater than about 100 µm in a downstream tank and dissolution with extended residence in the lower limb or resorber.

The tunnel has ancillary systems for rapid degassing and for continuous injection and removal of nuclei and large volumes of incondensable gas. The test section velocity is measured from one of two (low and high range) Siemens Sitrans P differential pressure transducers models 7MF4433-1DA02-2AB1-Z and 7MF4433-1FA02-2AB1-Z (measuring the calibrated contraction differential pressure) with estimated precision of 0.007 m/s and 0.018 m/s, respectively. The velocity and pressure in the test section are controlled to maintain a constant Re and σ. The test section velocity is spatially uniform to within $\pm 0.5\%$, has temporal variations of less than 0.2%, and the free stream turbulent intensity is about 0.5%. Detailed descriptions of the facility are given in Brandner et al. (2006,

2007) and Doolan et al. (2013).

An anodised aluminium hydrofoil was mounted on the test section ceiling centreline, as shown in Figure 2.2, 1.15 m downstream from the entrance. The hydrofoil geometry consisted of an elliptical planform, with a span of 200 mm, a base-chord length (i.e. the chord length at the hydrofoil/window junction) of 120 mm, and a modified NACA 63A015 profile. The profile modification involved an increase of the trailing edge thickness (see Figure 2.3) to enable practical manufacture of the scaled model and to reduce susceptibility to in-service trailing edge damage. The modified profile was achieved by the addition of $0.00385x$ to the standard profile, where x is the chord-wise distance from the leading edge.

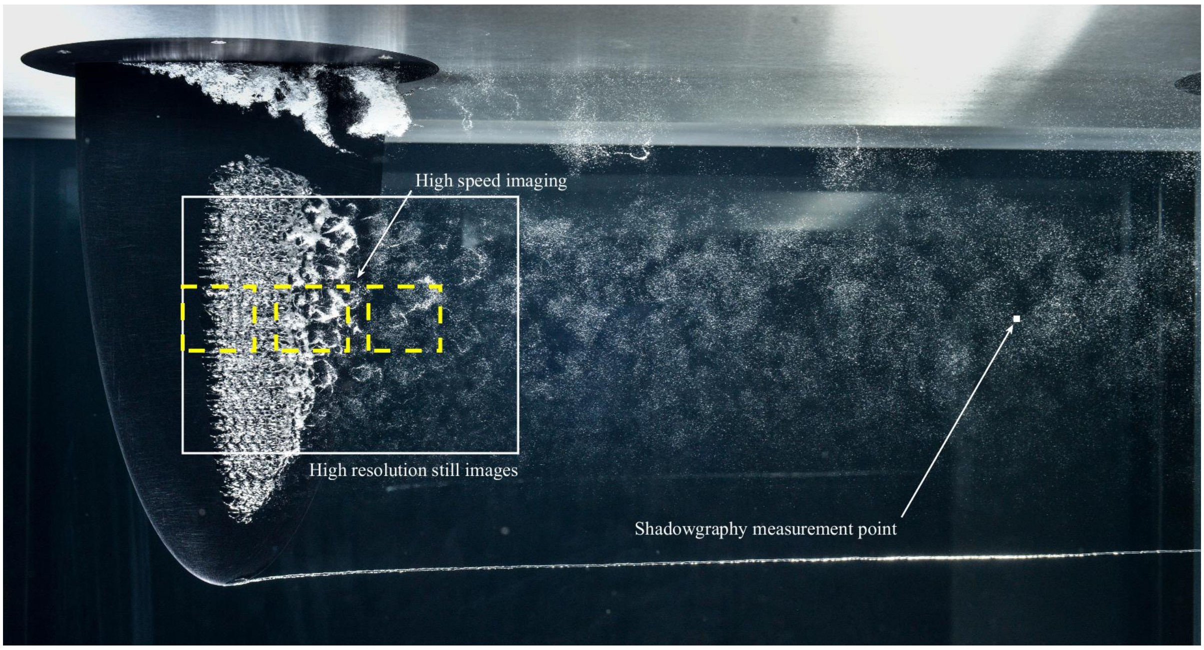

Figure 2.2: Elliptical planform modified NACA 63A015 section hydrofoil mounted in the CRL water tunnel. The location of the shadowgraphy measurement point is at mid-span, 2.5 × the root chord length downstream from mid-chord. The field of view for the high-resolution stills is indicated by the solid white boundary, while high-speed imaging field of views are given by the dashed yellow boundaries.

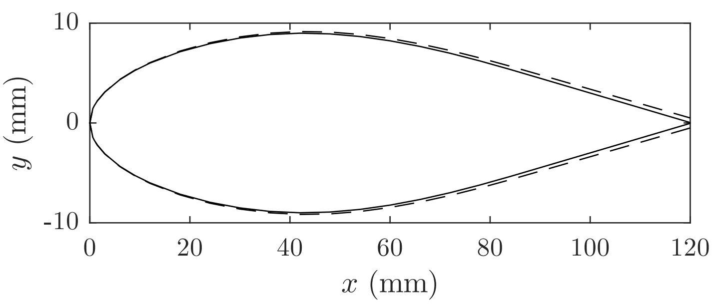

Figure 2.3: Comparison of a standard (solid) and modified (dashed) NACA 63A015 section. The modification thickens the profile gradually from the leading edge through to a maximum at the trailing edge.

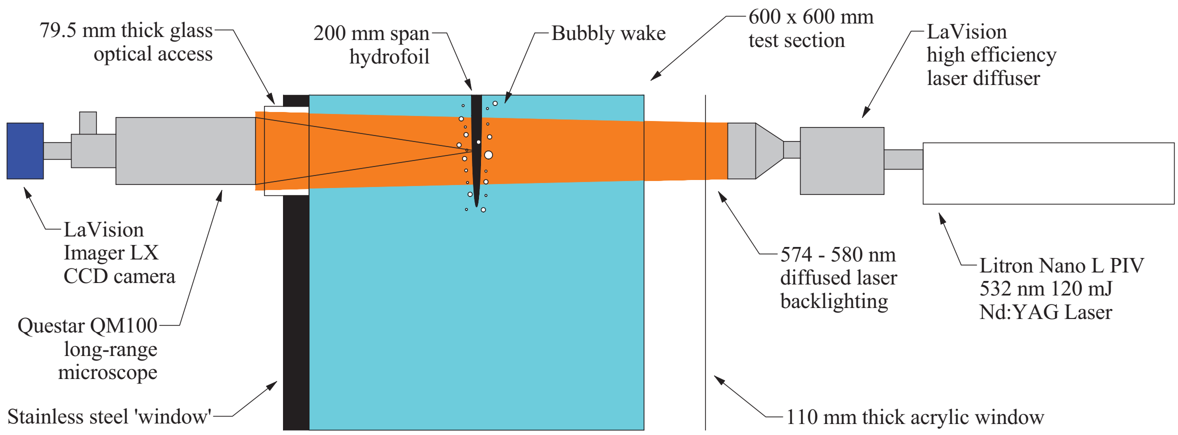

Figure 2.4: Schematic of experimental set-up for diffused laser shadowgraphy measurement in the wake of a hydrofoil in the CRL water tunnel test section (transverse view looking upstream).

High-resolution (36.3 megapixel) still photographs were captured using a Nikon D800E DSLR with a Nikon AF-S Micro Nikkor 105 mm 1:2.8G ED lens. Illumination was provided by two simultaneously triggered stroboscopes, a Drello 3018 scope with 4037 flashlamp and a Drello 1018 scope with 4040 flashlamp. High-speed photographic images were acquired at 14,000 frames per second using a LaVision HighSpeedStar8 CMOS 12-bit 1 megapixel camera with a Nikon AF Nikkor 50 mm 1:1.4D lens. A combination of high powered LED light units including 2 custom-made lamps (based on the Cree XLamp CXA3050 LED) and a Veritas Constellation 120 W light source were used to obtain sufficient illumination.

Shadowgraph images were acquired using a LaVision Imager LX 12-bit 29M camera in combination with a Questar QM100 long-range microscope. The camera CCD sensor size is 6600 × 4400 pixels. The long-range microscope was coupled to the camera using a 3× Barlow lens giving a field of view of 1917 µm × 1279 µm with a spatial resolution of 0.29 µm/px. This optical set-up allows a range of bubble sizes from 5 to 300 µm to be measured with a 5 µm bubble being imaged with 17 pixels across the diameter. The lower size is limited by the spatial resolution and the diffraction limit while the upper size is limited by the field of view and depth of field. One thousand images per data point were acquired based on the number required for converged statistics found from an earlier study (Brandner et al., 2010b).

To improve the optical access the 110 mm acrylic test section side window was replaced by a stainless steel window fitted with a 160 mm diameter, 79.5 mm thick, glass port. Backlit illumination was provided by a Litron Nano L PIV Nd:YAG laser (532 nm, 120 mJ, 20 Hz) guided through a LaVision high efficiency diffuser using a fluorescent dye plate. A cone of diffused light was produced which emitted pulses in the wavelength range 574 to 580 nm and of 20 ns duration when excited by 5 ns, 532 nm laser pulses. Both the camera and diffuser were affixed to Linos optical rails and mounted on Isel 3-axis (790 mm) linear traverses to allow accurate alignment and positioning. The laser and camera were triggered from a programmable timing unit and the acquisition and bubble sizing analysis was carried out using LaVision DaVis Version 8.3.0.

All data were obtained at a fixed incidence of 3.5° and at several chord-based Reynolds numbers, $Re = Uc/\nu$ (where U is the free stream velocity, c the root-chord length and ν the kinematic viscosity), and cavitation numbers, $\sigma = (p - p_v)/(^1\!/\!_2\rho U^2)$ (where p is the freestream static pressure at the mid-span of the hydrofoil, p_v the vapour pressure, and ρ the density of the fluid). The dissolved oxygen content was maintained between 25–30% of the concentration for saturated water at atmospheric pressure for all test conditions.

2.4 Results

Cavity geometry and topography

A schematic representation of cavity topology is presented in Figure 2.6, and a set of high-resolution photographs of cavitation development about the hydrofoil at $\alpha = 3.5°$ for a range of Re and σ values are presented in Figure 2.5. For $Re = 1.05 \times 10^6$, inception occurs just above $\sigma = 0.35$ and this value was observed to increase slightly with increasing Re. It was found that a cavity could not be sustained at $\sigma = 0.35$ for $Re < 1.05 \times 10^6$.

The cavity length (streamwise extent) and width (spanwise extent) increase with decreasing σ and also with increasing Re. Although not systematically investigated, the cavity width extends to the hydrofoil tip for sufficiently low σ and/or high Re. The effect of Re on cavity length is greatest for the higher σ values, as shown in Figure 2.5. Photographs acquired for a large range of Re values (See Appendix B) suggest that the cavity length tends to converge with an increasing Re and/or a decreasing σ. A similar trend is also observed for the cavity leading edge that moves upstream with decreasing σ and increasing Re. The effect of Re increase from 0.6×10^6 to 1.5×10^6 for $\alpha = 3.5°$ and $\sigma = 0.25$ on the cavity geometry and topography may be seen from the cropped photographs, with a constant field of view, shown in Figure 2.7. A direct comparison of photographs for the largest and smallest Re values is also shown in Figure 2.8, with the same magnification. The leading-edge movement between these Re values is about 10 mm, or 10% of the local chord.

Length scales of cavity topographical features generally change significantly with Re as is evident from the photographs shown in Figures 2.5 to 2.8. Despite these changes, the overall cavity physics are similar. The cavity leading edge is composed of laminar cells resulting from a complex interaction between the separating unstable laminar boundary layer and interfacial effects at the liquid-gas-solid juncture at cavity detachment. The occurrence of these leading edge cells on sheet and cloud cavitation have been reported on by e.g. Leger et al. (1998) and Brandner et al. (2010a).

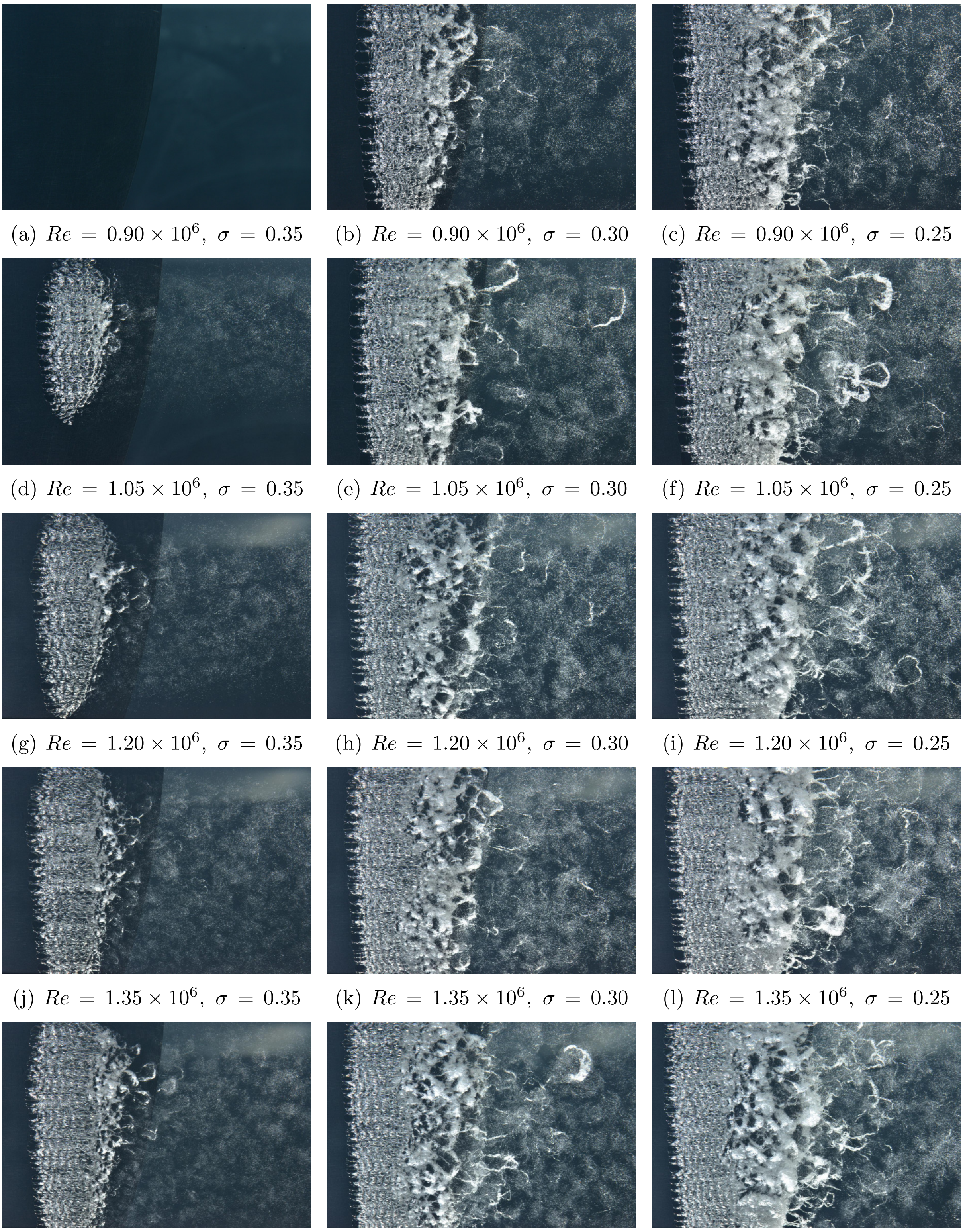

(a) $Re = 0.90 \times 10^6,\ \sigma = 0.35$ (b) $Re = 0.90 \times 10^6,\ \sigma = 0.30$ (c) $Re = 0.90 \times 10^6,\ \sigma = 0.25$

(d) $Re = 1.05 \times 10^6,\ \sigma = 0.35$ (e) $Re = 1.05 \times 10^6,\ \sigma = 0.30$ (f) $Re = 1.05 \times 10^6,\ \sigma = 0.25$

(g) $Re = 1.20 \times 10^6,\ \sigma = 0.35$ (h) $Re = 1.20 \times 10^6,\ \sigma = 0.30$ (i) $Re = 1.20 \times 10^6,\ \sigma = 0.25$

(j) $Re = 1.35 \times 10^6,\ \sigma = 0.35$ (k) $Re = 1.35 \times 10^6,\ \sigma = 0.30$ (l) $Re = 1.35 \times 10^6,\ \sigma = 0.25$

(m) $Re = 1.50 \times 10^6,\ \sigma = 0.35$ (n) $Re = 1.50 \times 10^6,\ \sigma = 0.30$ (o) $Re = 1.50 \times 10^6,\ \sigma = 0.25$

Figure 2.5: High-resolution photography of attached sheet cavitation on a modified NACA 63A015 section elliptical planform hydrofoil for various operating conditions. Flow is from left to right.

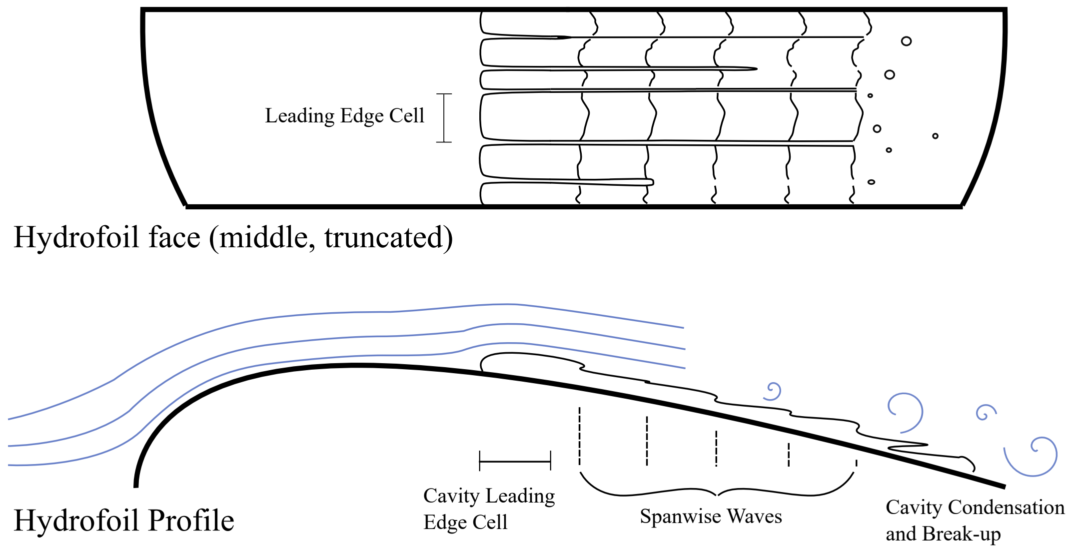

Figure 2.6: A schematic representation of the cavity is presented with key topological features identified.

Spanwise waves on the cavity surface in the wake of each cell are evident in the photographs. These are due to the Kelvin-Helmholtz (KH) instability in the overlying boundary layer (Brandner et al., 2010a; de Graaf et al., 2017). Spanwise discontinuities or edge effects in the surface waves corresponding with the divots separating the cells show these to induce three dimensional effects on the KH waves. The waves persist to the cavity trailing edge and drive coherent breakup and vortical cavity formation of the same length scale as the leading-edge cells. With downstream advection and condensation, these cavitating hairpin shaped vortices reduce in volume and ultimately break up into microbubbles of incondensable gas in the far wake.

From the high resolution photographs, it can be seen qualitatively that the length and width of the leading edge cells decrease with increasing Re. The wavelength of the KH waves also decreases with increasing Re (Figure 2.8). From Figure 2.8, it can be seen that the continuous cavity length is similar for each Re but the breakup region is much longer and the number and volume of shed cavitating vortices is much greater for the higher Re case. The vortices also persist much further downstream for the higher Re case before eventual condensation and breakup into microbubbles. Perhaps most significant is the difference in size and concentration of the generated microbubbles with the change in Re. At the low Re, low concentrations of apparently large bubbles are generated in comparison with the high Re case where much higher concentrations of bubbles are generated with a greater size distribution. The geometric and topographical features discussed here qualitatively are further analysed quantitatively below using data derived from the high-resolution photography, high-speed photography and the wake shadowgraphy.

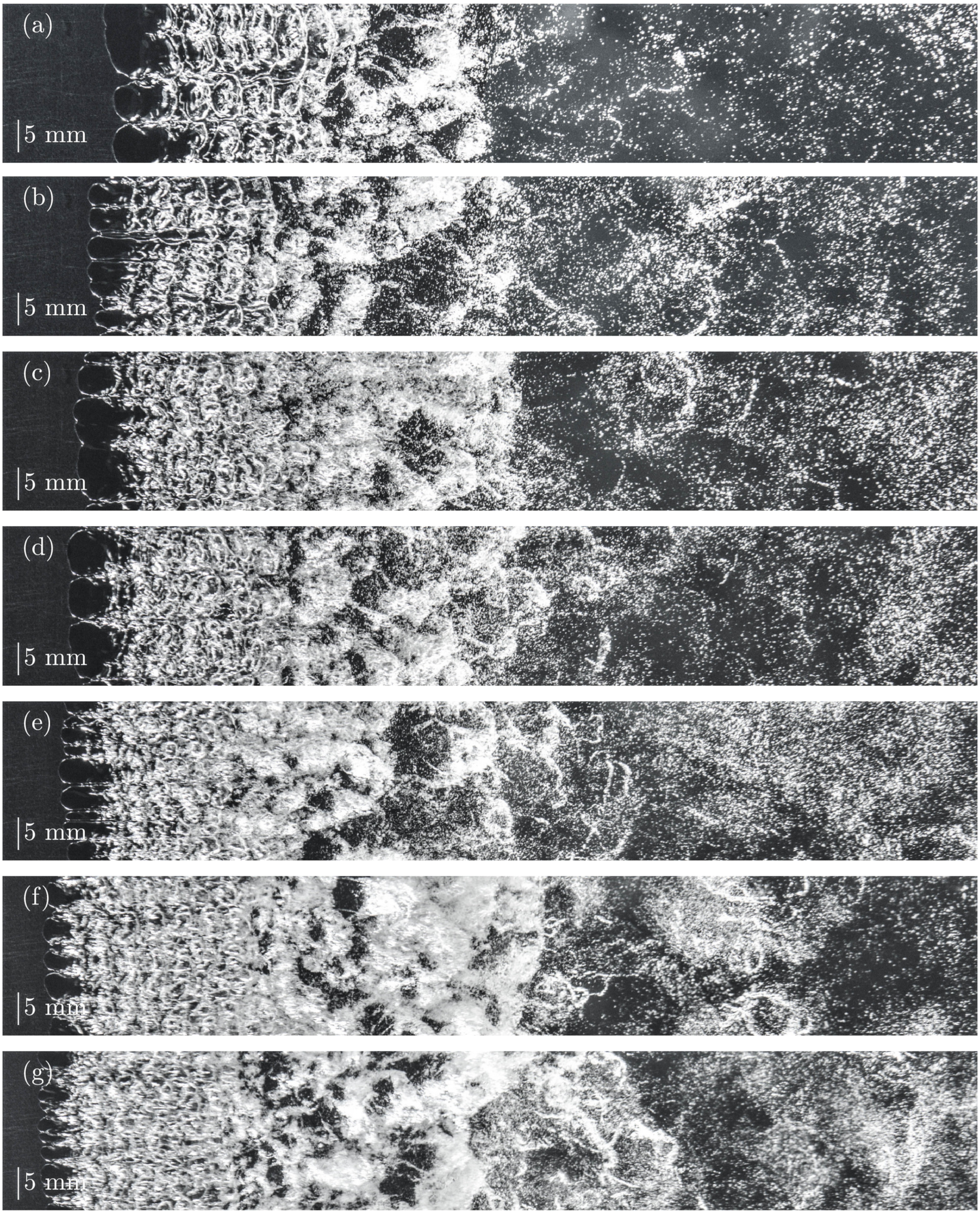

Figure 2.7: High-resolution photography of the variation of cavity leading-edge geometry as a function of Re. All photographs are at $\sigma = 0.25$. (a) $Re = 0.6 \times 10^6$, (b) $Re = 0.7 \times 10^6$, (c) $Re = 0.8 \times 10^6$, (d) $Re = 0.9 \times 10^6$, (e) $Re = 1.05 \times 10^6$, (f) $Re = 1.3 \times 10^6$, and (g) $Re = 1.5 \times 10^6$.

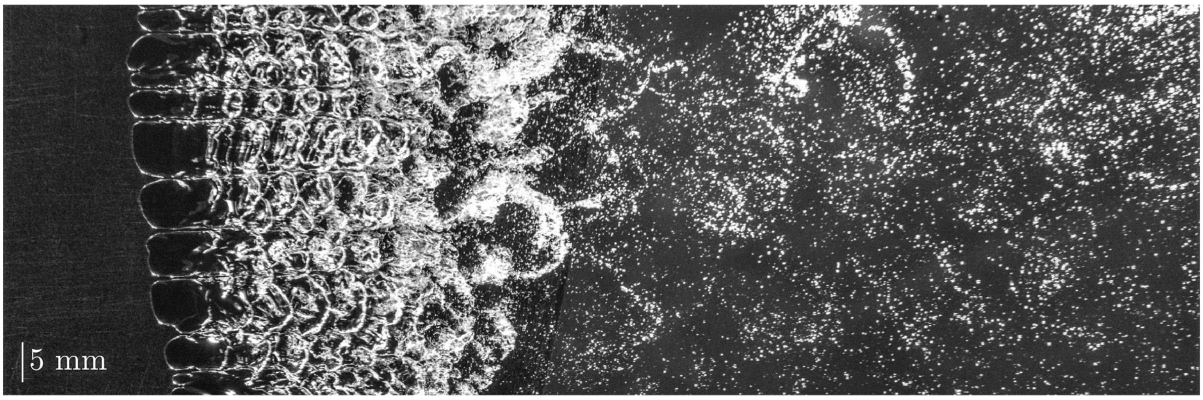

(a) $Re = 0.6 \times 10^6$, $\sigma = 0.25$

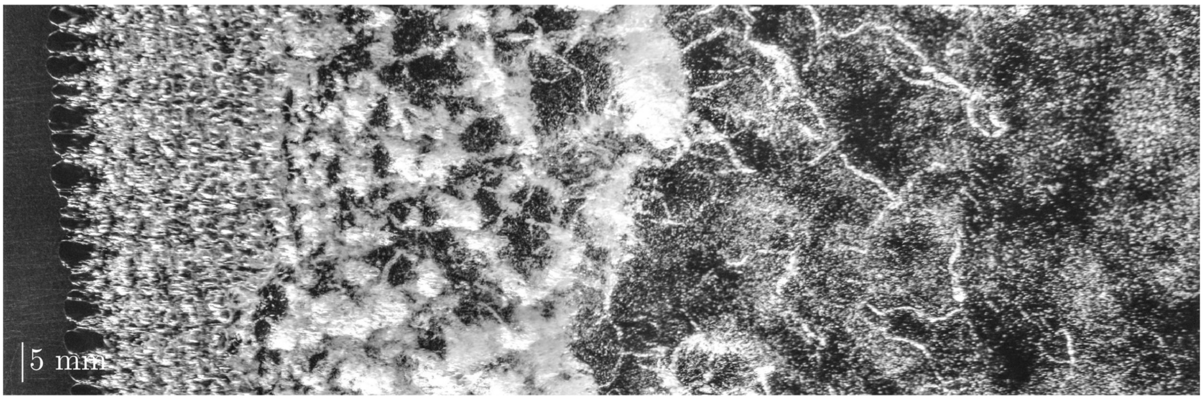

(b) $Re = 1.5 \times 10^6$, $\sigma = 0.25$

Figure 2.8: Comparison of two photographs showing the effect of Re on cell size and wavelength. The σ is constant between the two cases. In the top image, the average cell span is 5.1 mm, the average cell length is 5.1 mm, and the average wavelength is 4.7 mm. In the bottom image at higher Re, the average cell span is 3.4 mm, the cell length is 5.1 mm, and the wavelength is 3.4 mm.

Scaling and dynamic behaviour of cavity topographical features

The variation of the leading-edge cell mean width, s, with Re and σ has been derived from the high-resolution photography. Cell widths were measured using peak detection within intensity profiles extracted along the laminar region of the cavity leading edge. Ten images were used to derive s for each combination of Re and σ photographed. The variation of s as a function of Re, with σ as a parameter, is shown in Figure 2.9. As noted above, a cavity can be sustained for a lower Re with decreasing σ. The data for the two lowest σ values have an initial increase in s to a maximum at a Re of about 0.8×10^6. With increasing Re beyond these maxima s monotonically decreases for all σ values converging to about 3.2 mm for $Re > 1.3 \times 10^6$. There is insufficient data to determine whether σ has an effect on s. The peak at $Re = 0.8 \times 10^6$ is not supported by visual observation of images in Appendix B, indicating improvement could be made to detection algorithm.

Examination of the high-speed photography shows the cells to be in a state of dynamic equilibrium undergoing constant cycles of growth and division. Wider cells preferentially grow wider with smaller neighbouring cells reducing in width ultimately being washed

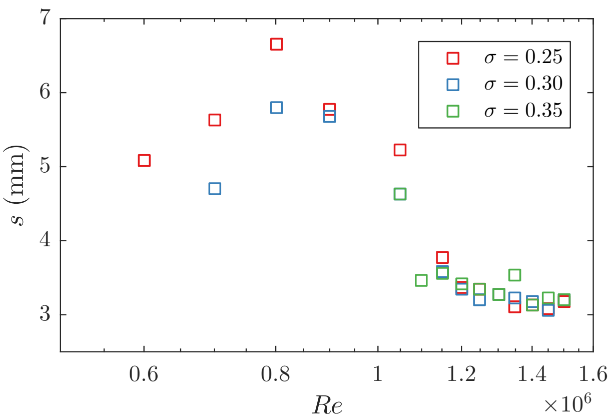

Figure 2.9: Average span of the cavity leading-edge cells, s, as a function of Re, with σ as a parameter denoted by symbol colour.

downstream within the divot or inter-cellular secondary flow.

Autocorrelation was used to find the most probable streamwise length of periodic features, which in this case is the wavelength of the surface features. The maximum non-zero peak of the autocorrelation function was recorded for each row in each image, then compiled to form a histogram. Histograms for the two photographs shown in Figure 2.8 are given in Figure 2.10. Two peaks are evident in each case. The peak near 4 mm corresponds to the wavelength of the cavity surface waves, which may be confirmed by inspection of the photographs (Figure 2.8). The lower peak around 1 mm is related to the small-scale features superimposed on the large scale surface waves.

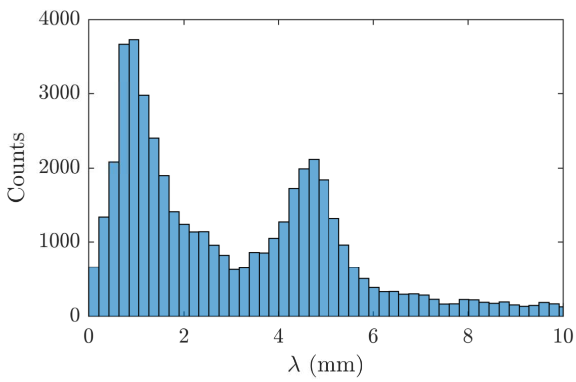

(a) $Re = 0.6 \times 10^6$, $\sigma = 0.25$

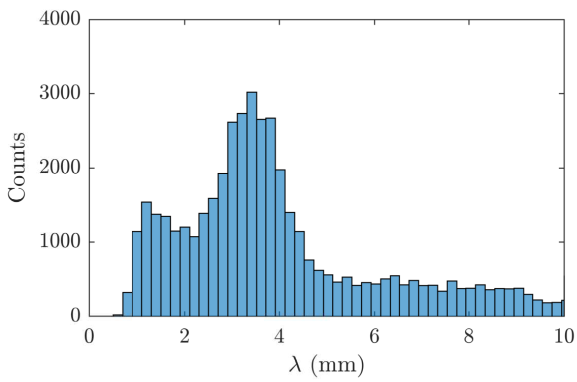

(b) $Re = 1.5 \times 10^6$, $\sigma = 0.25$

Figure 2.10: Typical histograms showing the distribution of wavelengths of cavity surface features for the two cases in Figure 2.8. The peaks at 4.7 mm (a) and 3.4 mm (b) correspond to the wavelengths of the shear-layer structures. The lower peaks at 0.9 mm (a) and 1.2 mm (b) are associated with the small-scale structures.

The same technique was used to measure the wavelength of the surface features from the high-speed photography. As the high-speed photography is of lower spatial resolution than the still images, 3000 images were acquired for each case. The data from the high-speed and still photography show reasonable comparison (Figure 2.11). The wavelength of the KH waves are seen to be mild functions of both Re and σ. The wavelength of the surface waves increase with increasing σ and decreasing Re. The smaller scale features increase in wavelength with increasing Re but appear to be independent of σ.

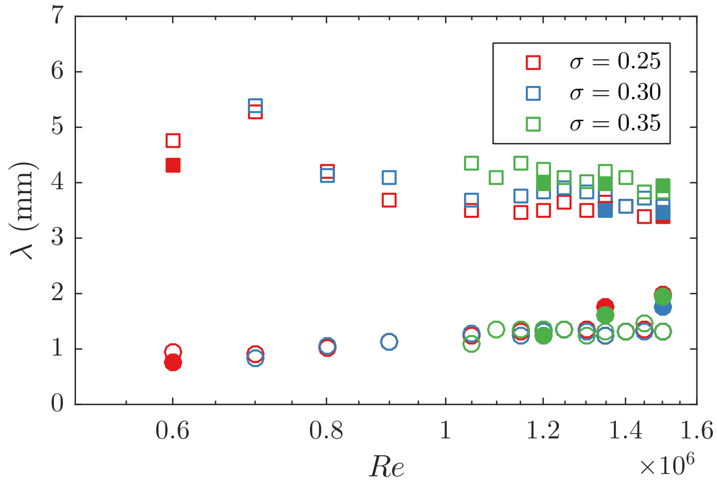

Figure 2.11: Wavelengths of cavity surface features as a function of Re. Different σ are denoted by colour. Solid symbols are data gathered from the high speed photography, while empty symbols are from still photography. Squares are the wavelength of the coherent structures, and circles are the small-scale features.

The dynamics of the cavity surface waves were analysed using the high-speed photography. Time-series of each pixel intensity were processed using a Welch periodogram with Hanning windows. Two sample spectra are shown in Figure 2.12. The peak frequency was extracted for each pixel position in the video, and then averaged across the continuous cavity surface.

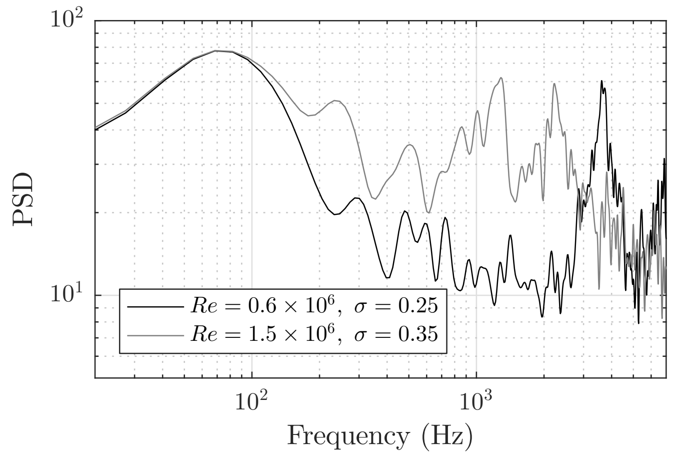

Figure 2.12: Typical spectra of the pixel intensity for two cases: $Re = 1.5 \times 10^6$, $\sigma = 0.25$ and $Re = 0.6 \times 10^6$, $\sigma = 0.35$.

From visual comparison of the high-speed images and the extracted spectra, the peak frequency matching the spanwise waves for each condition was extracted and is shown in

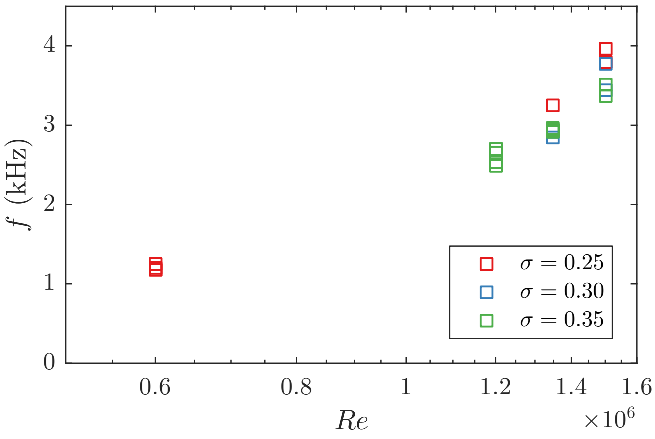

Figure 2.13: Cavity surface wave frequency as it varies with Re. Different σ are denoted by symbol colour.

Figure 2.13 as a function of Re. With only four Reynolds numbers tested the form of the relationship is unknown but clearly increases with Re, and shows a slight increase in frequency with decreasing σ at higher Re values.

Scaling of wake microbubble populations

The microbubble size distributions measured from the shadowgraphy for a range of Re and σ values are presented in Figures 2.14 and 2.15. The dominant bubble size was between 10 and 15 µm for all cases. It is found in later work (Russell et al., 2018), that although the size distributions of bubbles less than 50µm are converged, increased uncertainty is present for larger bubble populations as the number of detections decreases. This can be seen through as increased scatter in Figures 2.14 and 2.15 . Volumetric concentrations corresponding to each of these bubble number density distribution functions are given in Table 2.1. These data reveal that the distribution shape remains similar for all Re and σ values tested. From Figure 2.14 and Table 2.1, it can be seen that the concentration increases with Re, supporting the qualitative description of Figure 2.8 which were taken at a lower σ of 0.25.

The void fraction of the measured bubble populations are shown in Table 2.2. It should be noted that these are only representative of the range of bubble diameters measured. A true void fraction would include all the bubble sizes in the flow. There is an increase in void fraction with decreasing σ but the bubble concentration decreases indicating greater concentrations of larger bubbles. This is supported by the distribution seen in Figure 2.15. This trend of void fraction follows the changing scales of cavity lengths as described qualitatively above, with the breakup region lengthening as the cavitation number is decreased. The increase in void fraction can be attributed to growth in cavity volume and the associated larger scale of the shed structures. No clear trend is apparent with Re.

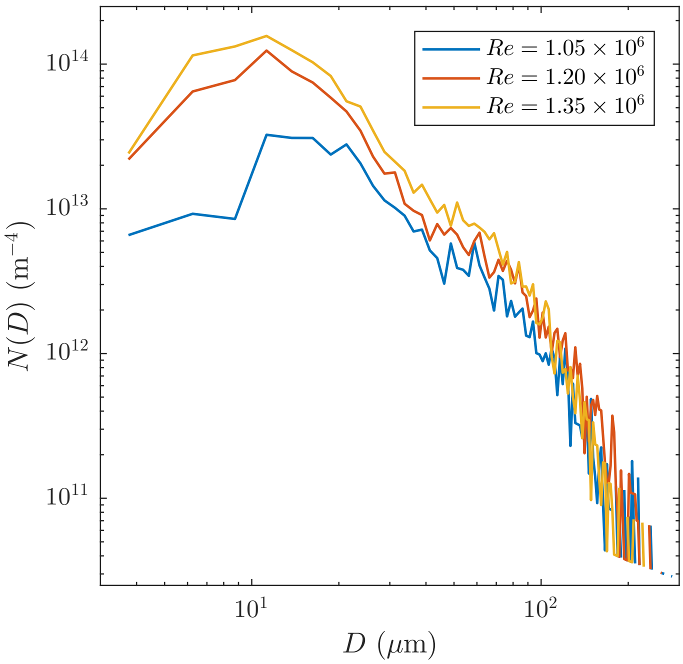

Figure 2.14: Bubble number density distribution function recorded for three different Re at $\sigma = 0.30$. A bin size of 2.5 µm is applied to 1000 images recorded at mid-span, 2.5 chord-lengths downstream of the hydrofoil mid-chord.

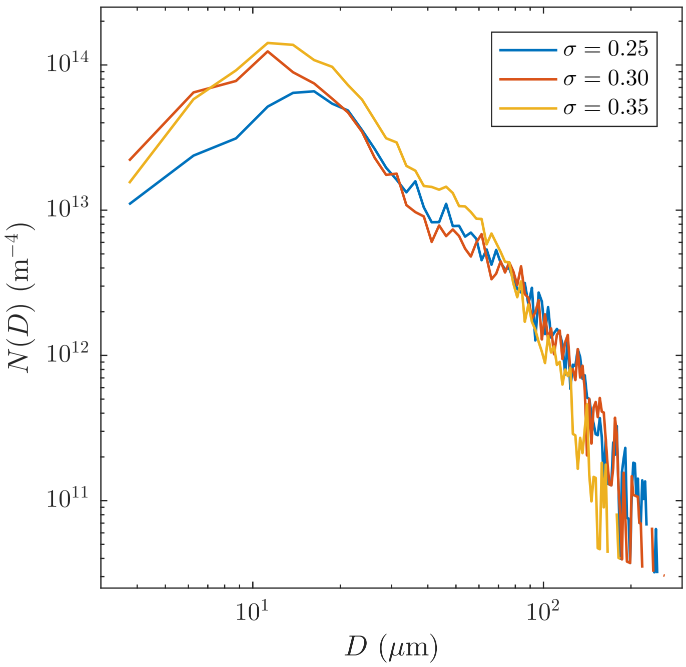

Figure 2.15: Bubble number density distribution function recorded for three different cavitation numbers all at $Re = 1.2 \times 10^6$. A bin size of 2.5 µm is applied to 1000 images recorded at mid-span, 2.5 chord-lengths downstream of the hydrofoil mid-chord.

Table 2.1: Total bubble concentrations per mm^3 for the range of bubble sizes measured. These correspond to each case displayed in Figures 2.14 and 2.15.

$Re \times 10^6$	$\sigma = 0.35$	$\sigma = 0.30$	$\sigma = 0.25$
1.05		0.84	
1.20	2.76	2.03	1.58
1.35		2.83	

Table 2.2: Contributed void fraction for the range of bubble sizes measured. These correspond to each case displayed in Figures 2.14 and 2.15.

$Re \times 10^6$	$\sigma = 0.35$	$\sigma = 0.30$	$\sigma = 0.25$
1.05		0.069%	
1.20	0.073%	0.107%	0.116%
1.35		0.091%	

2.5 Conclusion

The influence of Reynolds and cavitation numbers on the development of sheet cavity geometry and topography, and subsequent breakup and microbubble generation has been studied experimentally both qualitatively and quantitatively. The cavity leading edge is composed of laminar cells resulting from a complex interaction between the separating unstable boundary layer and interfacial effects. The reduction in cell size with increase in Reynolds number tends to converge for values greater than 1.3×10^6. Waves develop in the overlying laminar boundary layer due to the Kelvin-Helmholtz instability that drive coherent breakup of the cavity trailing edge into cavitating vortical filaments. With downstream advection the filaments condense and break up into microbubbles of incondensable gas in the far wake. The scale or wavelength of the instabilities is mildly dependent on the Reynolds and cavitation numbers. The volume of shed vortices and the concentrations of the microbubbles generated increase with Reynolds number. With decreasing cavitation number the microbubble concentration decreases whereas the void fraction increases indicating a greater production of larger diameter bubbles. The dominant bubble size was found to be between 10 and 15 µm for all cases.

Acknowledgements

This project was supported by the Defence Science and Technology Group (Mr. Brendon Anderson and Dr. David Clarke), the University of Tasmania, and the US Office of Naval Research (Dr. Ki-Han Kim, Program Officer) and ONR Global (Dr. Woei-Min Lin) through NICOP S&T Grant no. N62909-15-1-2019.

Chapter 3

Microbubble Disperse Flow about a Lifting Surface

This chapter is presented in article form, and has been published in the proceedings of the *32nd Symposium on Naval Hydrodynamics*.

The citation for the paper is:

Russell, P. S., Venning, J. A., Pearce, B. W., Brandner, P. A., Giosio, D. R., Ceccio, S. L. (2018). Microbubble Disperse Flow about a Lifting Surface. In *32nd Symposium on Naval Hydrodynamics*. Office of Naval Research Science and Technology. Hamburg, Germany.

3.1 Abstract

The effect of freestream nuclei content on stable cavitation about a hydrofoil and subsequent microbubble production in the wake is investigated experimentally. Microbubble concentrations are measured upstream and downstream of the hydrofoil for four upstream nuclei concentrations and three cavitation numbers. For each case the number of activated nuclei on the hydrofoil and the transverse distribution of concentrations in the wake were measured. Upstream nuclei concentrations were measured with interferometric Mie imaging in the size range between 45–250 µm at concentrations up to 30 cm^{-3}. Wake microbubble concentrations were measured using shadowgraphy in the size range 5–50 µm at concentrations up to 600 cm^{-3}. Wake concentration were found to increase for small changes in low upstream nuclei concentrations but to then decrease for further increase in concentrations. Wake concentrations were found to generally increase with decrease in cavitation number for a particular upstream nuclei concentration. The increase in wake

bubble concentrations with seeding increase, at the high cavitation number, is in the smaller bubble size range whereas the increase at the lower cavitation numbers occurs over a greater size range.

3.2 Introduction

Ships are prolific sources of polydisperse bubble populations due to the significant surface disturbances and turbulence they generate. Considerable volumes of air are ingested and dispersed about the hull and by the propulsion and control equipment. Various mechanisms are involved including plunging jets and captured air volumes generated by breaking waves as described by Castro et al. (2014), while surface turbulence may also be sufficient for the hull boundary layer to entrain air (Washuta et al., 2016; Kim et al., 2014; Castro et al., 2016). Lifting surfaces are also of interest here in regards to cavitation occurrence and the consequent contribution to microbubble generation (Yu and Ceccio, 1997; Russell et al., 2016). The dynamics of developed cavitation have been recently examined both experimentally (Ganesh et al., 2016; de Graaf et al., 2017), and numerically (Gnanaskandan and Mahesh, 2016a,b), however, the mechanisms by which cavitating flows generate microbubbles remain largely to be investigated.

As recently examined by Russell et al. (2016) there are limited reported experimental surveys of the bubble distribution within the wake of a cavitating hydrofoil (Maeda, 1991; Yu and Ceccio, 1997; De Graaf et al., 2014). The results of these experiments varied slightly with the dominant bubble size found to be of the order of 10 to 40 µm across this literature. A spatial survey performed by De Graaf et al. (2014) in the wake of a modified NACA 63A015 hydrofoil ($Re = 6.2 \times 10^5$) found the dominant bubble size to vary in the spanwise and streamwise directions between 25 and 40 µm. A later investigation of the same foil (Russell et al., 2016) found that for higher Reynolds number the dominant size was 10-15 µm, a result similar to that of Yu and Ceccio (1997).

The role of free stream nuclei in inception continues to be of significant interest in cavitation research as indicated by the following selection of publications from the last three decades (Meyer et al., 1992; Ran and Katz, 1994; Liu and Brennen, 1998; Gindroz and Billet, 1998; Hsiao and Chahine, 2005; Van Rijsbergen and Van Terwisga, 2011; Nagaya et al., 2011; Brandner et al., 2015; Mørch, 2015; Zhang et al., 2016; Park and Seong, 2017). As a part of this extensive activity there has been publication also on nuclei measurement techniques, both optical (Lebrun et al., 2011; Ebert et al., 2016) and mechanical (Khoo et al., 2016), with a number of studies making comparisons between the various techniques (Billet and Gates, 1981; Katz et al., 1984; Mées et al., 2010). As reflected on by Billet (1986), the volume of literature on the topic indicates the complexity of the problem, largely due to its multi-phase and inherently statistical nature. From this it is clear that each of these measurement techniques have their particular advantages and limitations so that none are indispensable when attempting to extensively examine problems involving the presence of nuclei/microbubbles with both diameters and concentrations ranging over several orders of magnitude. To this end the development of an optical interferometric measurement technique for use in the Cavitation Research Laboratory (CRL) water tunnel at the Australian Maritime College has been established to accompany existing optical (Russell et al., 2016) and mechanical (Khoo et al., 2016) bubble measurement capabilities.

Microbubbles respond dynamically to the changing pressure field about a hydrofoil with the effect of uneven diffusion during advection which is still to be fully understood. Not only is the size of the bubble important but the velocity of the bubble relative to that of the surrounding fluid. Given a sufficient velocity difference smaller bubbles can grow from their initial radius by an order of magnitude (Smith and Peterson, 1984). In the context of established cavitation, studies on travelling nuclei bubble cavitation have utilized standard headforms to investigate the dynamics of activated individual bubbles/nuclei (Ceccio and Brennen, 1991; De Chizelle et al., 1995). The maximum radius of activated nuclei is expected to increase as cavitation number decreases. More recently observations have been reported on the significant effect of free stream nuclei content on developed cavitation about a sphere (De Graaf et al., 2016) and a hydrofoil (Venning et al., 2017).

The present study follows on and extends the earlier work of Russell et al. (2016) on the measurement of microbubble populations in the wake of a cavitating hydrofoil. A NACA 63A015 profile hydrofoil of similar dimensions to the earlier study has been used. However, a rectangular rather than elliptical profile was selected to achieve a more consistent cavity length over the span of the hydrofoil and achieve a greater spanwise region of nominally uniform bubbly wake. In addition, profiles of microbubble populations were measured across the wake for both the unseeded (background nuclei population only (Venning et al., 2018)), and a range of three injected nuclei populations. Upstream nuclei populations have been measured using an Interferometric Mie Imaging technique (IMI), individual bubble activations over the hydrofoil surface are obtained from high-resolution still imaging and wake populations characterised via long range microscopy shadowgraphy. From these measurements, observations can be made regarding the effect of upstream nuclei content on the developed cavity dynamics and the resulting microbubble content and distribution in the downstream wake.

3.3 Experimental Approach

Experiments were carried out in the Cavitation Research Laboratory (CRL) variable pressure water tunnel at the University of Tasmania. The tunnel test section is 0.6 m square by 2.6 m long in which the operating velocity and pressure ranges are 2 to 12 m/s and 4 to 400 kPa absolute, respectively. The tunnel volume is 365 m^3, which is filled with demineralised water. Demineralised water is used to ensure dissolved contaminants do not precipitate over time, forming particles that may trap gas and become cavitation nuclei, or otherwise adversely affect the flow and discolour the water. The tunnel has ancillary systems for rapid degassing and for continuous injection and removal of nuclei and large volumes of incondensable gas. The test section velocity is measured from one of two (low and high range) Siemens Sitrans P differential pressure transducers models 7MF4433-1DA02-2AB1-Z and 7MF4433-1FA02-2AB1-Z (measuring the calibrated contraction differential pressure) with estimated precision of 0.007 m/s and 0.018 m/s, respectively. The velocity and pressure in the test section are controlled to maintain a constant Reynolds number (Re) and cavitation number (σ). The test section velocity is spatially uniform to within 0.5%, has temporal variations of less than 0.2%, and the free stream turbulence intensity is about 0.5%. Detailed descriptions of the facility are given in Brandner et al. (2006, 2007) and Doolan et al. (2013).

A stainless steel hydrofoil was mounted to the ceiling of the test section, as shown in figure 3.2, located 1.15 m downstream of the entrance to the test section. The hydrofoil profile was a modified NACA 63A015, rectangular planform hydrofoil, with a chord length of 150 mm (c) and a 300 mm span. The profile modification involved an increase of the trailing edge thickness (see figure 3.1) to enable practical manufacture of the scaled model and to reduce susceptibility to in–service trailing edge damage. The modified profile was achieved by the addition of $0.00385x$ to the standard profile, where x is the chord-wise distance from the leading edge.

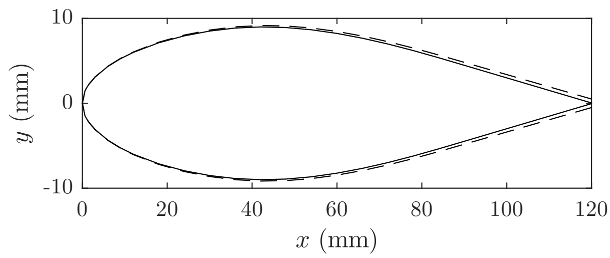

Figure 3.1: Comparison of a standard (solid) and modified (dashed) NACA 63A015 section. The modification thickens the profile gradually from the leading edge through to a maximum at the trailing edge. Note the aspect is stretched vertically to highlight the difference in profile.

Nuclei were injected from an array of microbubbles generators located in the plenum upstream of the tunnel honeycomb (figure 3.2). The array consists of 3 rows of 10 generators distributed on a 80 mm triangular grid which creates a homogeneously seeded

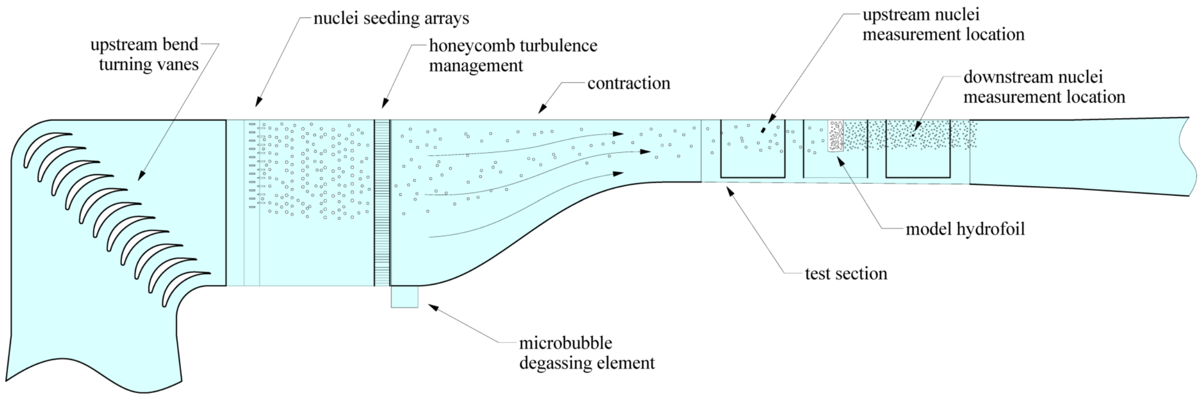

Figure 3.2: Schematic of microbubble injection and measurement locations within the CRL water tunnel circuit. The optical arrangement used in the water tunnel to detect seeding nuclei through IMI and glare point imaging. The camera on the left captured the interferometric images through a glass port mounted to the wall of the tunnel to ensure optical aberrations are minimised. The camera on the right simultaneously captures in focus glare points for nuclei concentration measurement and the location of the bubbles to be processing with IMI.

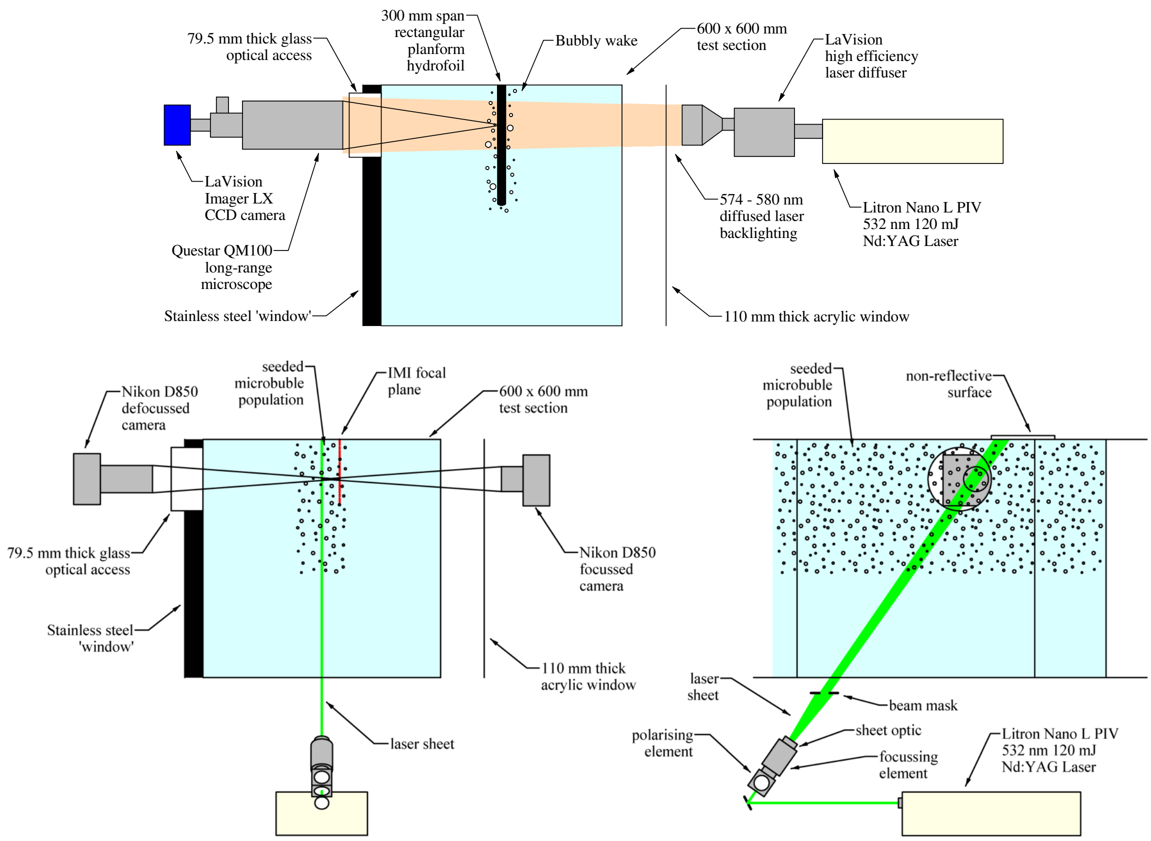

Figure 3.3: (top) Schematic of experimental set-up for shadowgraphy measurement in the wake of a hydrofoil in the CRL water tunnel test section. (bottom) Schematic of experimental set-up for interferometric nuclei measurement upstream of the foil.

nominally rectangular image in the test section enveloping the hydrofoil model (over 300 mm deep by 100 mm wide). The generators used for these experiments are of the so-called minitube type involving the rapid depressurisation of supersaturated water in a confined micro-nozzle the operation of which has been reported on previously (Brandner et al., 2010b; Trump et al., 2015; Giosio et al., 2016).

Data was collected using a variety of qualitative and quantitative imaging techniques. Long range microscopy shadowgraphy is a well-established technique for the sizing of particles many times larger than the imaging light wavelength. The technique then can be implemented at many scales but the dynamic range will dependent on the optical setup (Settles, 2012). Increased magnification will lead to a smaller minimum detectable particle size but will reduce the field of view and depth of field of the system. Therefore increased magnification will reduce the detection volume, the maximum bubble size and increase the number of images for converged statistics. These properties make shadowgraphy well suited for measuring the high bubble concentrations found in the wake of the hydrofoil, typically above $O(10^9)$ m^{-3}, but poorly suited for measuring seeding concentration, approx $O(10^4)$ m^{-3} in these experiments.

IMI allows for the sizing of bubbles on the order of microns in size over a much larger field of view than shadowgraphy can accomplish with accurate sizing. However the interference patterns occupy a much larger portion of the sensor than detections in a shadowgraphy image necessitating low volumetric concentrations. The maximum concentrations measurable depends on the illumination used and several other optical parameters particular to the setup (Dehaeck and van Beeck, 2007; Mées et al., 2010; Damaschke et al., 2002) but here can typically measure below $\mathcal{O}(10^7)$ m^{-3} with measurable sizes ranging from $50-300$ µm. This is ideal however for measuring the upstream seeding populations which are both small in size and low in concentration.

Still photography allows us to qualitatively examine the effects seed nuclei have on the cavitation topology but the magnification is such that both seed bubbles and those measured through shadowgraphy are too small to be seen. It appears from these images that the void fraction in the wake increases with increased seeding but what will be investigated here are bubble populations too small in size to be observed in these images.

High-resolution (36.3 megapixel) still photographs of the cavity were captured using a Nikon D810 DSLR with a Nikon AF-S Nikkor 85mm 1:1.4G lens. Illumination was provided by two simultaneously triggered stroboscopes, a Drello 3018 scope with 4037 flashlamp and a Drello 1018 scope with 4040 flashlamp. Injected nuclei content was measured upstream of the foil using simultaneously acquired in-focus still photography and out-of-focus Interferometric Mie Imaging (IMI), illuminated by a pulsed sheet of Nd-YAG 532 nm laser light oriented along the centreline of the tunnel after passing through a 420–680 nm Thorlabs beam splitting polariser (see figure 3.3). In focus images were captured by a Nikon D850 DSLR with a Nikkor 105mm lens and were used to collect concentration count statistics and spatially locate the nuclei for later processing of the out-of-focus images. IMI were captured using a Nikon D850 DSLR camera, with a Sigma APO Macro 180 mm F2.8 EX-DG-OS-HSM with the focal plane of the camera positioned 45 mm past the centerline of the tunnel.

Shadowgraphy measurements were taken 5 chord lengths downstream of the hydrofoil mid-chord, at 1/3 span from the ceiling of the tunnel (or hydrofoil root) for 7 transverse positions when normalised by wake width ($y/w = 0.05,\ 0.25,\ 0.40,\ 0.50,\ 0.60,\ 0.75,\ 0.95$). Shadowgraph images were acquired using a LaVision Imager LX 12-bit 29M camera in combination with a Questar QM100 long-range microscope. The camera CCD sensor size is 6600 $\times$ 4400 pixels. The long-range microscope was coupled to the camera using a 3$\times$Barlow lens giving a field of view of 1917 µm $\times$ 1279 µm with a spatial resolution of 0.29 µ/px. This optical set-up allows a range of bubble sizes from 5 to 300 µm to be measured with a 5 µm bubble being imaged with 17 pixels across the diameter. To improve the optical access the 110 mm acrylic test section side window was replaced by a stainless steel window fitted with a 160 mm diameter 79.5 mm thick glass port. Backlit illumination was provided by a Litron 532 nm 120 mJ 20 Hz Nano L PIV Nd:YAG laser guided through a LaVision high efficiency diffuser using a fluorescent dye plate. A cone of diffused light is produced with emitted pulses in the wavelength range 574 to 580 nm and of 20 ns duration when excited by 5 ns 532 nm laser pulses. Both the camera and diffuser were mounted on a 3-axis Isel (790 mm) linear traverses to allow accurate positioning. The laser and camera were triggered from a programmable timing unit and the acquisition was carried out using LaVision DaVis Version 8.4.0

Data were obtained at a fixed incidence of $\alpha = 3.5°$ for four nuclei seeding concentrations (no seeding, low, high and very high) and three cavitation numbers ($\sigma = 0.35,\ 0.30,\ 0.25$) defined by $\sigma = (p - p_v)/0.5\rho\, U^2$ where p is the freestream static pressure at 1/3 span of the hydrofoil from the ceiling, p_v the vapour pressure, and ρ the density of the fluid. The chord based Reynolds number remained fixed at $Re = Uc/\nu = 1.5 \times 10^6$, where U is the free stream velocity, c the chord length and ν the kinematic viscosity. The dissolved oxygen content was maintained between $DO_2 = 25$–30% of the saturated concentration at atmospheric pressure for all test conditions. Images showing the range of the conditions tested is presented in figure 3.4.

All data were processed and analysed in MATLAB 2017a using custom sizing scripts. Shadowgraphy measurements in the wake used localised thresholding to isolate potential bubbles and non-linear multivariate regression to precisely size bubbles with corrections for out of focus blurring. For upstream nuclei measurements the location of nuclei were determined by global thresholding of the in-focus image. A transformation was then applied to these locations to identify the precise centre of the bubbles in the out of focus image. A square region containing each out-of-focus pattern was then extracted and analysed using wavelet analysis to measure fringe frequency of the interference lines.

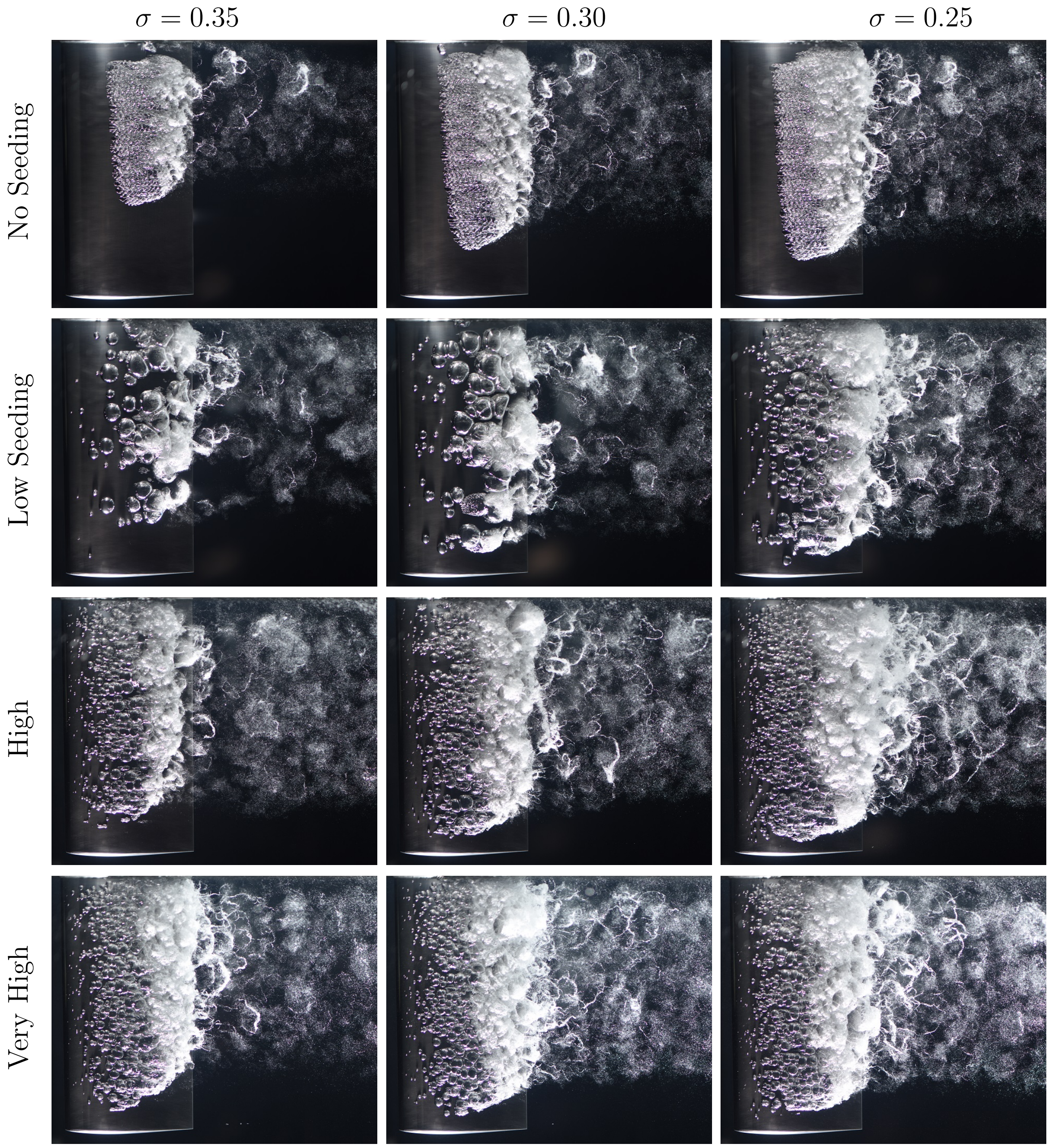

Figure 3.4: Photographs of the conditions tested. The number of large bubbles in the near wake increased with the concentration of seeding and decreased with cavitation number. Topology of cavity collapse changes with the seed concentration.

3.4 Results

3.4.1 Seeding Measurements

The concentration of injected nuclei was measured by threshold detection from the in-focus glare point images and is summarised in table 3.1. All tunnel parameters were maintained constant except for the pressure in order to vary the cavitation number. The combined change in pressure and small changes to the operating parameters of the nuclei injectors created changes in the test section nuclei concentration. Lower pressures and thus cavitation numbers were accompanied by an increase in the concentration of nuclei passing the hydrofoil. The aim during testing was to produce four uniformly distributed seeding concentrations. Upon data processing it was clear that the two highest levels of seeding were greatly affected by changes in tunnel pressure and that the middle seeding concentration was higher than anticipated. Interferometric images were able to provide more detail and produced size distributions of the nuclei, see figure 3.5. It was determined that the minimum size faithfully measured by the system was a microbubble that produced three fringes across its interference pattern. Upon calibration this corresponded to a size of 45 µm. Background nuclei concentrations in the tunnel have been measured using a cavitation susceptibility meter which show the largest nuclei to be or order 10 µm with concentrations of less than 10^{-6} cm^{-3} (Venning et al., 2018). These results imply that the background nuclei concentration from the present IMI measurements are of contaminants only. This is confirmed by inspection of the raw IMI images where detections were found to not show fringe patterns consistent with bubble scattering (Ebert et al., 2016). These are of such small concentrations that they may be ignored and have not been corrected for in the seeded measurements. Activation of background nuclei from non-seeded test cases were also not heard during testing or observed in any of the images.

Table 3.1: Measured seeding concentration per cubic centimetre presented by nominal seeding level and tunnel test section σ values.

(N/cm^3)	$\sigma = 0.35$	$\sigma = 0.30$	$\sigma = 0.25$
No Seeding	0.86	0.71	1
Low	1.77	1.89	2.85
High	14.44	20.9	23.89
Very High	20.1	26.31	31.68

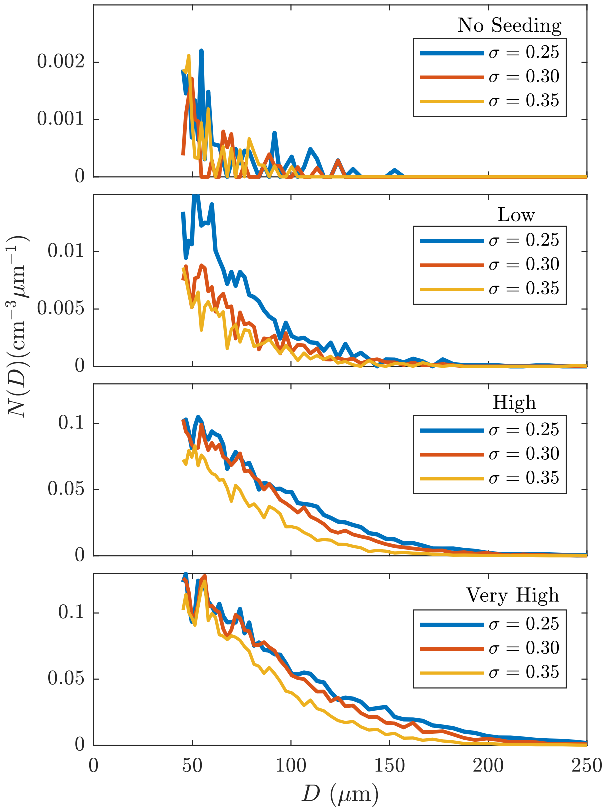

Figure 3.5: Injected microbubble nuclei distribution measured using IMI upstream of the hydrofoil.

3.4.2 Cavity geometry and topography

A set of high-resolution still photographs (figure 3.4) provide an overview of the conditions tested. Cavitation about the hydrofoil was tested at a chord based $Re = 1.5 \times 10^6$, and angle of incidence $\alpha = 3.5°$, for a range of seeding concentrations and tunnel σ values. Unseeded inception took place just above $\sigma = 0.35$ occurring sooner with the nuclei injection.

Bubbles activated by the foil may undergo fission upon collapse resulting in a cloud of small vapor/gas bubbles when seeding concentrations are sufficiently low (Brennen, 2002). However, bubble-bubble, and bubble-body interactions along with coalescence may modify the cavity closure at higher seeding concentrations (Chahine and Duraiswami, 1992; Takahira, 1997; Hsiao et al., 2016). The cavity length (streamwise extent) and width (spanwise extent) increased with decreasing σ and increased with seeding level. Primary cavity separation and collapse did not extend beyond the trailing edge of the hydrofoil in all the conditions reported but continued bubble break-up and condensation was observed in the near wake structures. The effect of seeding on the cavity topography may be seen in more detail in figure 3.6 for fixed $\sigma = 0.35$. Without seeding the leading edge of the cavity has a smooth cellular structure downstream of which interfacial instabilities develop which fed into and affect downstream cavity condensation and breakup (Russell et al., 2016). Seeded nuclei activated by the hydrofoil immediately broke up the leading edge of

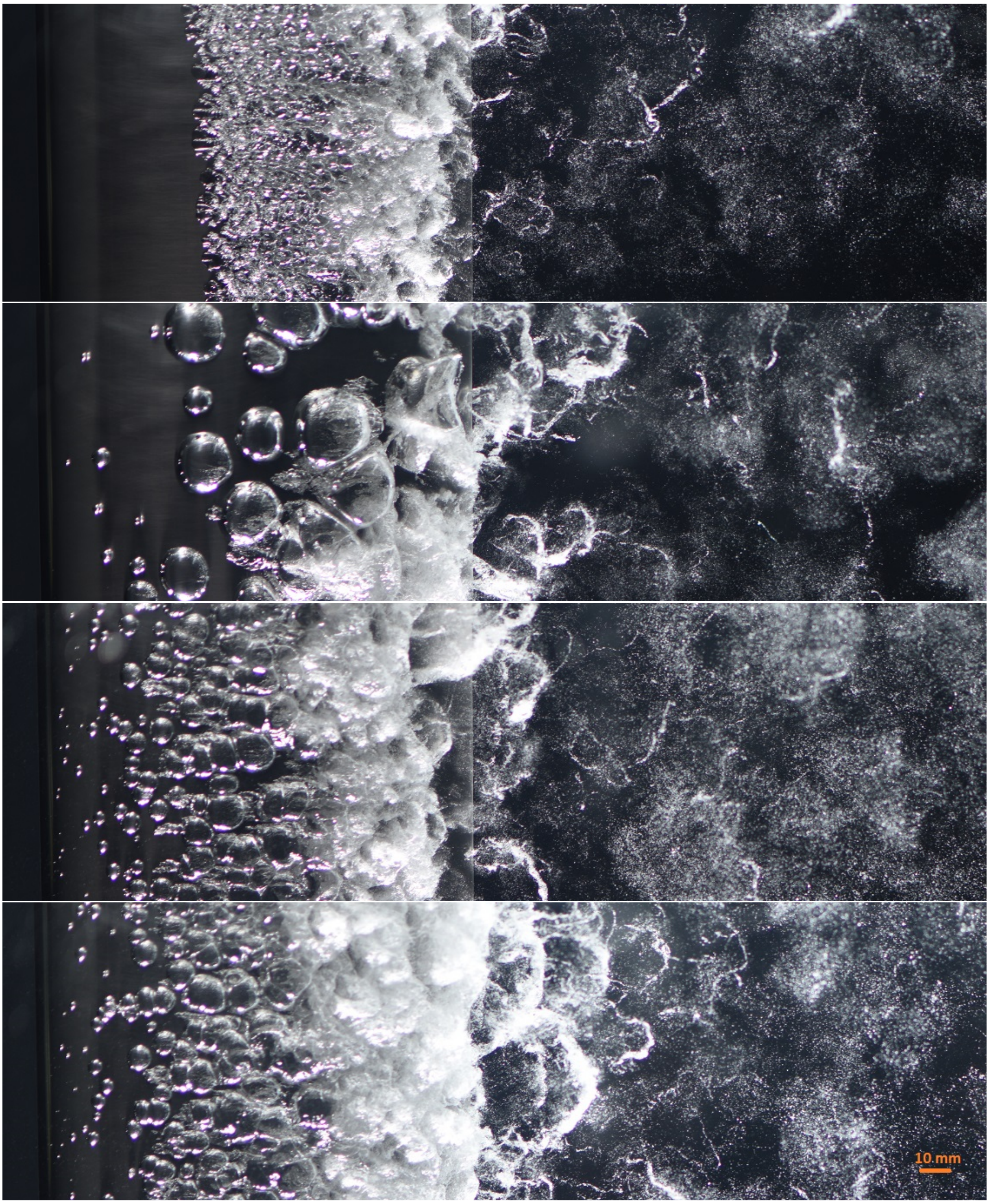

Figure 3.6: Image samples taken at $\sigma = 0.35$ for the full range of seeding conditions. In all seeded flow cases the stable attached cavity is suppressed. The cavity closure physics changes with seeding concentration. At low seeding level, individual bubble collapse can be observed. At higher seeding, bubbles coalesce into a collapse regime similar to that of an attached cavity but with a higher density of bubbles observed in the wake. Qualitatively, the observed bubble concentration in the wake increases with seeding level.

the cavity. For low seeding, bubbles activated by the hydrofoil retained their shape longer and grew to larger sizes than at the higher seeding concentrations where greater activation rates led to bubble coalescence and interaction restricting growth. The instability along the cavity surface was no longer able to develop as discrete bubble cavities persisted deep into the breakup region, modifying the collapse physics. The condensation region near the trailing edge was initially reduced with the addition of low levels of seeding but grew larger to exceed the no seeding case as seeding concentrations increased.

3.4.3 Activated nuclei about the hydrofoil

To explore the effect of seeding further the area-concentration of nuclei activated on the hydrofoil between 20–50% chord and 20–80% span at each test condition was measured across 15 images. Figure 3.7 highlights the region of interest on a sample image.

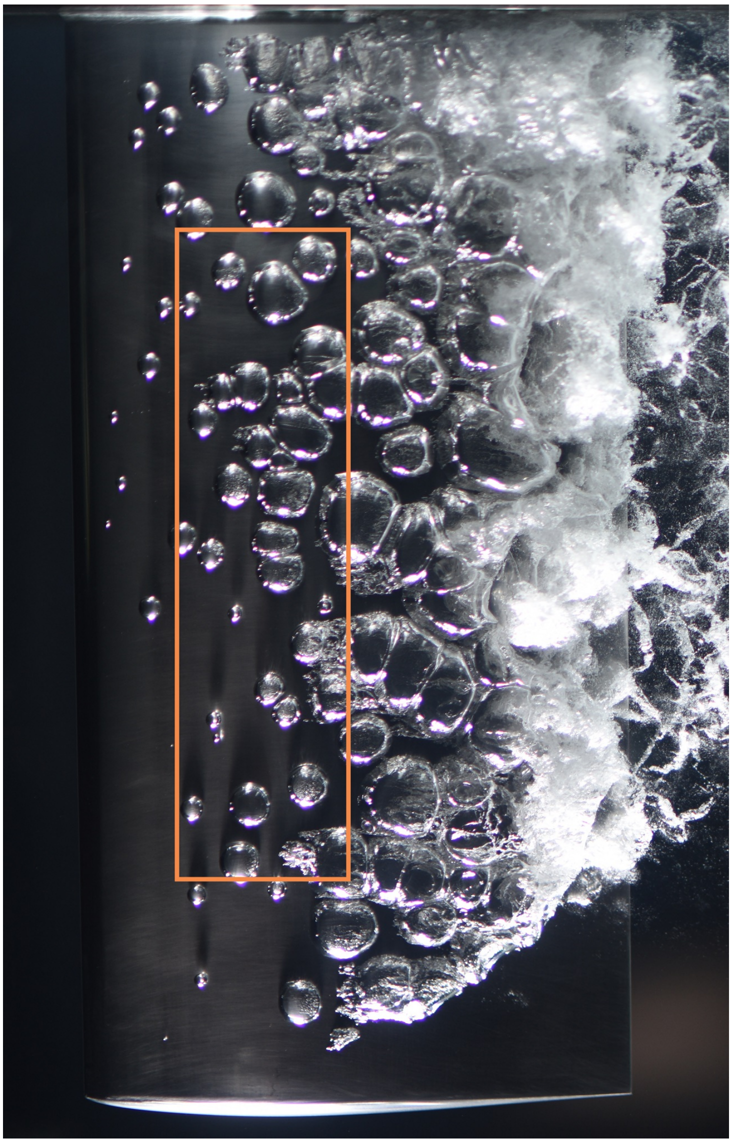

Figure 3.7: A sample image at tunnel $\sigma = 0.30$ with low nuclei seeding is shown with an overlay highlighting the region of interest (20–50% chord and 20–80% span) in which activated nuclei were counted.

These results are shown in table 3.2 and plotted in figure 3.8. The number of activated nuclei shows a sudden increase at low concentrations followed by an apparently linear increase from the low to higher seeded concentrations. For the range of bubble sizes resolved from the IMI (about 50 to 250 μm) there is little static delay suggesting there should be little dependence on nuclei size and cavitation number and that most will be activated with critical pressures about the hydrofoil. The linear trend between upstream concentration and number of activations and the overlap between conditions tends to confirm this observation.

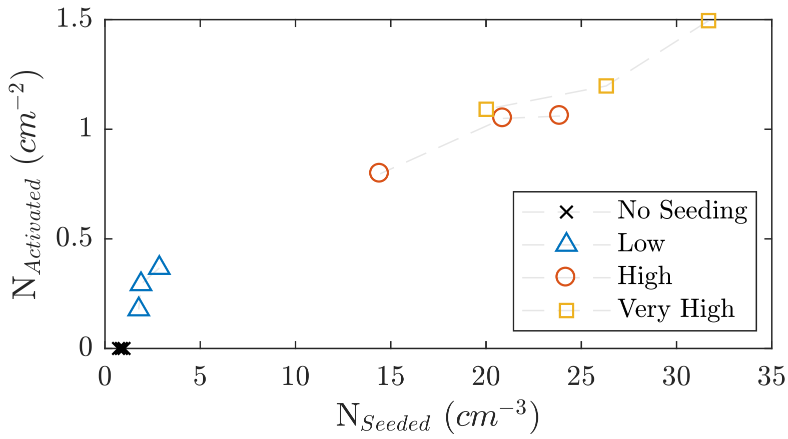

Figure 3.8: Area concentration of nuclei activations on the hydrofoil for each volumetric concentration injected nuclei.

Table 3.2: Number of bubbles activated between 20–80% span and 20-50% chord of the hydrofoil. (N/cm^2)

μ	$\sigma = 0.35$	$\sigma = 0.30$	$\sigma = 0.25$
No Seeding	**0.00**	**0.00**	**0.00**
Low	**0.18**	**0.29**	**0.37**
High	**0.80**	**1.05**	**1.06**
Very High	**1.09**	**1.20**	**1.50**
Std. Dev	$\sigma = 0.35$	$\sigma = 0.30$	$\sigma = 0.25$
No Seeding	0.00	0.00	0.00
Low	0.04	0.06	0.07
High	0.10	0.09	0.09
Very High	0.12	0.17	0.19

3.4.4 Shadowgraphy Measurements

The measured spanwise distribution of wake microbubble concentration for each test condition is presented in figure 3.9. The wake widths varied from about 80 mm wide for the unseeded case to about 100 mm wide for the highest seeding concentration. The pressure and suction sides of the hydrofoil correspond with dimensionless transverse ordinates $y/w = 0$ and 1 respectively. These results show concentrations within the 0-50 µm size range. Although the measurement system was able to capture bubbles faithfully up to a size of 300 µm inspection of the data revealed that for bubbles larger than 50 µm there were insufficient detections for converged statistics. The shape of these plots indicates a

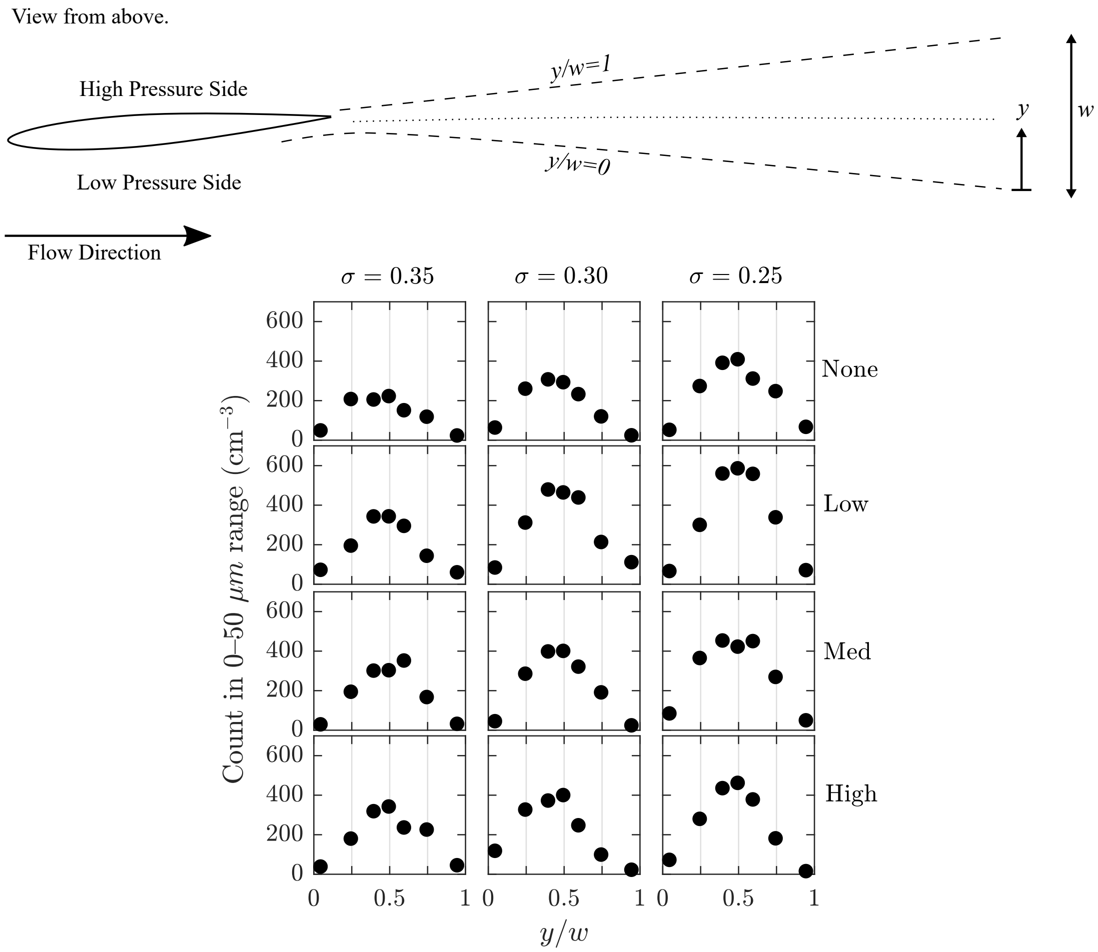

Figure 3.9: Wake concentrations for bubbles in the 5-50 µm size range are plotted against transverse wake location for each seeding concentration and tunnel cavitation number. A location of 0 corresponds to the edge of the wake on the pressure side of the hydrofoil.

slight asymmetry in the concentration distribution with lower concentrations on the suction side of the wake. Although the peak concentration is generally at about mid wake. The data show a general trend of increasing peak concentration with cavitation number reduction similar to the qualitative trend apparent in the still photography shown in figure 3.4. The peak concentrations show an increase in the lowest seeding concentration compared with the unseeded case but a slight decrease with further increase in seeding concentration. This effect is most pronounced at low cavitation numbers. These results appear contrary to qualitative observations noted above suggesting that the greater concentrations apparent in figure 3.4 may be attributable to bubble sizes greater than those measured with the shadowgraphy. This further suggests that two or more magnifications, along with larger data samples, are required to fully resolve the wake microbubble populations. The discrepancy is reconciled by the observation that the intensity of light reflected by bubbles is proportional to their area. This biases the perceived number of bubbles in macro images towards those with larger bubbles. Further, the resolution of the overview image are ≈ 76 µm per pixel and so the microbubbles detected through shadowgraphy are smaller than a single pixel in these macro images. Tests capturing a wider size range at reduced number of transverse locations is planned to examine this further.

Mean void fraction values from $y/w = 0.4, 0.5, 0.6$, for the measured size range are shown in table 3.3. These reflect the general trends in concentration discussed above. Similarly the mean concentrations as a function of the area concentration of activations are shown in figure 3.10 which also reflect the trends discussed above. Overall the results suggest that greater concentrations and increased gas diffusion occurs with lower concentrations where activated bubbles grow to larger sizes than for higher concentrations.

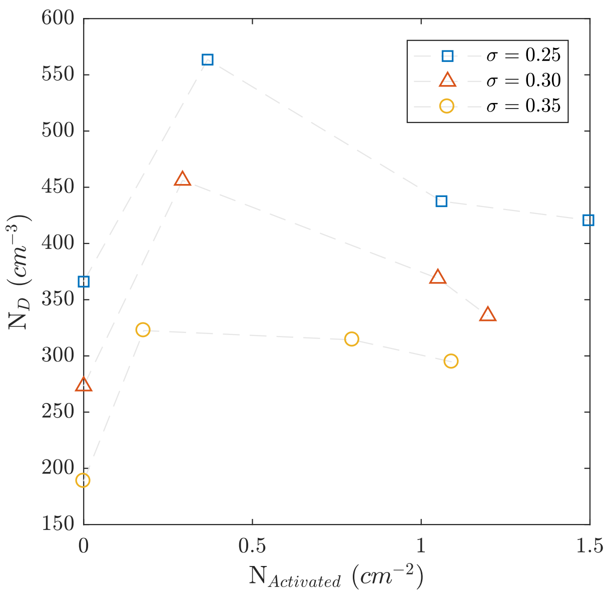

Figure 3.10: Bubble count per cubic centimetre within the 0-50 µm size range are plotted against the number of nuclei activations per square cm for each seeding concentration and tunnel cavitation number.

Mid-wake microbubble population distributions are presented for each test condition, in figure 3.11. Similar trends are present as with the previous data although differences in the range of bubble sizes affecting these trends can be discerned. Uncertainty in the population distributions in figure 3.11 increases in magnitude for smaller bubble sizes where less detections were recorded, but for a 10 µm bubble is estimated as

Table 3.3: Mean void fraction contribution from $y/w = 0.4, 0.5, 0.6$ across the wake for different seeding and σ conditions for bubbles 5–50 µm in diameter.

Void Fraction $\times 10^{-6}$	$\sigma = 0.35$	$\sigma = 0.30$	$\sigma = 0.25$
No Seeding	9.5	10.7	15.5
Low	13.5	17.3	21.5
High	12.8	14.9	17.8
Very High	13.1	16.9	18.2

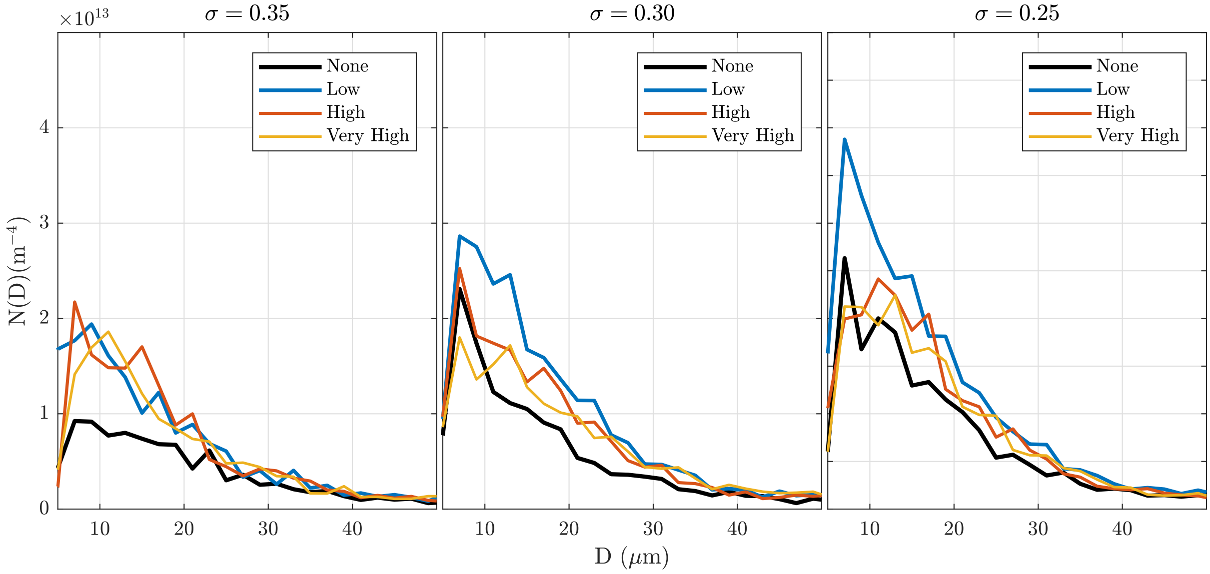

Figure 3.11: Wake bubble population distributions are plotted for constant tunnel cavitation number at four different seeding levels. An increase in σ resulted in less bubbles. The effect of added nuclei changed with σ, particularly for $\sigma = 0.35$.

$N(10\ \mu m) = \pm\ 0.4 \times\ 10^{13}\ m^{-4}$. Consequently, smaller fluctuations and finer differences in the population distributions should are overlooked, while the larger differences observed in figure 3.11 remain valid. In addition, since identical optical parameters were used to measure bubbles across all flow conditions, uncertainty stems from the limited number of detections that occur within a narrow band of bubble sizes. In this regard, while a single bubble size may contain greater uncertainty, trends persisting across the distribution carry much greater confidence. For $\sigma = 0.35$, whilst there is a change in wake concentration with the addition of seeding, there is little change with further increase of the upstream concentration. At this cavitation number the increase in overall wake concentration was attributable to bubble sizes in the range below about 22 µm. For the lower cavitation numbers it is ventured that the increase in concentration occurs over a greater range of bubble sizes. For the low seeding concentration which gave the greatest increase in the wake concentration there is generally a greater increase in the smaller bubble sizes. As discussed, further data at lower magnifications are required to improve the dynamic range and fully resolve the total wake populations.

To summarise, the upper and lower bounds of both freestream seeding levels (no seeding and high seeding) and measured wake concentrations are presented in figure 3.12. The background measurements for the unseeded case were measured using a cavitation susceptibility meter (Venning et al., 2018), as noted earlier. That is, the dashed blue line is the wake concentration for the unseeded case corresponding to the background concentration shown by the solid blue line. Whereas, the dashed brown line shows the largest measured wake concentration which corresponds to the low seeding level for the lowest $\sigma = 0.25$. The solid black line is for the very high seeding concentration at the lowest $\sigma = 0.25$ which gives a wake concentration between the two dashed lines. These data suggest that the bubble production in the wake is initially highly sensitive to low concentrations but becomes only mildly sensitive to order of magnitude changes in upstream nuclei concentrations at least within the measurement ranges of the current experiment.

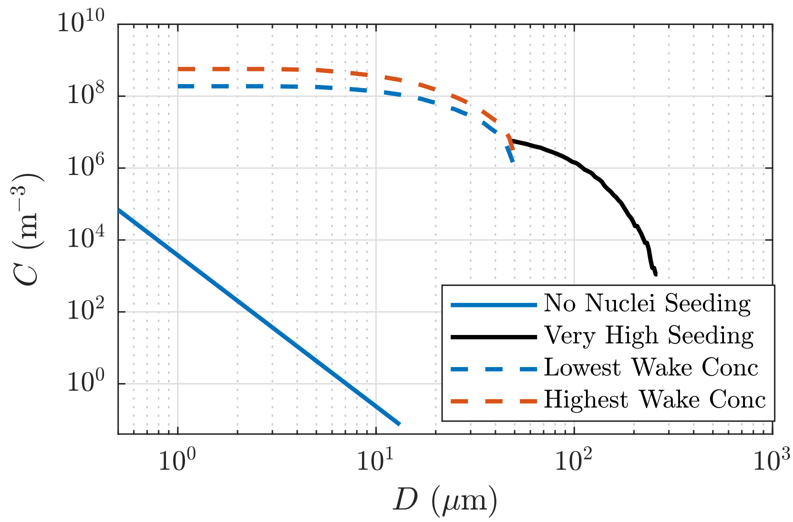

Figure 3.12: Cumulative populations of the upstream flow (solid lines) and in the wake (dashed, measured with shadowgraphy). The background data for the unseeded case were measured with a cavitation susceptibility meter as reported in Venning et al. (2018).

3.5 Conclusion

The influence of seeding concentration and cavitation number on the development of cavity geometry and topography, and subsequent microbubble generation has been studied experimentally both qualitatively and quantitatively. The cavity leading edge is broken up by the introduction of freestream nuclei with the condensation and breakup region changing with increased nuclei concentration. Nuclei seeding concentrations were measured and related to the number of activations about the hydrofoil with a portion of the size distributions measured using IMI. High resolution still photography shows that bubble populations increase with nuclei concentrations, however shadowgraphy reveals that microbubble concentration in the range of 5-50 µm increases for low seeding levels but decrease with further increase in seeding concentration. Wake bubble concentrations overall increase with decrease in cavitation number. The increase in wake bubble concentrations with seeding increase, at the high cavitation number, is in the smaller bubble size range whereas the increase at the lower cavitation numbers occurs over a greater size range. Wake microbubble concentrations are highly sensitive to small changes in low active freestream nuclei concentrations but become only mildly sensitive to order of magnitude changes for higher upstream concentrations. Further, more extensive measurements using multiple optical setups and with greater sample sizes are required to capture bubbles over a larger range of sizes in the wake to explore these flows further. Experimental measurements capturing the full spectrum of bubble sizes – while challenging – would enable calculation of the total void fraction and aid in the validation or contrast of results with computational studies. They may also identify the mechanisms that lead to a reduced quantity of wake microbubbles 5-50 µm in diameter with increased seeding.

Chapter 4

Calibration of Mie Scattering Imaging

This chapter is in article form. (Russell et al., 2020b) The citation for the publication is, Russell, P. S., Venning, J. A., Pearce, B. W., & Brandner, P. A. (2020). Calibration of Mie scattering imaging for microbubble measurement in hydrodynamic test facilities. *Experiments in Fluids* 61(93) . https://doi.org/10.1007/s00348-020-2927-7.

The contributing authors are:
Russell, P. S., Venning, J. A., Pearce, B. W., and Brandner, P. A.

4.1 Abstract

Calibration of the Mie Scattering Imaging (MSI) technique for microbubble size and concentration measurement in hydrodynamic test facilities is investigated. Monodisperse bubbles are generated by a microfluidic 'T' junction, and individual bubbles simultaneously imaged with shadowgraphy and MSI. Nominal bubble diameters between 30 and 150 µm were tested. The influence of fringe uniformity and intensity for each polarisation on measurement precision was investigated. Parallel polarisation was chosen over perpendicular for its more uniform spacing despite the lower intensity. The linear relation between fringe wavelength and bubble diameter was demonstrated at a measurement angle of 90°. The calibration was derived from constants for light scattering, and for the imaging optics. The wavelength of the scattered fringe pattern is predicted using the Lorentz-Mie theory. A practical method for the calibration of interference patterns is presented. Using this approach the measured bubble diameters from the shadowgraphy and MSI compare to within 1 µm. A method for determining the size dependent measurement volume for axisymmetric and arbitrary beam profiles is also presented.

4.2 Introduction

On the macroscopic scale almost all volumes of water of practical interest contain bubbles. However, the range of sizes and concentrations present varies greatly. For breaking ocean waves the spectrum of bubble radii extends at least four decades, with bubble concentrations found across six decades (Deane and Stokes, 2002). Most bubble measurement techniques lack the dynamic range to measure across one of these parameters, let alone both, therefore hydrodynamic test facilities require multiple techniques in order to cover the full gamut of possibilities (Brandner, 2018). Mechanical techniques often cover a larger dynamic range but are inherently intrusive to implement (Venning et al., 2018). Optical techniques are non-intrusive but are usually restricted to approximately two decades in either the concentration, size, or both (Xu, 2001; Randolph et al., 2014). In addition, these techniques have a lower limit which is of the order of the wavelength of light used. Exceptions to this, most notably holography, typically require a high level of rigour to accomplish (Katz and Sheng, 2010). Mie Scattering Imaging (MSI) is an important technique as it covers a difficult region of the size-concentration map, being able to measure bubbles on the order of micrometres in size at very low concentrations. While acoustic techniques also cover this region — possessing wide dynamic range and are un-intrusive (Chahine and Kalumuck, 2003; Duraiswami et al., 1998) — they measure integral concentrations between a transmitter and receiver, and are therefore difficult to implement for use with targeted bubble seeding or spatially variant bubble populations.

The MSI technique has been given many names including: Interferometric Laser Imaging (Glover et al., 1995), Mie Scattering Imaging (Dunker et al., 2016), Global Phase Doppler (Damaschke et al., 2002; Albrecht et al., 2013), Inteferometric Laser Imaging for Droplet Sizing (Pu, 2005), and Interferometric Particle Imaging (Ebert et al., 2014). The principle by which these methods operate is the same, monochromatic light illuminates a transparent bubble (or particle) and the light scattered from it produces an interference pattern. The frequency of this interference pattern can be mapped to the bubble size.

MSI is based on Lorenz-Mie Theory (LMT) which describes rigorously the scattering of light by a permeable sphere from a incident plane wave (Bohren and Huffman, 2008). Computation time increases with bubble size but can be approximated through Geometrical Optics (Hulst and van de Hulst, 1981). For bubble measurements these approximations have been shown to be valid for measurement angles of less than 80° between the light source and the sensor (Semidetnov and Tropea, 2003). Extensions to geometric optical approximations continue to be developed (Sentis et al., 2016), to enable the use of this method for larger angles. However, for MSI measurements based on mapping of the interference fringe frequency to a diameter the extended time for calculation is not an issue so that full Lorenz-Mie Theory can be used. Some implementations propose improvements in precision by using least-square-fitting of the interference pattern to theory

(Graßmann and Peters, 2004). However, this method is very sensitive to the experimental parameters, and uncertainty in their measurement at larger working distances can negate the improvement in precision.

Early work on MSI was for application in particle spray measurements, particularly in fuels (König et al., 1986; Skippon and Tagaki, 1996; Mounaïm-Rousselle and Pajot, 1999). Since then various modifications to the technique have been developed. A cylindrical lens can be incorporated to compress interference patterns in one dimension on the sensor (Maeda et al., 2000; Kobayashi et al., 2000; Qieni et al., 2014). This reduces overlap of the fringes when multiple particles/bubbles are present and thus increases the concentration limit of the technique. The use of laser light also lends itself to simultaneous particle-image velocimetry and size measurement (Kawaguchi and Maeda, 2005). Novel methods have also been proposed to measure the 3D location of droplets in addition to the diameter through an optical arrangement that shears the interference pattern as the distance away from the sensing plane increases (Brunel and Shen, 2013; Shen et al., 2013). Despite these extensions, calibration of the technique for use in hydrodynamic test facilities remains a challenge, and experimental measurements comparing MSI to other techniques exhibit differences in the size distributions (Quérel et al., 2010; Ebert et al., 2015; Boucheron et al., 2018; Birvalski and van Rijsbergen, 2018). Calibration in a cavitation tunnel using electrolysis to create bubbles approximately half the diameter of the wire found unexpected bubble sizes in the measurements (Lacagnina et al., 2011), and it was suggested that systematic calibration take place outside the main facility to identify the source of these errors and reduce uncertainties. At the core of the problem are the uncertainties in mapping the interference pattern measured by the camera to the precise angular range this represents. This is exacerbated when working over large distances such as in hydrodynamic test facilities. The most detailed treatment of sensitivity and uncertainty analysis for this process has been by Dehaeck and van Beeck (2007), where the measurement of experimental parameters such as the location of lens or sensor planes are attributed the largest source of error and uncertainty in these calibration experiments. Custom lenses or specialist optics knowledge can provide the required precision (Mées et al., 2010), but for a standard multi-element lens and cameras such data may not be accessible. Dehaeck and van Beeck (2007) examine multiple methods for calibration and full experimental calibration is identified as very accurate. This is not the final recommended method due to difficulty in finding mono-disperse generators and replicating the same optical configuration that will be used in the primary facility. We will present just such an experiment.

In addition to the calibration of bubble size, the effective measurement volume must be ascertained in order to convert size distributions into bubble concentrations. This correction is not widely discussed in literature but is critical as the small measurement volume of MSI changes with bubble size (Mées et al., 2010). A theoretical method to calculate the size dependent detection volume has been adapted from the Laser-Doppler Velocimetry technique (Ebert, 2015), and greatly alters the measured bubble concentration distribution (Ebert et al., 2016). Due to its sensitivity, errors in the volume correction may account for some of the discrepancies between measurement techniques reported in hydrodynamic test facilities (Lacagnina et al., 2011; Mées et al., 2010; Ebert et al., 2015). Systematic experimental investigation of the detection volume with bubble size is undertaken in these experiments and a method for calibration based on the approach by Ebert (2015) demonstrated.

The following section presents a summary of Lorenz Mie Theory and its approximations. The theory's implications for the measurement of bubbles in hydrodynamic test facilities are also discussed. We then demonstrate a method to produce mono-disperse microbubbles at concentrations suitable for measurement with both shadowgraphy and MSI in Sec. 4.4. This is accompanied by an experimental procedure to simultaneously measure a single microbubble with both techniques. This is used to rigorously calibrate MSI measurements (Sec. 4.5) and identify the detection volume (Sec. 4.6). Multiple frequency based MSI processing methods are discussed along with their implications for calibration. Uncertainties in both shadowgraphy and MSI are explored and MSI results are compared with theory.

4.3 Lorenz-Mie Theory

Although a conceptual understanding of the processes involved in the measurement technique does not require detailed knowledge of the mathematics behind Lorenz-Mie Theory, the selection of the scattering angle, collection angle, and the sampled scattered light polarization are assisted by connecting them to the theory. In addition, theory is often posed so that the coordinate system is defined independently of the incident light polarisation. While this abstraction is useful for analysis when the incident beam may be unpolarised, for highly polarised laser light this definition can cause confusion and obfuscate the choice of sampled scattered light polarization. A rigorous derivation of the far field intensity of light scattered by a bubble is provided by Bohren and Huffman (2008), the key components of which we will reproduce with minor changes to discuss the selection of parameters for measuring bubbles with polarised laser light.

Laser light propagates along the X axis and interacts with a bubble located at the origin (Fig. 4.1). The scattered intensity of light lobes in a complex pattern radiating outward to be captured by a camera. The angle between the beam and the vector from the bubble centre to the middle of the camera lens is termed the scattering angle, θ. The plane created by these two vectors forms the scattering plane. Deviating from the standard approach, we define the angle between the plane of polarisation of the laser and

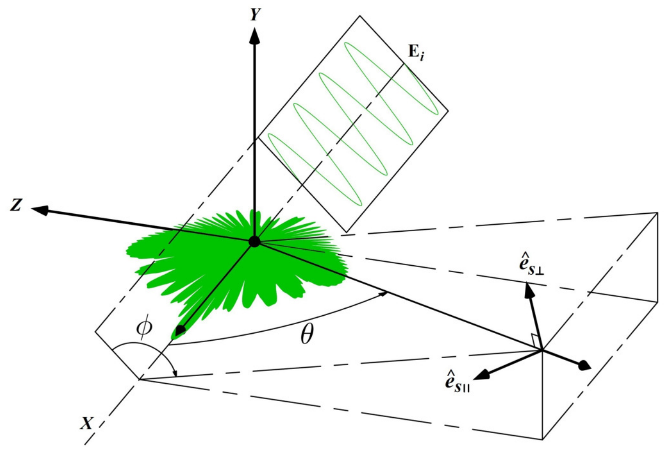

Figure 4.1: Angular distribution of scattered light from a bubble illuminated by a 532 nm plane wave (E_i) propagating along the X-axis. The scattering angle, θ, is the angle between the illumination source and the viewing direction. Logarithmic intensity distribution with scattering angle are shown for a sample plane in green. The polarisation angle ϕ indicates the angle between the polarised incoming laser beam and the scattering plane.

the scattering plane to be the polarisation angle, ϕ. We now seek to calculate the intensity of scattered light for any values of θ and ϕ, which will have a component polarised parallel to the scattering plane ($E_{s||}$) and a component normal to the scattering plane ($E_{s\perp}$). The range of θ in the scattering plane over which we measure intensity with our lens will be labelled α, our collection angle.

The dimensionless parameter, χ, describes the size of the bubble relative to the wavelength of light (λ) illuminating it and m is the ratio of the refractive indices of the two media, n_a and n_w for air and water, respectively.

$$\chi = \frac{2\pi\ n_w\ r}{\lambda} \qquad m = \frac{n_a}{n_w} \tag{4.1}$$

These parameters dictate the overall spacing between interference lobes of the scattered light and at which scattering angle they appear. If the particle was non-spherical or required treatment with complex refractive indices the calculations would be more elaborate, but in the ideal case the theory for a single bubble is summarised with the equation for the intensity of scattered light for two planes, parallel and normal to the scattering plane:

$$\begin{bmatrix} E_{s||} \\ E_{s\perp} \end{bmatrix} = E_i \frac{e^{ip}}{-ip} \begin{bmatrix} S_2(\theta) & 0 \\ 0 & S_1(\theta) \end{bmatrix} \begin{bmatrix} \cos(\phi) \\ -\sin(\phi) \end{bmatrix}, \tag{4.2}$$

where

$$S_1 = \sum^n \frac{2n+1}{n(n+1)}(a_n(\chi,m)\pi_n(\theta) + b_n(\chi,m)\tau_n(\theta))$$
$$S_2 = \sum^n \frac{2n+1}{n(n+1)}(a_n(\chi,m)\tau_n(\theta) + b_n(\chi,m)\pi_n(\theta)).$$

The scattering functions S_1 and S_2 are the truncated infinite sum of the scattering modes. They produce the intensity modulation the measurement technique utilises to size bubbles. It is observed from (4.2) that S_1 is associated with the light scattered from the bubble that is polarised perpendicular to the scattering plane, and S_2 parallel; this is not to be confused with the polarisation angle ϕ, although the relative intensity of S_1 and S_2 are a function of θ. The terms a_n and b_n are comprised of spherical Bessel functions, and the π_n and τ_n are constructed from associated Legendre polynomials. To investigate the components of these functions further does not enhance the discussion of the measurement parameters except to say that numerous computer codes exist to calculate numerically a_n, b_n, π_n and τ_n and we have used a particular MATLAB implementation by Mätzler (2002). It is however of interest to graph these scattering functions $I(a.u.)$ across a range of angles (Fig. 4.2) and point out some features.

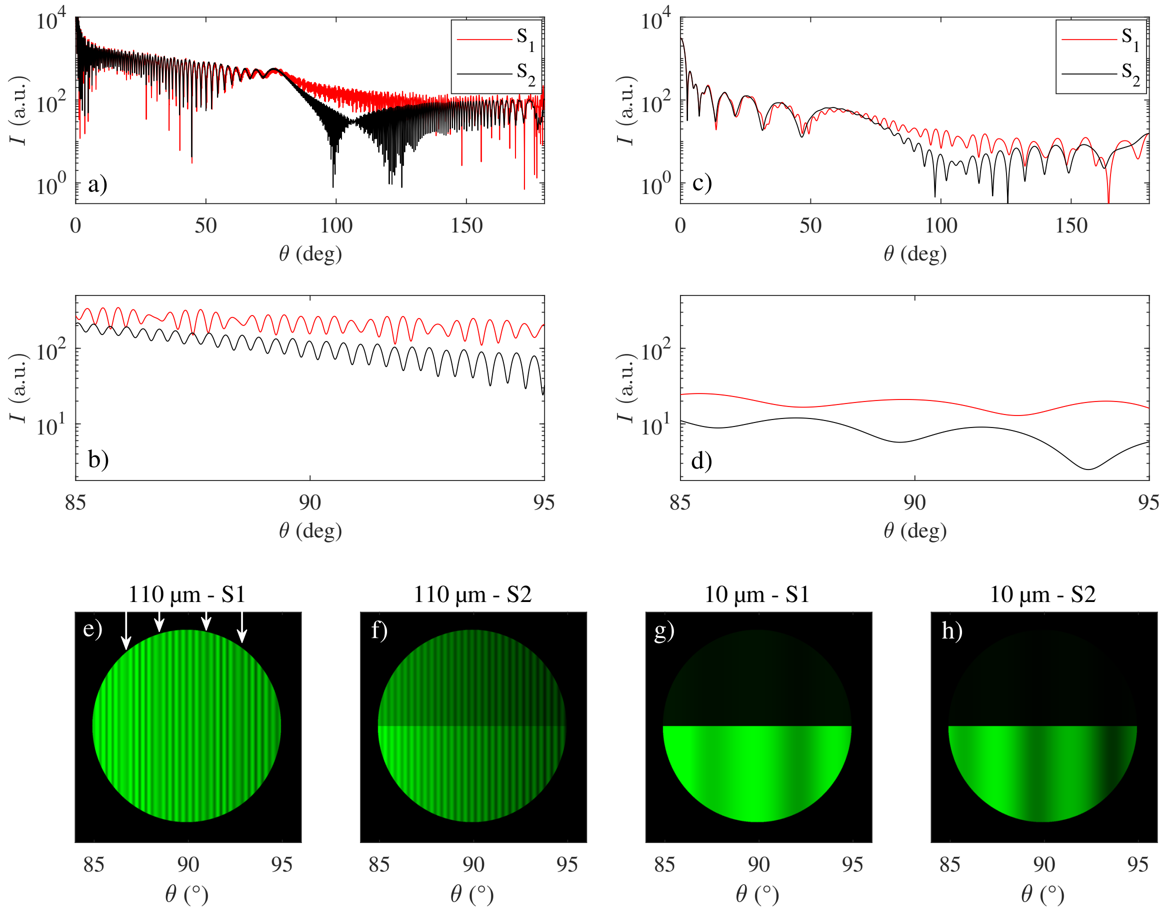

Figure 4.2: Intensity of scattered light for an air bubble in water illuminated with 527 nm light. The S_1 (red) and S_2 (black) polarisations are given in the top two rows for microbubbles with diameter 110 µm (left) and 10 µm (right). The second row is restricted to ±5° about the viewing angle. The bottom row has synthetic images of the scattering pattern as captured by a circular aperture with a 10° collection angle. The aberrant fringes in the S_1 polarisation are indicated by the arrows. For the top half of each synthetic image the relative brightness is untouched. For the bottom half of each synthetic image the brightness has been normalised to visualize the differences in frequency and intensity. The abbreviation *a.u.* stands for *arbitrary units*.

For a 110 µm bubble the greatest contrast between the darkest and brightest part of the interference fringes is achieved at a scattering angle of approximately $10 < \theta < 45°$ (Fig. 4.2a). However, for consumer lenses we are typically limited to a collection angle $\alpha \leq 10°$. For a 10 µm bubble the wavelength of the fringes are too large to be measured in this region with a 10° collection angle, the same is true for $\theta > 120°$ (Fig. 4.2b). A larger collection angle is then better as it limits the minimum detectable bubble size along with the measurement scattering angle. The design of custom lenses is of benefit (Lacagnina et al., 2011) but the specialist knowledge required may not be available to all hydrodynamic facilities. In any case, a region with high frequency oscillations is desirable as well as a lens with the largest collection angle. Fortunately, the measurement scattering angle of 90° lies in a region dense with fringes and is convenient for many experimental settings. While the selection of θ might be further optimised, angles other than 90° require a Scheimpflug lens arrangement to ensure the focal plane is parallel to the illumination plane, and may also introduce a working depth correction across the sensor (Quérel et al., 2010).

Comparing the two polarisations of scattered light for a 110 µm bubble in the region near 90° (Fig. 4.2c) the perpendicular S_1 component is brighter by an order of magnitude, and so would dominate the interference pattern if both components were present. However S_1 contains aberrant fringes resulting from surface effects (Pu, 2005; Sentis et al., 2016). These are seen in Fig. 4.2c at 87°, and 89° and less prominently at 91.5° and 93°. Later results show that their presence in the signal introduces greater uncertainty in size measurements as they degrade peak frequency extraction. However, S_2 alone can be measured by placing a polarising filter on the front of the camera lens. While the S_2 component has less variability in fringe wavelength, there is a rapid fall off in intensity across the region around 90°. To mitigate this experimental data can first be detrended, keeping in mind that for some measurements, one tail may drop into the noise floor of the camera sensor. The increased laser power requirements due to the decrease in scattered intensity of S_2 are usually inconsequential in most experimental settings. Clearly then we orient the laser to optimise measurement of the parallel polarisation. From Eqn 4.2 we can increase S_2 intensity and reduce S_1 by choosing $\phi = 0$. However, laser power is most stable when operating at maximum power. For lasers that are too bright at maximum power a polarising beam-splitter can be employed to dictate incident polarisation and reduce beam intensity.

LMT assumes a bubble is illuminated by an idealised plane wave of homogeneous intensity. Neither of these assumptions are strictly true. However for sufficiently small bubbles the scattering of light is not greatly affected (Albrecht et al., 2013). This is limited to bubbles where the intensity of light does not deviate by 5% across the bubble area so that for a Gaussian beam the bubble diameter should be less than approximately 20% the beam width. Experimental results by Hesselbacher et al. (1991) indicate a less stringent requirement than for droplets, at a scattering angle of 20° the diameter could be measured to an accuracy of better than 2% if the droplet diameter is smaller than the beam diameter. This describes an insensitivity in the interference pattern due to changes in illumination across the width of the microbubble, not the total intensity of light refracted by the bubble.

The mapping between the number of fringes N across an interference pattern and the bubble diameter can be derived from geometric optics in the case where $20° \leq \theta \leq 70°$ as

$$d = \frac{2N\lambda}{\alpha}\left(\cos\left(\frac{\theta}{2}\right) + \frac{m\ \sin\left(\frac{\theta}{2}\right)}{\sqrt{m^2 - 2m\cos\left(\frac{\theta}{2}\right) + 1}}\right).$$

While inappropriate at $\theta = 90°$, the mapping can still be approximated by a linear relationship with angular frequency (Boucheron et al., 2018). The most basic of which is posed as N, across measured collection angle α in Eq. 4.3a, but can also be expressed in terms of the angular wavelength of fringes $\bar{\lambda}_f$ as seen in Eq. 4.3b. The overbar in this context does not denote normalisation, as is the convention in quantum mechanics ($\bar{\lambda} \neq \lambda/2\pi$), but has been used to differentiate fringe wavelength from the wavelength of incident light. Experimental data will obtain the the wavelength in pixels $\bar{\lambda}_{px}$ which will be calibrated to an angular wavelength by C, an angular calibration constant the defocussed degrees per pixel.

$$d = \frac{KN}{\alpha} \qquad \frac{[\mu\text{m }°]\ [\,]}{[°]} \tag{4.3a}$$

$$= \frac{K}{\bar{\lambda}_{deg}} \qquad \frac{[\mu\text{m }°]}{[°]} \tag{4.3b}$$

$$= \frac{K}{C\ \bar{\lambda}_{px}} \qquad \frac{[\mu\text{m }°]}{[°\text{ px}^{-1}]\ [\text{px}]}. \tag{4.3c}$$

As discussed by Boucheron et al. (2018) the value of K changes with the wavelength of the laser. To calculate K and assess if the method of processing will influence the measurement, a series of 4000 intensity curves for bubbles of $d = 10 - 200$ µm with $\theta = 90°$, and $\alpha = 5°$ were generated. The overall trend line was subtracted to produce nominally zero-mean oscillations. Four methods were then used to extract the dominant wavelength: peak finding, auto-correlation, FFT, and wavelet analysis. Fig. 4.3a) shows a typical intensity series for a 100µm bubble. The detrended data is shown in red. The peak finding technique (Fig. 4.3b) used an inbuilt MATLAB algorithm to locate peaks of sufficient amplitude within the signal. The mean distance between the peaks was calculated to be the nominal wavelength. The second method used the first peak in the auto-correlation of the intensity series. (Fig. 4.3c) Sub-pixel resolution of the peak wavelength was achieved by fitting a spline to the seven points around the first peak and resampling at increased resolution. The third method (Fig. 4.3d) used a zero-padded FFT to increase the frequency resolution of the short series. The fourth method used wavelet analysis and a Morlet mother-wavelet to extract the dominant frequency by averaging the wavelength power across the interference pattern (Fig. 4.3f). Examples of the processing methods are shown in Fig 4.3a-f.

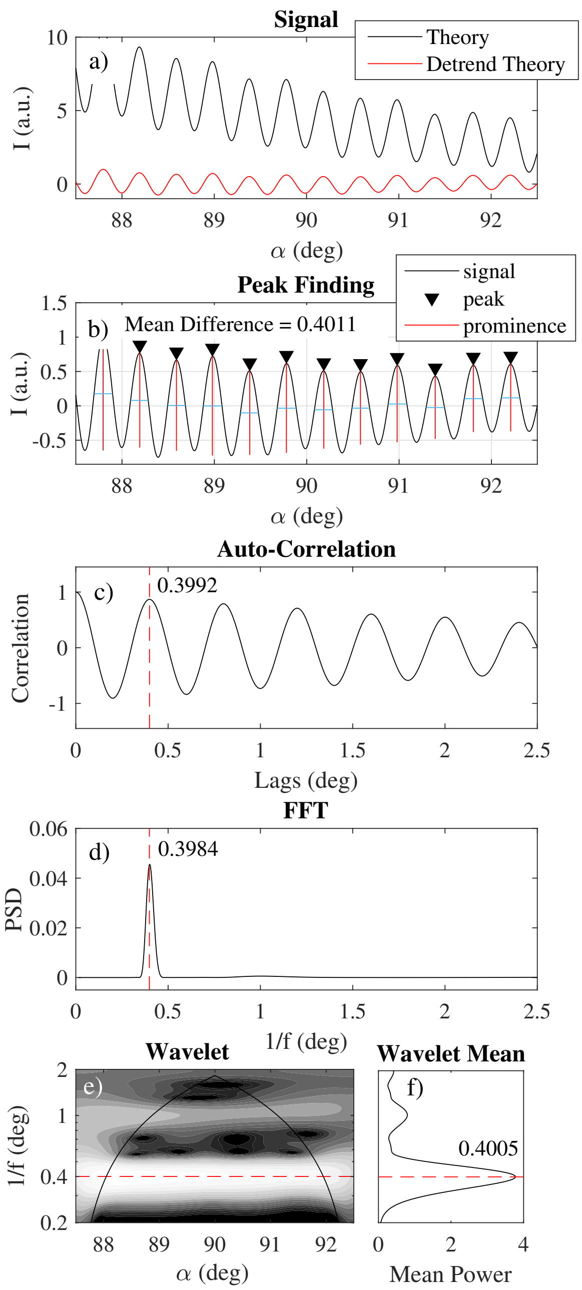

Figure 4.3: Review of methods used to extract the fringe wavelength for a theoretical intensity curve from a $d = 100$ µm bubble.

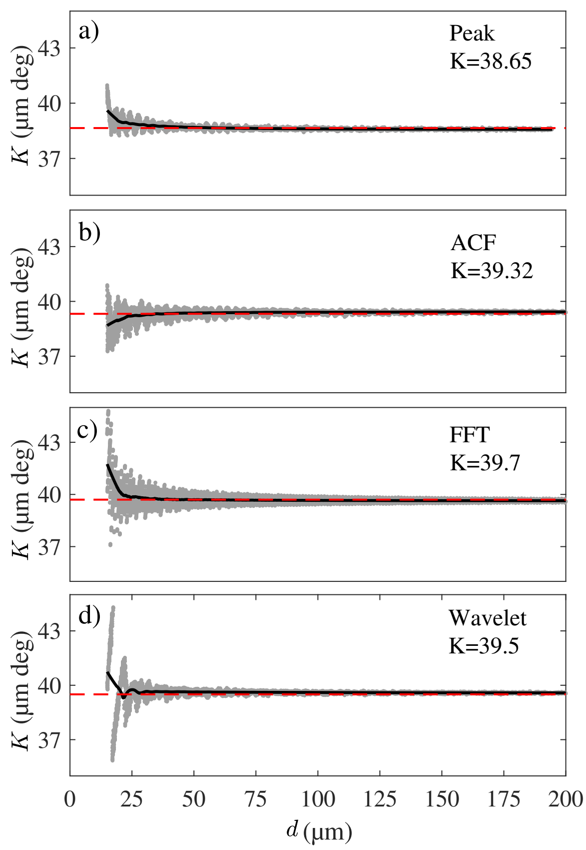

Figure 4.4: The conversion factor K is plotted against the diameter as processed from the theoretical scattering intensity. Nominal conversion values are listed for each method.

The value of K was calculated with each method by rearranging Eq. 4.3b. This was prudent as our implementations produced different results (Fig. 4.4). All methods showed increased scatter in the calibrated K value at small diameters but in general the auto-correlation exhibited the least variation. This is in part attributed to the up-scaling method applied. Although an extra step is included, auto-correlation is the preferred processing method as it is inexpensive to compute and reasonably insensitive to noise.

4.4 Experiment Details

The experiment was performed in a 0.6 m square, 0.9 m long stainless steel test chamber. A schematic of the experimental setup is presented in Figure 4.5. Two optical

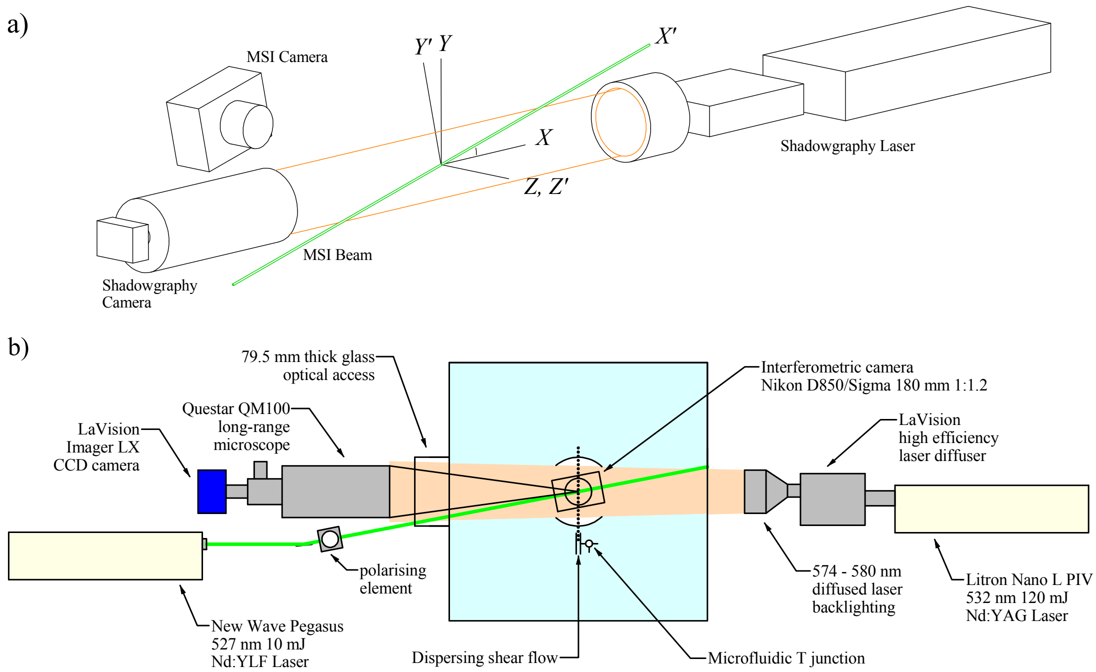

Figure 4.5: a) Experimental set-up and coordinate system. The coordinate system for MSI measurements X', Y', Z' is inclined by 13.36° about the Z-axis to accommodate shadowgraphy measurements perpendicular to the glass wall window. b) Schematic in the XY plane, viewed from the positive Z direction with further experimental details.

tables were positioned either side of the test chamber, to which the cameras and laser equipment were mounted. In-line Long-range Microscopy Shadowgraphy (LMS) equipment was placed either side of the test chamber. Backlighting was provided by a Lavision high-efficiency diffuser attached to a Litron Nano S 35-30-PIV Nd:YAG laser to produce a 4 µs pulse of diffused 574-580 nm light. A BK7 glass port 79.5 mm thick allowed optical access for a Lavision Imager-LX PIV camera mounted behind a Questar QM100 long range microscope with a 2x Barlow Lens. A custom nylon mount was manufactured so that a 62 mm polarising filter could be mounted to the end of the microscope objective to block the majority of light scattered by the bubble from the MSI laser which would otherwise be focussed onto the shadowgraphy CCD and potentially damage the camera sensor. Illumination for the MSI measurements was from a Litron Nano L 120-20-PIV

532 nm Nd:YAG laser. The beam was directed horizontally towards two Thorlabs NB1-K12 532 nm coated mirrors that redirected the light to 13.4° which finally passed through a Thorlabs CCM1-PBS25-532/M polarising beam splitter to control beam polarisation before entering the test chamber. The angle of 13.4° was set to provide beam access past the long range microscope and to avoid direct reflection on the measurement volume. The MSI beam passed through the same port used by the LMS receiving optics but low enough to ensure the light reflected by the glass port did not enter the long range microscope objective. A Nikon D850 DSLR with a Sigma 180 mm 1:2.8 APO Macro DG HSM lens and a Promaster HGX Prime 86 mm polarised filter was used to capture MSI data. This was mounted with a Linos rail system to the end of the tank behind a second glass port to form a scattering angle of 90°. The camera was rotated 13.4° so that the horizontal pixel pitch was inline with the direction of the MSI laser.

Acquisition triggering was performed using a Lavision PCI 9 programmable timing unit run by Davis 8 for the shadowgraphy camera and both the MSI and shadowgraphy laser. The trigger pulse for the MSI laser was split to pass through a delay generator before connecting to the MSI DSLR camera. A wiring schematic is presented in Figure 4.6 and data was acquired at 0.5 Hz. The MSI laser was triggered 8 µs after the shadowgraphy acquisition trigger to lower the risk of damage to the sensor but allow for simultaneous measurement of the bubbles by both techniques.

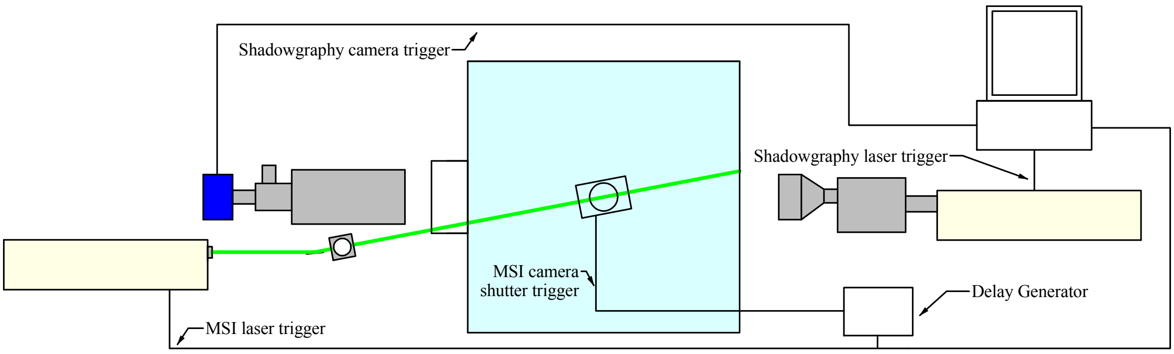

Figure 4.6: Wiring diagram for triggering illumination and image acquisition equipment.

Monodisperse microbubbles for the comparison of the methods were produced by Lamylec-L10 100 µm and 50 µm T-junctions from YLEC Consultants (Grenoble, France). These junctions accept a constant supply of pressurised air and water to generate a monodisperse train of bubbles from 30 to 130 µm in size at a rate of $\sim 10^3$ bubbles per second. A Proportion-Air (QPV1TBNISZP10BRGAXL) electronic regulator with a Prevost 1 µm air filter delivered pressurised air in the range of 0–10 bar to the junction. A second air regulator supplied pressure to a water reservoir, the pressurised water was then supplied to the T-junction. Fine adjustment of the supply pressures alters bubble production rate and bubble diameter. Typical operating pressures are approximately 3 bar for both supply fluids. To produce sufficient spacing between bubbles the train was fed into a circular laminar cross flow 1 mm in diameter. The laminar cross flow was induced by water flowing under gravity from a constant-head tank positioned above the main chamber. The water level in the head tank was kept constant by a miniature centrifugal RS-Components 702-6876 pump, with excess water returned via an overflow line to main chamber. The cross flow jet was ejected vertically at a velocity of ∼1 m/s into a quiescent tank, with the measurement location approximately 30 mm above the jet outlet. If the cross flow was too fast the bubbles would not enter the core of the cross flow and travel more slowly near the passage walls where coalescence may occur. If the cross flow was too slow the bubbles may not be spaced appropriately. A schematic of the bubble generation and dispersion method is shown in Fig. 4.5(b). The T-junction and cross flow outlet were mounted to an acrylic arm. Precise 3D positioning of the arm was possible through three Melles-Griot 25 mm linear stage micrometres attached between the arm and its mounting position outside the tank.

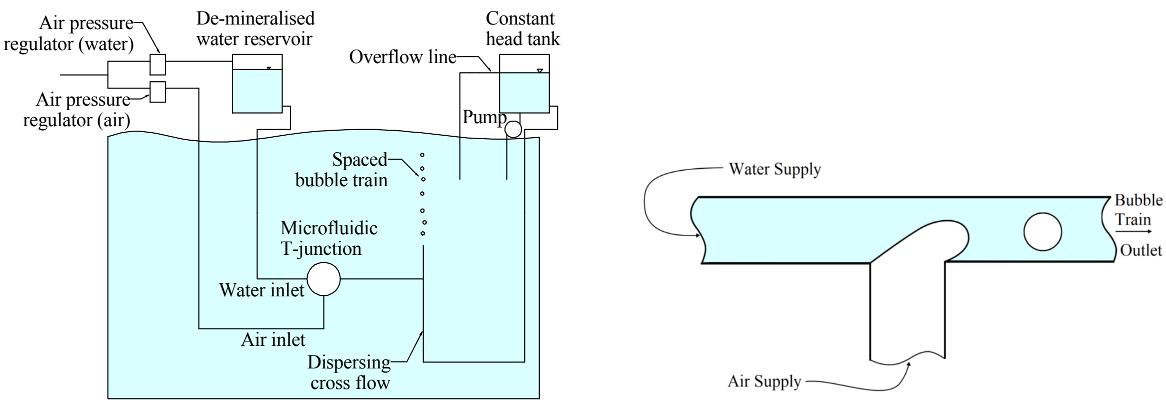

Figure 4.7: Schematic of the bubble generation and dispersion apparatus.

The shadowgraphy measurements were acquired and processed using DaVis 8. To calibrate the system the acrylic arm and bubble generator was removed and the shadowgraphy system brought into focus on a glass calibration plate placed in the centre of the both optical access windows. Precise dots printed on the plate calibrated the magnification factor and bubble sizing parameters for the shadowgraphy measurements. Zoomed sections of the calibration images are shown in Fig. 4.8a-d. Diffraction effects on the bubble edges are visible and their relative intensity is more noticeable on the smaller calibration dots. The pixel intensity was sampled horizontally through the centre of the dot and plotted in Fig 4.8e. The effects of diffraction reduce the minimum pixel intensity and round the edges of the profile but otherwise agree well when normalised by minimum intensity and nominal bubble radius (Fig 4.8f). The histogram of dot diameters measured using optimised parameters from the calibration plate are shown in Fig 4.8g. The spread of the measured dot diameters around the known size gives an uncertainty estimate of ±2 µm for the shadowgraphy measurement.

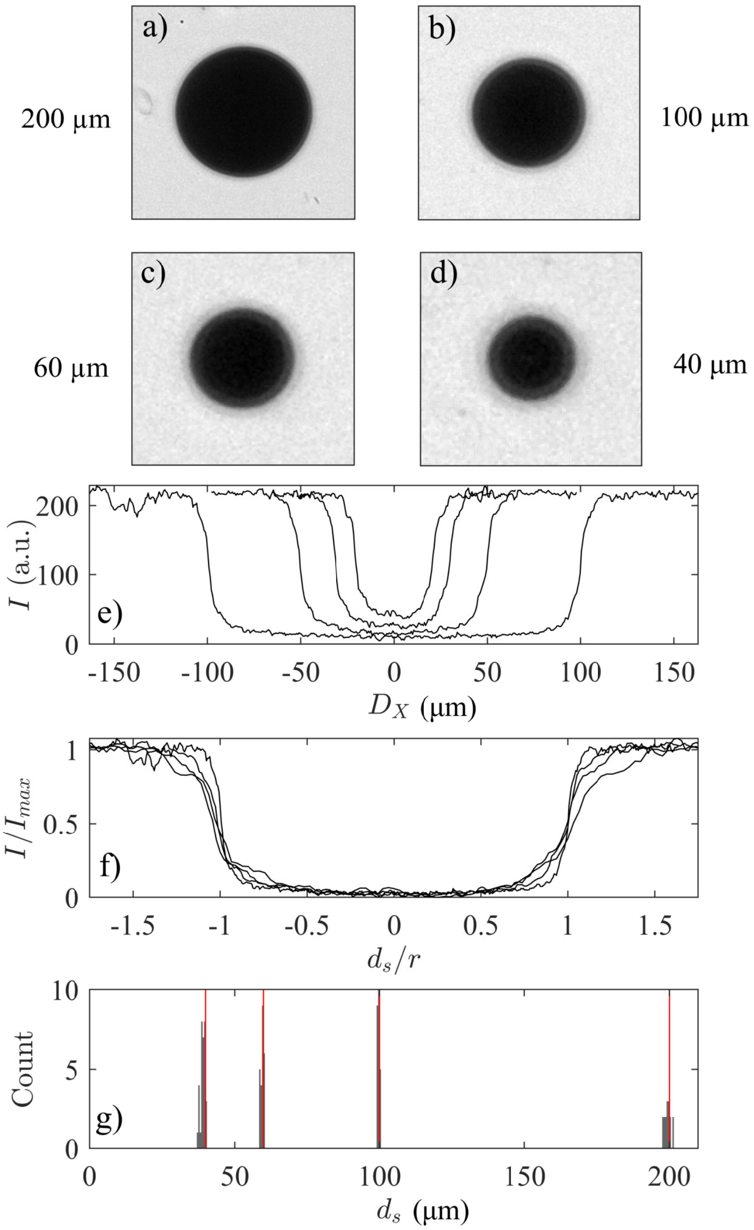

Figure 4.8: A series of images and plots showing the calibration of the shadowgraphy images from a glass reference plate. Four example calibration dots of different size are extracted at different levels of zoom (a-d). Pixel intensity across dot centre are plotted e). Normalised pixel series (f). Histogram of measured dot diameters for the calibration plate are presented (g).

The MSI laser was then aligned to intersect the same location on the calibration plate. The bubble generation apparatus was then returned and positioned to be in focus for the shadowgraphy measurements. To confirm that the measurement volumes were coincident, the polarisation filter was removed from the shadowgraphy microscope objective and in simultaneous MSI and shadowgrahy measurements, with the MSI laser at low power, back scattered light from the MSI laser was observed using the shadowgraphy camera (Fig. 4.9). The depth of focus of the shadowgraphy equipment was small so that although focussed at the mid-plane of the bubbles, the backscattered light from front of the bubble is slightly out of focus. To measure the defocus distance of the MSI system a target plate was traversed along the Z axis from the bubble plane to the MSI camera focal plane using an electronic linear microstage. The uncertainty on the measurement of the defocus distance was ±0.2 mm.

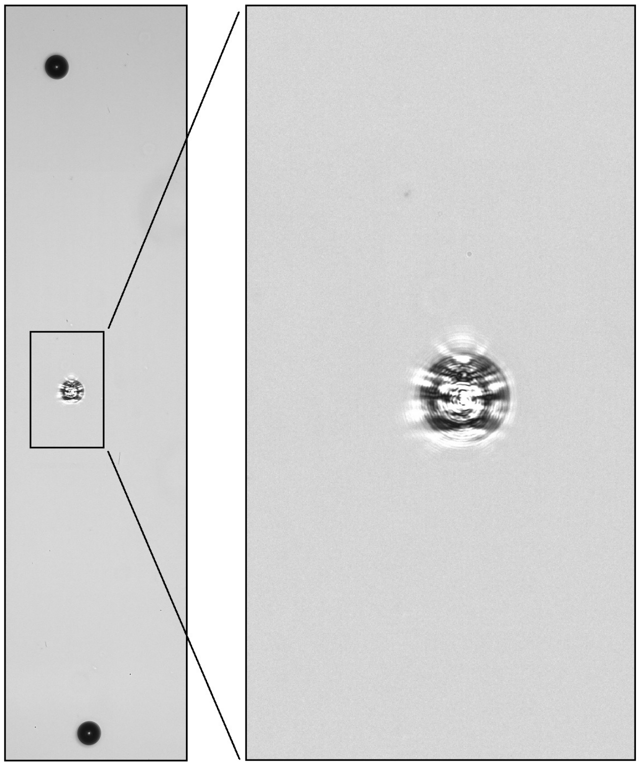

Figure 4.9: Sample shadowgraphy image showing three 109 µm bubbles in the train. With the polarisation filter removed from the shadowgraphy camera, the MSI laser backscatter from the middle bubble is imaged, validating direct simultaneous measurement.

To capture a data set the air and water supply to the bubble generators were configured to produce the bubbles of the desired size. Sample shadowgraphy data was examined for a period of 5 minutes to assess bubble size spread and inter-bubble spacing. When appropriate bubble size and spacing characteristics were achieved 100 simultaneous MSI and shadowgraphy image pairs were captured. Figure 4.10 displays a typical shadowgraphy and MSI pair.

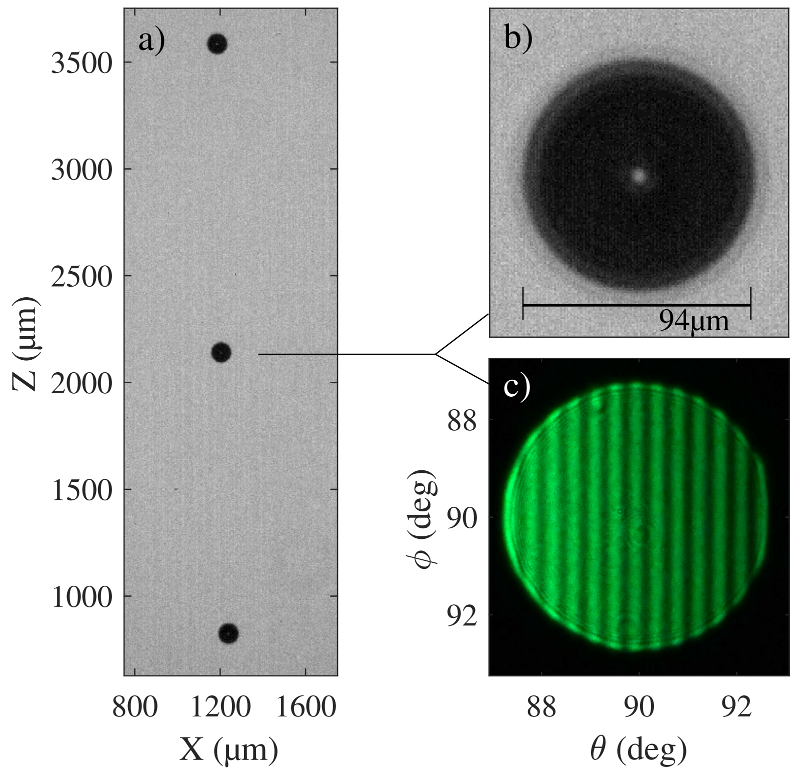

Figure 4.10: Sample shadowgraphy and MSI picture pair for a 94μm bubble. The magnified region shows the same bubble that is illuminated in the MSI picture.

4.5 MSI calibration and Results

The polarising filter in front of the MSI camera could be adjusted to capture either the perpendicular or parallel polarised components of the light scatter by a bubble. The different features predicted by theory in each polarisation of the scatter light, see Sec. 4.3, were experimentally validated in Fig. 4.11. These data confirmed that parallel polarised light has greater homogeneity in wavelength when decomposed so that there is less scatter in the measured wavelength with size. Fresnel diffraction about the limiting aperture was also observed which needed to be accounted for in calibration.

The defocus distance, and therefore the observed disc width, was varied by moving the camera and lens together on a linear rail in the Z-direction. It can be seen from Fig. 4.12 that the interference pattern can be normalised for a single bubble size by the interference disc width. The perpendicular polarisation was chosen for these measurements so that the presence of aberrant fringes were visible to help distinguish one fringe from its neighbor. The size of the defocus disc sets the maximum bubble size as the Nyquist limit is reached for the number of pixels per fringe wavelength. A competing requirement is that larger interference discs are more likely to overlap and so the measurable concentration limit decreases with disc size. The choice of disc size is then a function of the size and concentration ranges present. While perhaps undesirable it will be shown that post measurement calibration of the technique is possible so that the defocus distance can

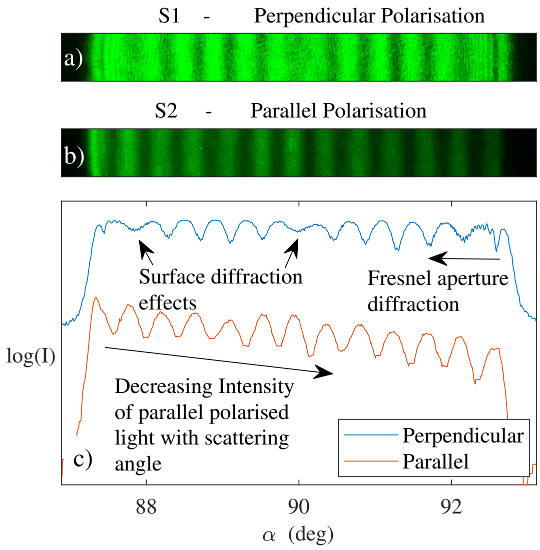

Figure 4.11: MSI images for both S_1 (perpendicular, a) and S_2 (parallel, b) polarised light. The average intensity is given in (c), showing that S_2 is in general darker but has a more consistent wavelength across the collection angle.

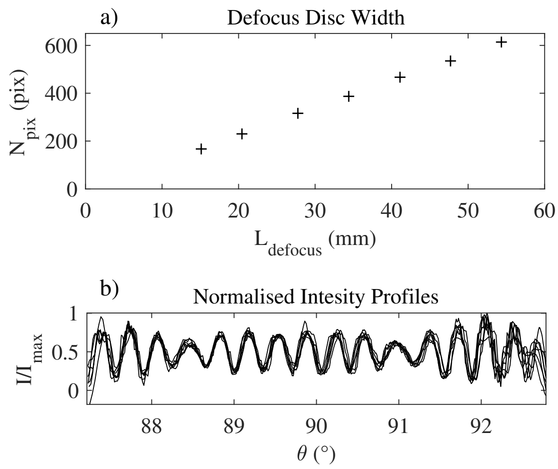

Figure 4.12: The interference disc size in pixels (D_{pix}) as a function of the off-focus distance (L_{defocus}) of the camera and lens combined (top). Below, the normalised intensity profiles for perpendicularly polarised light are plotted showing an invariant profile with defocus distance.

be varied until the concentration is measurable by the system. The aliasing of data will not go unnoticed as the intensity of scatter light increases with bubble size so that the presence of bubbles too large to be measured are identified by their intensity. Methods to screen these data are discussed by Ebert (2015) and Ebert et al. (2016).

To calibrate MSI there needs to be a mapping from the interference pattern in pixels to the angular scattering region this represents. One common approach is to measure the collection angle α, and observation/scattering angle and infer the region of measurement (Graßmann and Peters, 2004). In standard camera lenses the precise diameter of the limiting aperture is unknown and cannot easily be measured. In order to determine α accurately a new aperture whose width could be precisely measured was placed in between the bubble and the camera to mask the interference pattern. The width of the interference pattern in pixels then corresponds with the collection angle centered over the principle scattering angle of the camera. For bubble measurements it is advantageous that this aperture is located in the water so that the exact refractive index of the water, and more importantly glass, need not be known. However, the measurement of the interference pattern width in pixels directly is prone to error (Dehaeck and van Beeck, 2007). Diffraction around the aperture edge in conjunction with the same intensity oscillations we wish to measure make resolving the true location of the geometric edge difficult. This can be circumvented by measuring the height of the interference pattern, but resolving the location of the geometric edge still posed a problem.

From Fresnel diffraction theory the intensity level at the geometric boundary location is 1/4 the unperturbed maximum intensity. A rectangular aperture was placed in the test chamber and three vertical series were extracted from a sample image to measure the height in pixels and are compared in Fig. 4.13. One from the brightest part of a fringe, one from a dark band of the fringes, and the third series was constructed by taking the mean intensity across the image sample. The location of the edge agreed well but the bright and dark pixels series are subject to pixel noise so that the mean intensity series was preferred. This method was then applied to a sample of 160 interference patterns. The histogram of results showed a spread of interference pattern widths (see Fig. 4.14).

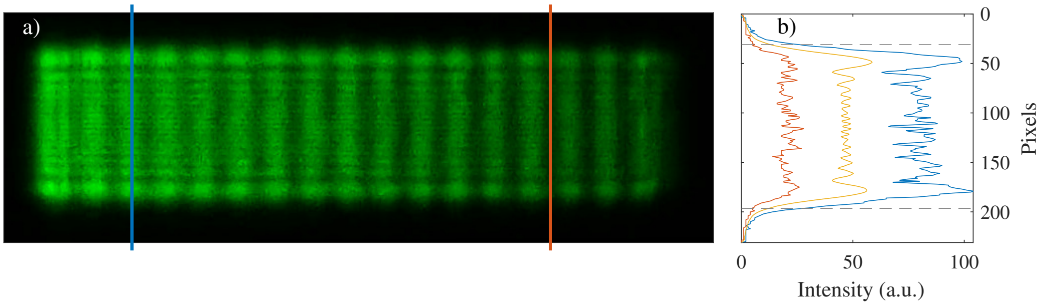

Figure 4.13: (a) An interference pattern for scattered light clipped by a rectangular aperture placed in the water between the bubble and the camera lens. (b) Vertical intensity profiles are plotted for the blue and orange locations in a) as well as the horizontal mean intensity (yellow).

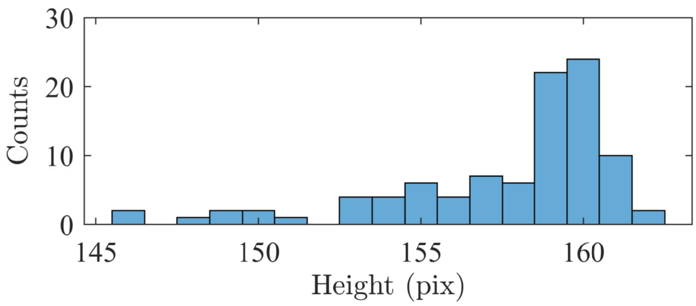

Figure 4.14: A Histogram of measured interference heights for 160 sample images using the method from Fig. 4.13

An alternative method was implemented in order to avoid the need to find a geometric edge. Instead diffraction was used to our advantage. Two holes were machined in a thin plate which was then placed in the path between the camera and the bubble, (see Fig 4.15), similar to the limiting aperture method above. Aside from the geometry of the 'aperture' the only difference was now that the radial symmetry of the holes caused diffraction to create a series of concentric rings with a bright or dark spot in its centre (Fig. 4.16). The distance in pixels between circle centers was able to be more accurately measured that locating the diffracted geometric edge. The calibration constant C was then calculated by,

$$C = \frac{\alpha}{D_{pix}} = \frac{2\arctan(\frac{O}{A})}{D_{pix}}, \tag{4.4}$$

where O is the half distance of the aperture width, A the distance from the bubble to the limiting aperture, and D_{pix} the spacing between circle centers. Results for three aperture locations are tabulated below and agree well (Tab. 4.1).

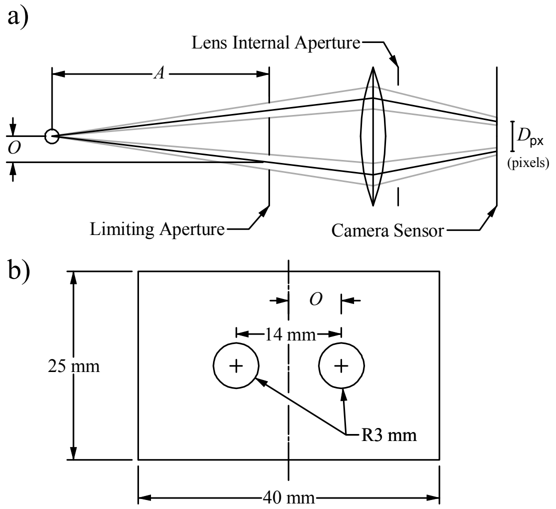

Figure 4.15: (a) A schematic of the optical arrangement for the angular calibration. O is the half distance between the apertures, and A is the distance between the bubble and the mask plate. (b) The mask plate used in the angular calibration.

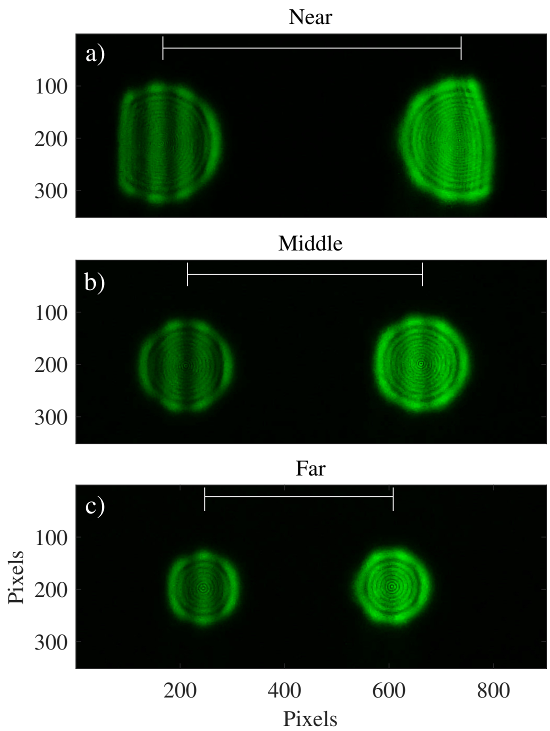

Figure 4.16: Calibration images taken at three different distances (A in figure ref). The angle is reduced between the two apertures as the plate is moved farther from the bubble train.

Table 4.1: Calculations for calibration constant C for three distances from the bubble plume, presented also as $1/C$ for readability.

	$D_{aperture}$ (mm)	α_{holes} (°)	D_{pix} (pix)	C (°/pix)	$1/C$ (pix/°)
Near	181	4.43	570.5	776e-5	128.8
Middle	229	3.50	450.0	778e-5	128.5
Far	285	2.81	360.5	780e-5	128.1

With both measurement systems calibrated, the pressure of the air and water supplied to the T-Junction was varied to produce single bubble measurements ranging from ≈ 30–140 µm in diameter. The diameter measured by both techniques are plotted against one another in Fig. 4.17. The difference in measurements varied by less than 1 µm. This gives confidence in the methods of calibrating and calculating the constants C and K, particularly as these were accomplished using separate information. It would otherwise be easy in calibration for the bias of one constant to propagate into the other, as discussed by Dehaeck and van Beeck (2007). From the theoretical calculation and plotting of K

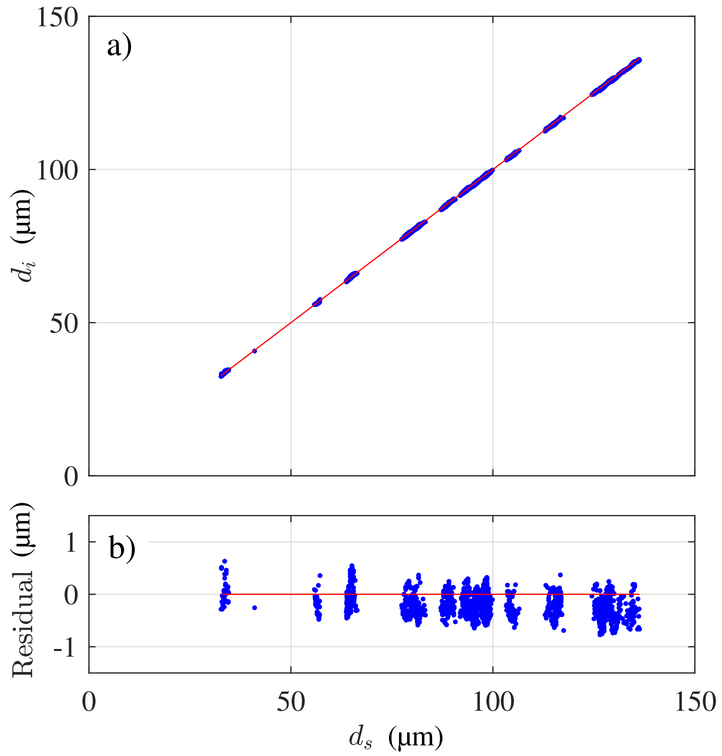

Figure 4.17: (a) The size measured with MSI (d_i) is plotted against the size measured with shadowgraphy (d_s). (b) The residual ($d_i - d_s$) is plotted below with less than 1µm difference between the measurements.

with size in Fig 4.4 there is greater uncertainty in K for small diameters. Further, there are less fringes across a single measurement so that there is greater uncertainty in the fringe wavelength. Uncertainty estimates for two bubble sizes are presented in Tab. 4.3. The uncertainty in C is constant and taken from Tab. 4.2. For small bubbles uncertainty in the measured fringe wavelength was estimated to be to within 1 pixels. For larger bubbles where many fringes can be sampled averaging allows for a sub pixel estimate of uncertainty.

Table 4.2: Linearised estimate of the uncertainty in the calculated calibration constant C.

x	units	x_{est}	U_x	$\left\lvert \frac{\partial C}{\partial x} \times U_x \right\rvert$	$\%U$
A	(mm)	181	± 0.5	3.39×10^{-5}	48.1%
D_{pix}	(px)	360.5	± 1	3.41×10^{-5}	48.7%
O	(mm)	7	± 0.005	8.77×10^{-6}	3.2%
			U_{total}	4.89×10^{-5}	(°/pix)

Linearised estimates of uncertainty in d indicate that for small bubbles uncertainty in K dominates. For $d = 110$ µm the primary uncertainty is the wavelength measurement, though more evenly distributed. In any case, the shadowgraphy measurement uncertainty of 2 µm is bigger for both sizes. The minimum detectable bubble size (d_{min}) will depend

Table 4.3: Linearised estimate of the uncertainty in the calculated diameter for a 10 and 110 µm bubble.

10 µm

x	units	x_{est}	U_x	$\left\lvert \frac{\partial d}{\partial x} \times U_x \right\rvert$	$\%U$
K	(µm deg)	39.32	±2	0.499 µm	98.3%
C	(°/px ×10^{-5})	778	±4.89	0.062 µm	1.5%
λ_{px}	(px)	515	±1	0.019 µm	0.2%
			U_{total}	0.503 µm	

110 µm

x	units	x_{est}	U_x	$\left\lvert \frac{\partial d}{\partial x} \times U_x \right\rvert$	
K	(µm deg)	39.32	±0.22	0.617 µm	16.5%
C	(°/px) ×10^{-5}	778	±4.89	0.693 µm	20.8%
λ_{px}	(px)	45.8	±0.5	1.204 µm	62.7%
			U_{total}	1.52 µm	

on the collection angle of the system. To attempt correlation a minimum of 1.5 cycles is needed across the interference pattern. From equation 4.3a) and a collection angle $\alpha \approx 5.5°$ this corresponds to $d_{min} = 10$ µm. The largest detectable bubble is limited by either saturation of the image sensor, by the Nyquist criterion when the number of wavelengths is half the number of pixels across an interference pattern, or when bubble become aspherical at sizes above 200 µm in diameter.

4.6 Volumetric Concentration

To accurately calculate bubble concentration the measurement volume for each bubble size must be determined. The intensity of an MSI interference pattern is proportional to the intensity of incoming light as well as the 2D projected area of the bubble. Consequently, a large bubble may receive enough illumination across the full beam width to be measured, whereas a smaller bubble might only be recorded when in a narrow region at the centre of the beam, Ebert et al. (2016). To examine this problem in detail bubbles were measured at various locations in the YZ plane, a cross-section of the MSI beam.

Bubbles were imaged with both shadowgraphy and MSI as they rose through the measurement volume. They were randomly located in the Y direction and systematically varied in the Z direction using a micro stage. The intensity of an interference pattern was established to be the 95th percentile of the pixel series data (Fig. 4.18). A series of 1000 images was recorded for four bubble sizes and the jet outlet moved in 5 µm increments along the Z axis. The interference pattern intensity for one bubble size has been plotted as a function of position in Fig. 4.19a. The beam profile after passing through the chamber was expanded and captured using a DSLR camera, shown for reference in Fig. 4.19b.

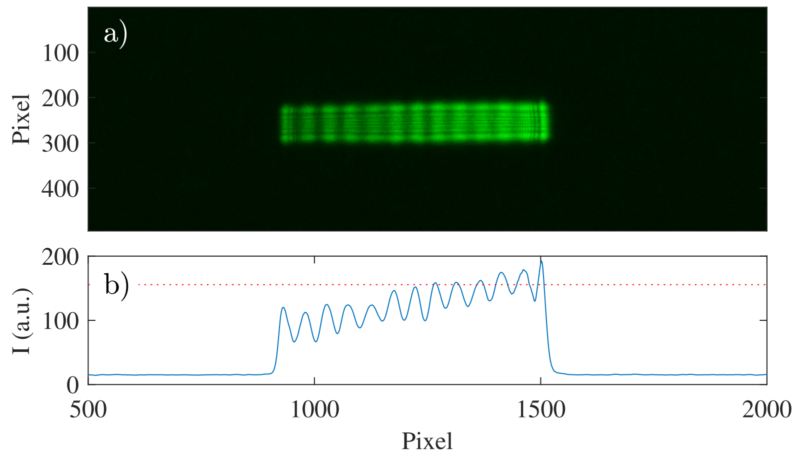

Figure 4.18: a) Example interference pattern. b) Extracted pixel series. The red line indicates the 95^{th} percentile, taken to be the representative intensity of the interference pattern.

Before testing the beam profile emitted from the laser head was measured and produced a radially symmetric and highly Gaussian profile. Beam optics and the angle at which the MSI beam entered the test chamber have clearly modified this beam shape. This may have implications for MSI configurations at angles other than $\theta = 90°$. None-the-less, data in Fig. 4.19a compares well to the reference beam measurement Fig. 4.19b. In the future the beam will enter perpendicular to the glass port, but could not in this experiment without interfering with the shadowgraphy equipment. Whilst the shadowgraphy could be used to measure the effective beam width, a method that uses the measured beam profile and MSI data alone is outlined and validated using the available measurements.

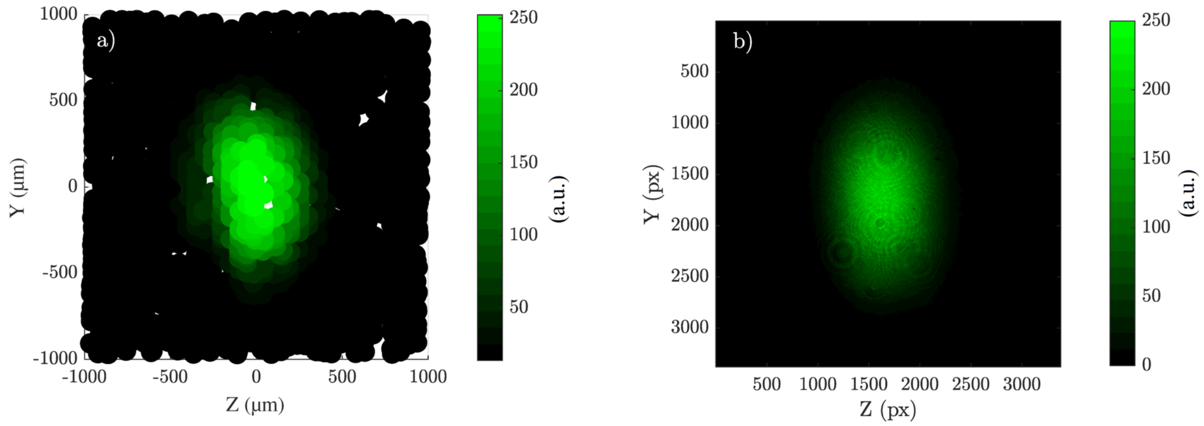

Figure 4.19: a) Intensity of the scattered MSI light as a function of the spatial position of the bubble. b) Expanded beam profile.

For a practical measurement a beam-profiler can be placed at the same optical path length as the measurement volume from the laser head. The profile does not need to be Gaussian in shape. The centroid of an interference pattern in an MSI photograph can be related to its location in the beam (Fig. 4.20). The lens geometry and defocus distance will determine the magnification factor of an image at the illumination plane.

Movement of the centroid in an image is mapped to its location across one dimension of the beam profile. With a large number of images, bubbles in a narrow size range can be interrogated to estimate the location at which the scattered light intensity is below the cutoff ($Y_{crit}(d)$). The maximum intensity across the beam profile at Y_{crit} can then then determined. A contour of the beam profile at this intensity value determines the effective beam area and the subsequent measurement volume.

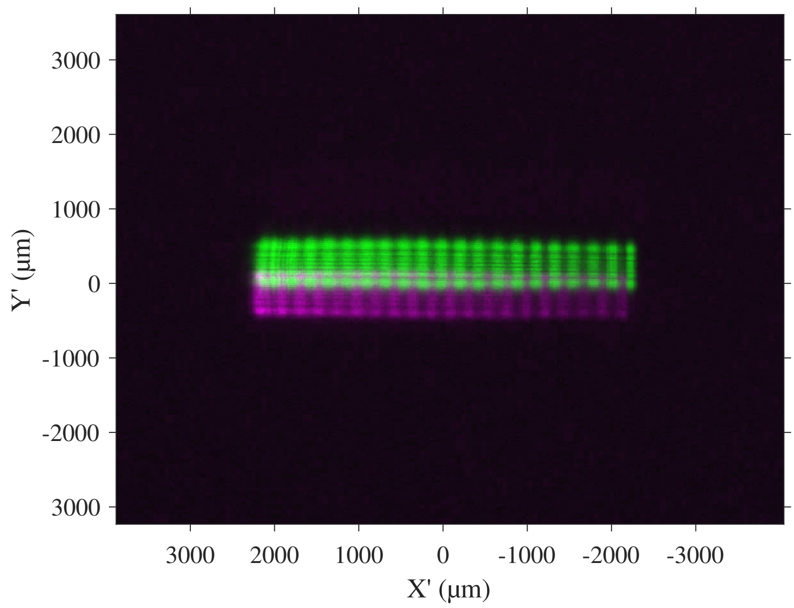

Figure 4.20: Two MSI images superimposed demonstrate the shift in interference pattern as the location of the bubble varies within the MSI beam.

To validate the approach we compare results using this method to data with the location known through shadowgraphy. First the Y location for MSI interference patterns are calculated from 2D cross-correlation of a rectangle template the same dimensions as the interference pattern with MSI photographs. Maxima of the cross-correlation identify bubble locations and are scaled by the magnification factor at the beam plane. Bubbles located via shadowgraphy are mapped to the MSI image and the intensity extracted. The Y-location and intensity are plotted for data extracted via MSI alone and shadowgraphy in Fig. 4.21. The two methods compare well and a sample fit is plotted for the shadowgraphy data. This process was repeated for four bubble sizes. A plot of the intensity profiles extracted from MSI data along with a fit to the data are presented in Fig. 4.22. The minimum intensity threshold was set to be $I_{min} = 50$ which has also been plotted as the red dotted line. Contours for the location of I_{min} for each of the bubble sizes are plotted in Fig. 4.23. These data are summarised as the effective beam width and beam area in Fig. 4.24.

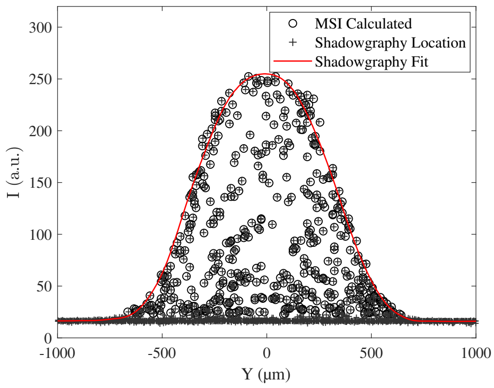

Figure 4.21: A plot of Y-location against interference pattern intensity comparing the shadowgraphy and MSI methods.

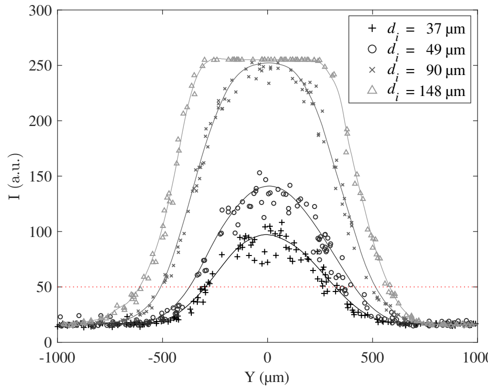

Figure 4.22: Intensity profiles for four bubble sizes along the Y axis at $Z = 0$. The best fit surface for the intensity map is also plotted for this cross section of the profile.

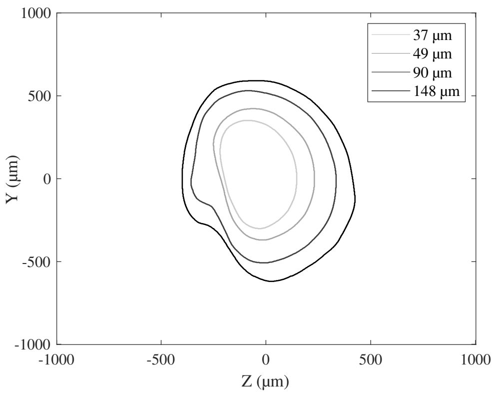

Figure 4.23: Contours of the beam area defined by the cutoff intensity threshold for four different bubble sizes.

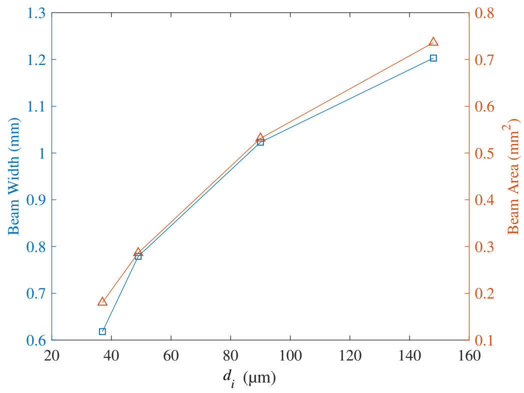

Figure 4.24: The effective beam diameter and area are plotted against bubble diameter for four bubble sizes.

4.7 Conclusions

The MSI technique has been investigated using simultaneous shadow imaging of individual mono-disperse microbubbles. The use of parallel polarisation was chosen instead of perpendicular at 90° scattering angle giving more uniform fringe spacing yielding greater precision despite the lower intensity. Calibration of the imaged fringe pattern was derived from two constants. The constant of proportionality between the scattering bubble diameter and the angular wavelength was determined from Lorentz Mie theory. A practical calibration for the second constant of proportionality between the scattering angle and imaged length is demonstrated. The comparison of the measured diameters by shadow and MSI by this approach within the range 30–150 μm is less than 1 μm. The diameter dependant effective measurement volume can be determined from the measured ensemble population if the beam profile is axisymmetric, or for an arbitrary beam shape if the profile is measured independently. A rationalised approach for the application of the MSI technique in water tunnels or other hydrodynamic test facilities using conventional laser diagnostic equipment is demonstrated. Although bubbles below 30 µm were not tested the method is applicable to sizes below 10 µm but with increased uncertainty. The approach is applicable for measurement of microbubbles in the diameter range 10–175 µm and for concentration ranges up to 10–100 mL^{-1}.

4.8 Acknowledgements

This project was supported by the Defence Science and Technology Group (Dr. Dev Ranmuthugala and Mr. Matthew Khoo), the University of Tasmania, and the US Office of Naval Research (Dr. Ki-Han Kim, Program Officer) and ONR Global (Dr. Pae Wu, Dr Sung-Eun Kim) through NICOP S&T Grant no. N62909-15-1-2019.

Chapter 5

Measurement of Nuclei Seeding in Hydrodynamic Test Facilities

This chapter is article form. (Russell et al., 2020a) The citation for the publication is, Russell, P. S., Barbaca, L., Venning, J. A., Pearce, B. W., & Brandner, P. A. (2020). Measurement of nuclei seeding in hydrodynamic test facilities. *Experiments in Fluids*, 61(79). https://doi.org/10.1007/s00348-020-2911-2

The contributing authors are:
Russell, P. S., Barbaca, L., Venning, J. A., Pearce, B. W., and Brandner, P. A.

5.1 Abstract

Microbubble populations within the test section of a variable pressure water tunnel have been characterised for various operating conditions. The tunnel was operated with demineralised water and artificially seeded with microbubbles from an array of generators located in a plenum upstream of the tunnel contraction. The generators produce a polydisperse population of microbubbles 10–200 µm in diameter. The microbubbles are generated from supersaturated feed water within a confined turbulent cavitating micro-jet. The generator and tunnel operating parameters were systematically varied to map the range of nuclei concentrations and size ranges possible in the test section. Microbubbles were measured with Mie-Scattering Imaging (MSI), an interferometric sizing technique. A new method was introduced to calibrate the detection volume and extend the dynamic range of the MSI. The acquisition and processing of microbubble measurements with MSI have a fast turn-around such that nuclei concentration measurements are approaching real-time. Estimation of the total bubble concentration was within 5% of the statistically converged concentration after only 100 detections but 10^4 were necessary for full

histogram convergence. The tunnel is operated with water at low dissolved gas content to ensure all injected microbubbles dissolve and do not complete the tunnel circuit. As a result of this the injected population is altered by dissolution as well as pressure change during the short residence between plenum and test section. The transformation is shown to be complex, changing with tunnel operating conditions. The measured test section nuclei populations were found to follow a power law for the higher concentrations. Test section nuclei concentrations of 0–24 mL^{-1} can be achieved through variation of generator and tunnel operating parameters.

5.2 Introduction

Microbubble disperse flows are intrinsic to surface oceanography and naval hydrodynamics as they control, or interact with, many phenomena and processes of interest including cavitation inception and dynamics, gaseous diffusion, noise generation, acoustic and shockwave propagation and turbulence. With regard to cavitation, microbubbles provide nuclei that control the inception and dynamics of unsteady cavitation; but cavitation itself is also a prolific source of microbubbles by its very nature. Modelling of these flows experimentally remains a challenge as microbubble concentrations and size ranges may vary over several orders of magnitude. To this end, several techniques for generating and measuring microbubbles have been developed in the Cavitation Research Laboratory (CRL) at the Australian Maritime College (AMC) (Brandner, 2018). Sample results from these techniques for measuring cumulative microbubble or nuclei populations in the AMC cavitation tunnel are shown in Fig. 5.1. Overall concentrations and sizes range over 10 and 5 orders of magnitude respectively. The population with the largest concentrations and sizes is typical of that in the wake of a cavitating object at relatively high Reynolds numbers (Russell et al., 2018). This population of high concentration/larger microbubbles has been measured using Long-range Microscopic Shadowgraphy (LMS). The most sparse population shown in Fig. 5.1 is typical of the background or naturally occurring nuclei population ever present in the AMC cavitation tunnel under normal operating conditions. These nuclei cannot be measured using optical techniques due to their small sizes and low concentrations. These have been measured via mechanical activation using a Cavitation Susceptibility Meter (CSM) (Khoo et al., 2017). The intermediate population is representative of a test flow artificially seeded with a modest concentration of microbubbles in the size range 2 to 200 µm for experimental modelling of cavitation inception. It is the characterisation of these intermediate populations within cavitation tunnels that is the subject of the present work.

The measurement of micro-bubble concentrations on-the-order-of 0-1 cm^{-3} is challenging with in-focus imaging, as discussed in a review paper on optical measurement

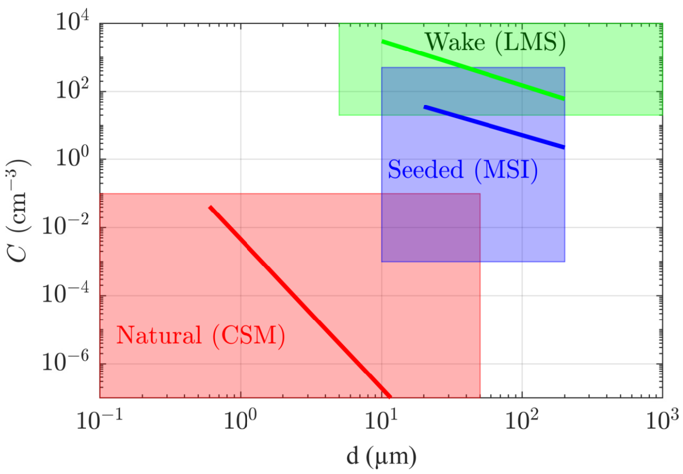

Figure 5.1: Nuclei distribution graph showing the bubble diameter, d, and concentration, C, ranges (shaded regions) for which practical measurements can be made using the Cavitation Susceptibility Meter (CSM), Mie Scattering Imaging (MSI) and Long-range Microscopic Shadowgraphy (LMS). Optical methods (e.g. IMI and LMS) are more suitable for higher concentrations of larger bubbles, while mechanical activation (CSM) is suitable for lower concentrations of smaller bubbles. The lines represent recent nuclei measurements at the AMC cavitation tunnel.

techniques in fluid flows by Tropea (2011). To accurately size the bubbles, high magnification is required (field-of-view $\sim$ 1 mm^2), resulting in the need for an impractically large number of images to observe enough detections for a converged measurement. To circumvent this issue interferometric techniques possessing a larger detection volume have been employed.

Early use of interferometric sizing techniques was reported for application in particle spray measurements, particularly in fuels (König et al., 1986; Skippon and Tagaki, 1996; Mounaïm-Rousselle and Pajot, 1999), and its development stemmed from the Global Phase-Doppler technique (Albrecht et al., 2013). Various implementations of the method have been developed, but the fundamental operating principle is the same, monochromatic light illuminates a bubble (or particle) and the scattered light produces an interference pattern. Information from the interference pattern is used to determine the bubble/particle size. Based on the slight differences between implementations, the method has been given different names: Interferometric Laser Imaging, Mie Scattering Imaging, Global Phase Doppler, Inteferometric Laser Imaging for Droplet Sizing, Interferometric Particle Imaging, and Interferometric Mie Imaging. We adopt the nomenclature of Graßmann and Peters (2004) and label the method Mie Scattering Imaging (MSI). This name reflects the technique's roots in the mathematically rigorous scattering of a plane wave by a sphere, postulated by Lorentz-Mie Theory (Bohren and Huffman, 2008).

Numerous extensions to MSI technique have been proposed in the published literature. A cylindrical lens can be incorporated to compress interference patterns in one dimension on imaging sensors (Maeda et al., 2000; Kobayashi et al., 2000; Qieni et al., 2014). This reduces overlap of the fringes when multiple bubbles (or particles) are present and thus increases the concentration limit of the technique. The use of laser light also lends itself to simultaneous particle-image velocimetry and size measurement (Kawaguchi and Maeda, 2005). Novel methods have also been proposed to measure the 3D location of droplets in addition to the diameter through an optical arrangement that shears the interference pattern as the distance from the sensing plane increases (Brunel and Shen, 2013; Shen et al., 2013). Alternatively the size of the interference disc can also be used to estimate the out-of-plane location (Tropea, 2011).

Comparative experimental measurements of nuclei size distributions using MSI and various other nuclei measurement techniques have shown large discrepancies in the results (Quérel et al., 2010; Ebert et al., 2015; Boucheron et al., 2018; Birvalski and van Rijsbergen, 2018). To minimize the uncertainty and errors in the results obtained using MSI, Lacagnina et al. (2011) suggest that a systematic calibration of the method has to be performed. The most detailed treatment of sensitivity and uncertainty analysis has been reported by Dehaeck and van Beeck (2007). They identify measurement of the lens and sensor plane location as a potential source of error and uncertainty in calibration experiments. Custom lenses or specialist optics knowledge can provide the required precision (Mées et al., 2010), but for a standard multi-element lens and camera such data may not be accessible. Dehaeck and van Beeck (2007) examined multiple methods for calibration and full experimental calibration is identified as very accurate. A calibration experiment of a similar nature was conducted by Russell et al. (2020b). Individual microbubbles from a mono-disperse bubble generator were simultaneously recorded using shadowgraphy and MSI. A calibration procedure was demonstrated and using this method measurements with the two techniques deviated by less than ±0.5µm for bubbles 40-150µm in diameter. In addition, the calibration method for the size dependent measurement volume proposed by Ebert (2015) was extended. The method of Ebert (2015) was developed from Laser-Doppler Velocimetry theory (Albrecht et al., 2013) and assumes a Gaussian beam profile (Ebert et al., 2016), whereas the procedure of Russell et al. (2020b) avoids this assumption through measuring the beam profile directly. The efficacy of the method was demonstrated using the location of the bubbles in the beam measured from the shadowgraphy data. The details of this correction are critical, as just like shadowgraphy, the measurement volume of MSI changes with bubble size (Mées et al., 2010). Due to its sensitivity, volumetric correction errors may then account for some of the discrepancies between the microbubble measurement techniques reported in hydrodynamic test facilities (Lacagnina et al., 2011; Mées et al., 2010; Ebert et al., 2015).

The ability to measure and precisely control nuclei populations in water tunnels enables rigorous comparison of results from different facilities (Lindgren, 1966). Although the origin and quantity of nuclei may stem from a variety of sources, the natural nuclei population present in each facility progresses towards equilibrium with the available dissolved gas content of the surrounding fluid. Often nuclei control in facilities is achieved solely through dissolution of these populations by degassing the water (Liu et al., 1993; Etter et al., 2005; Weitendorf et al., 1987). However, natural populations may still be partly comprised of nuclei biological and particulate in nature, the cavitation susceptibility of which cannot be measured optically. To produce populations of the desired concentration and strength that can be measured optically, the AMC water tunnel uses filtered, degassed water, to which artificial microbubble nuclei are injected using a seeding system (Brandner et al., 2006). This tunnel architecture emulates the French Grand Tunnel Hydrodynamique (GTH) (Lecoffre et al., 1987). This facility uses cavitating micro-jets of supersaturated water to generate the artificial microbubble nuclei. These nuclei generators were characterised outside the water tunnel and typically produce a poly-disperse plume of bubbles 2-200μm in diameter (Giosio et al., 2016). However, their response to changing tunnel operating conditions has not yet been fully characterised. The scope of the present work is to present the application of the refined MSI technique for nuclei measurement in hydrodynamic test facilities and analyse the effect of variable operating conditions to better understand the range of nuclei populations that can be tested for in the facility.

A short summary of the equations used for bubble sizing and antecedent Lorentz-Mie theory are presented in Sect. 5.3, including deliberation on the choice of measurement parameters. Experimental method and equipment, including an outline of data processing technique, are found in Sect. 5.4. Calibration methods are also presented in Sect. 5.4.2. This includes an improvement to the *in-situ* calibration of the measurement volume that extends the dynamic range of the technique. The measurement technique is used to characterise the range of microbubble sizes and concentrations that can be produced in the test section by the nuclei seeding system (Sect. 5.5). The modification of generated populations with changing tunnel conditions is shown to be complex, as the microbubble population generated upstream are affected by the change in pressure through the contraction, and dissolution that occurs due to bubble residence time. To explore this process a quasi-steady model of bubble dynamics with dissolution is used to simulate the modulation of the injected population (Sect. 5.6). Results of the simulation are then related to the observed population as tunnel conditions vary, and the implications for tunnel operation explored. Conclusions are presented in Sect. 5.7.

5.3 Mie Scattering Imaging

Theory and experiments have shown that a linear mapping can be constructed between the size of a microbubble ($\sim 1 - 100$ μm) and the number of interference fringes of light it scatters across a narrow angular domain (Mées et al., 2010; Boucheron et al., 2018).

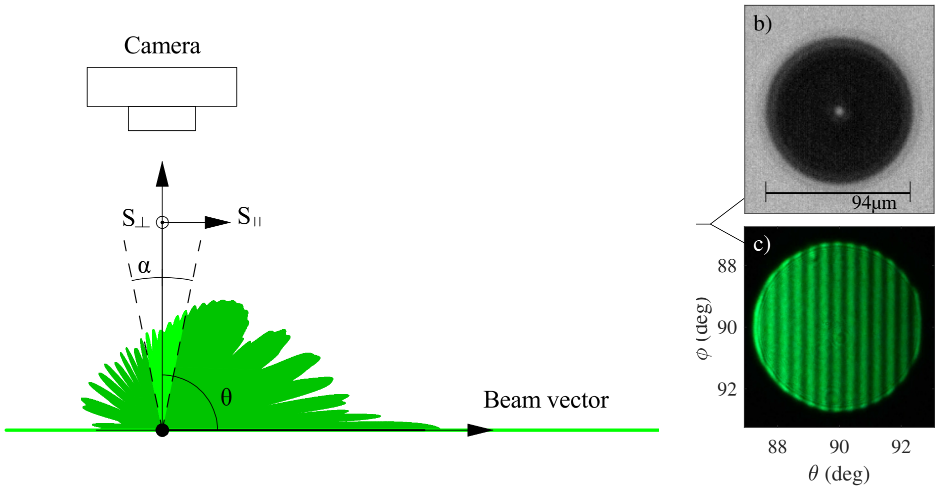

Figure 5.2: a) A schematic of the MSI measurement technique. b) A shadowgraphy image of a 94 µm bubble. c) The interference pattern produced by the same bubble as in b).

This can be expressed by equation

$$d = \frac{KN}{\alpha} \qquad \frac{[\mu\text{m}\ ^\circ]\ []}{[^\circ]}, \tag{5.1}$$

where d is the bubble diameter in microns, N the number of fringe wavelengths across the angle α, and K is a proportionality constant. K depends primarily on the wavelength of light used to illuminate the bubble and the scattering angle θ_s, which is defined as the angle between the camera, the bubble and the direction in which the light is propagating (Fig. 5.2 a). An example of an interference pattern resulting from Mie scattering of a 94 µm bubble (Russell et al., 2019) is presented in Fig. 5.2c, along with the calibrated shadowgraphy image of the same bubble captured simultaneously (Fig 5.2b). In order to create an image disc containing the frequency information, MSI images must be taken off-focus, as otherwise the scattered light would focus back to a point. In experiments by Russell et al. (2020b), equation 5.1 was recast to map the wavelength of interference fringes in pixels, to the diameter of the bubble, by introducing a second constant A. Its value encapsulates the angle a single pixel represents in an interference pattern. By converting N/α to a wavelength (λ_{deg}), and substituting A, equation (5.1) becomes,

$$d = \frac{KN}{\alpha} \qquad \frac{[\mu\text{m}\ ^\circ]\ []}{[^\circ]} \tag{5.2a}$$

$$= \frac{K}{\lambda_{deg}} \qquad \frac{[\mu\text{m}\ ^\circ]}{[^\circ]} \tag{5.2b}$$

$$= \frac{K}{A\ \lambda_{px}} \qquad \frac{[\mu\text{m}\ ^\circ]}{[^\circ\ \text{px}^{-1}]\ [\text{px}]}. \tag{5.2c}$$

Light scattered by a bubble can be decomposed into two components. One parallel to the scattering plane, i.e. the plane containing the camera, bubble, and direction of propagation ($S_{||}$), and the other that is normal to the scattering plane ($S_{\perp}$). The intensity of each component is modulated by the angle between the polarisation of the laser and the scattering plane, called the polarisation angle ψ_{s}. Despite being overall less intense the $S_{||}$ component produces a more uniform fringe spacing making it preferred. For these experiments a scattering angle $\theta_{\mathrm{s}} = 90°$, with a polarisation angle $\psi_{\mathrm{s}} = 90°$ was used. A polarising filter on the lens admits only $S_{||}$ for measurement. Further discussion on the selection of these parameters is presented in Russell et al. (2020b).

Calibration of the value for K can be determined by simulating intensity curves from theory and measuring the fringe wavelength for a range of bubble sizes. For 532 nm light where $\theta_{\mathrm{s}} = 90°$, K has been measured to be 39.8 µm·deg^{-1}. Experimental calibrations for the setup-dependent value A, and the size dependent measurement volume, are discussed in the following section.

5.4 Experimental Setup

Experiments were conducted in the Cavitation Research Laboratory (CRL) variable pressure water tunnel at the University of Tasmania. The test section is 0.6 m square by 2.6 m and operates with velocities of 2 to 13m/s and pressures of 4 to 400 kPa. To manage turbulence, upstream of the test section is a plenum containing a 6mm plastic honeycomb. The homogenised flow then passes through a contraction section leading to the test section entrance to constrict any remaining turbulence. The test section velocity is measured from the calibrated contraction differential pressure. Depending on the value, either high or low range Siemens Sitrans-p differential pressure transducers models 7MF4433-1DA02-2AB1-Z (pressure range 0-25 kPa) and 7MF4433-1FA02-2AB1-2AB1-Z (pressure range 0-160 kPa) are used, with estimated precision of the velocity measurements of 0.007 and 0.018 m/s respectively. The test section velocity has been measured to be spatially uniform to within 0.5%, and has temporal variations of less then 0.2%, with the free stream turbulence intensity of 0.5%. Further details of the facility are given in (Brandner et al., 2006, 2007; Doolan et al., 2013).

Nuclei injection was realized using an array of micro-bubble generators positioned in the plenum upstream of the tunnel honeycomb and contraction (Fig. 5.4). The generators operating principle is based on rapid expansion of supersaturated water in a confined turbulent jet. A schematic of a single generator is presented in figure 5.3. Supersaturated water is expanded through a ∅ 0.5 mm by 0.3 mm long orifice into a ∅ 1.2 mm by 200 mm long hypodermic tube, where micro-bubbles form in shear layer cavities. The generators produce a poly-disperse plume of micro-bubbles 2-200 µm in diameter (Giosio et al., 2016; Brandner et al., 2010b). The supersaturated water is created using a separate

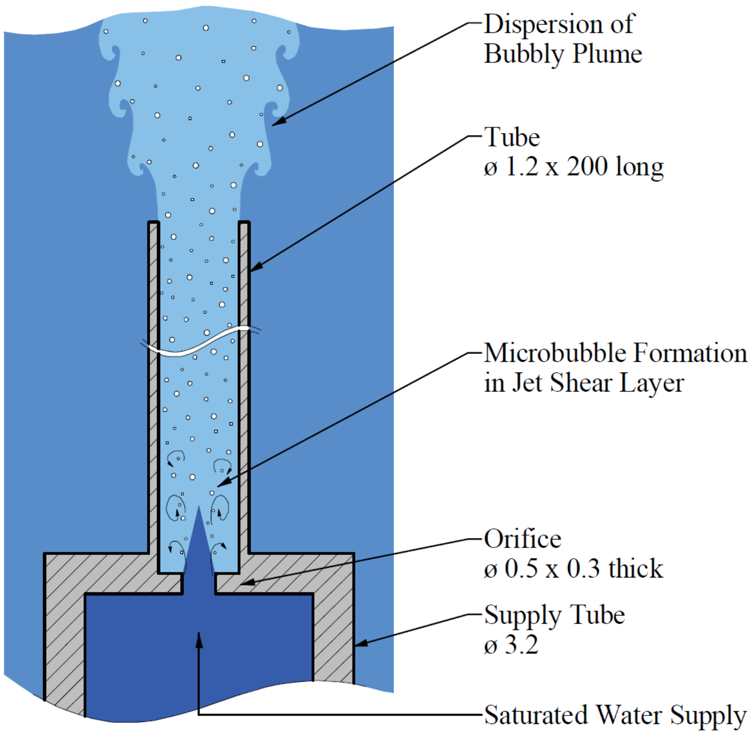

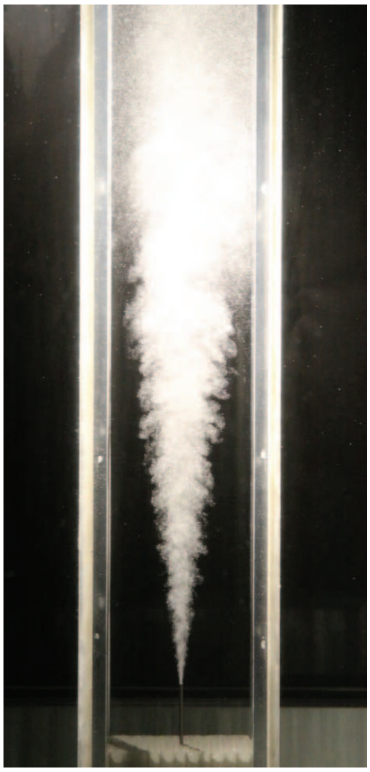

Figure 5.3: a) Schematic of one nuclei generator. b) A photograph of a single generator being operated outside the tunnel in co-flow. Both images are reproduced with author permission from an experiment to characterise the bubble population produced at the generator outlet (Brandner et al., 2010b).

recirculating pressure vessel (saturation vessel) designed to facilitate the dissolution of gas into the liquid at high pressures and is capable of maintaining pressures of 100-20000 kPa.

The microbubble population generated is a function of the absolute and differential values of the saturation vessel (p_s) and tunnel plenum (p_p) pressures, where $\Delta p = p_s - p_p$. From which the dimensionless parameters including the Reynolds, Weber and cavitation numbers, and the saturation pressure ratio of the supply and tunnel water, may be formed. The Reynolds and Weber numbers are proportional to $\sqrt{\Delta p}$ and Δp respectively. The cavitation number and saturation pressure ratio may be defined as $p_p/\Delta p$ and p_s/p_p respectively. The first two parameters are relatively large and don't change appreciably for the range of pressures involved. The last two parameters arguably have the greatest effect on the generated population and hence ultimately the tunnel test section population. The cavitation number and saturation pressure ratio control the cavity and available gas volumes respectively. If it is assumed that the Reynolds and Weber numbers don't affect the flow then a series of pressure combinations can be set for which the cavitation number and saturation pressure ratio remain constant. However for each of these combinations Δp will change which controls the flow rate and hence the bubble production rate.

The array of generators can be configured to seed different areas of the tunnel cross section. Generators can be affixed in an 80 mm triangular grid pattern across the plenum. For the present study, three rows of 10 generators were used to seed a 300 mm high by 100 mm wide, nominally rectangular, area in the top half of the test section.

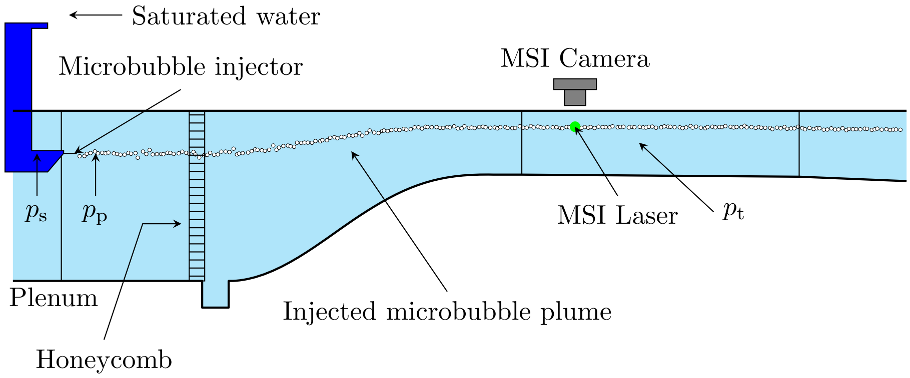

Figure 5.4: A schematic of the tunnel seeding arrangement and measurement setup. Bubbles injected upstream of the honeycomb are advected into the test section. A horizontal laser beam across the test section is used to measure bubbles with MSI using a 90° scattering angle.

The MSI measurements were captured using a 48MP IO Industries Flare 48M30 CX high-speed CMOS camera equipped with a Sigma 180 mm 1:2.8 APO Macro DG-HSM lens, located above the test section. A Promaster HGX Prime 86 mm polarizing filter was attached to the lens. Bubbles were illuminated using an Ekspla NL204-SH TEM_{00} laser emitting 532 nm light with pulse frequency of up to 1kHz and the energy of 2 mJ per pulse. The beam was collimated using a plano-convex LA1978-A-ML coated lens with a focal length of 750 mm, and it was then passed through a Thorlabs BSF10-A 1" UVFS 10% Beam Sampler before being directed into the tunnel by a Thorlabs NB1-K12 1" Nd:YAG mirror. A schematic of the optical arrangement is shown in Fig. 5.5. Mirror M1 was mounted to a Melles Griot microstage to enable precise positioning and movement of the laser beam in the tunnel. The beam entered the tunnel test section horizontally through an 80 mm thick glass port, 145 mm below the test section ceiling. An angle of 87° to the port was chosen to prevent any reflected and refracted rays from overlapping the measurement beam. Accordingly, the camera was rotated so that the horizontal axis was parallel to the direction of beam propagation. The camera was set with the sensor-plane-normal perpendicular to the beam so that the measurement scattering angle was $\theta_s = 90°$ (Fig. 5.2a). The Ekspla laser was polarised horizontally giving an MSI polarisation angle $\psi_s = 90°$.

5.4.1 Processing

Images were analysed using a custom Matlab script. Each interference pattern was reduced to a representative one-dimensional 'pixel series' of the same width as the original pattern. To generate these series, an iterative algorithm was used to extract the

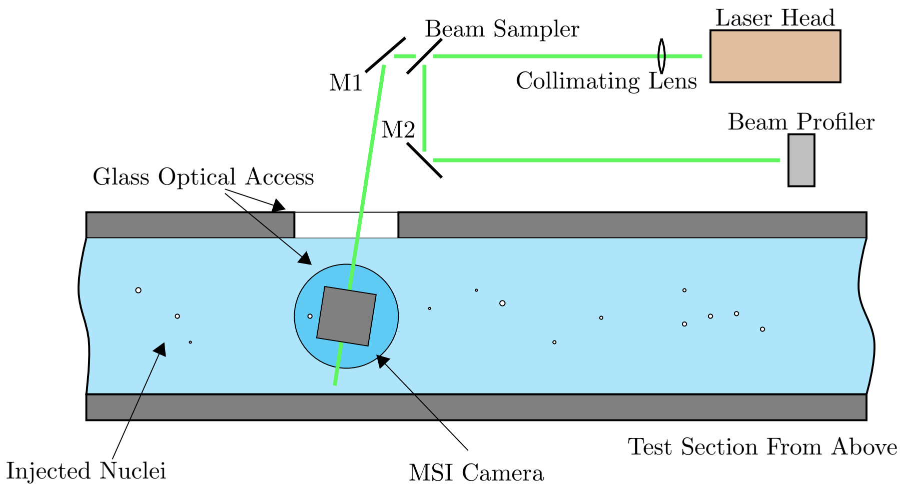

Figure 5.5: An overview of the optical setup used to calibrate and capture the MSI images.

brightest interference pattern from an image, masking out the circular area afterwards. The masked image was then re-processed, and the processing continued until the median of the intensity series extracted in the current step was lower than a specified intensity threshold. Steps to locate and extract pixel series were,

1. Cross correlate a down-sampled image with a down-sampled template.
2. Locate correlation maximum.
3. Refine location by cross correlation in a limited domain with the full template.
4. Extract circular domain to generate an intensity series.
5. Sum each column of the extracted region and divide by the number of pixels to generate the 'pixel series'.
6. Mask out the region of the image and re-process the masked image.
7. If the median intensity of the pixel series is too weak, discard the last data and stop processing the image.
8. Filter and record all valid bubble locations and associated pixel series.

The last step filtered out bubbles that were too close together, or too close to the edge of an image, for the frequency detection algorithm to accurately measure the bubble size. In the case of two bubbles close together, both were discarded. This would cause an underestimate in the total bubble concentration if many bubbles overlapped, however, in present data such occurrence was rare, and it was observed no more than twice in 1000 detections. Once an image had been converted into a set of pixel series, auto-correlation was used to extract interference wavelengths. Each auto-correlation was refined by fitting a quadratic curve to the 7 points around the first maximum. The quadratic curve was then re-sampled with 1000 points to find the dominant wavelength in the interference pattern. The dominant wavelength was converted to bubble diameter through equation 5.2. The intensity of an interference pattern was defined as the 95th percentile of the extracted pixel series. This, along with the location of the bubble in the beam, was used to calculate the measurement volume of the technique for the optical setup described above.

5.4.2 Calibrations

To calibrate the magnification factor of images in the laser plane, mirror M1 (figure 4) was traversed in the stream-wise direction. The beam was moved 5 mm upstream and downstream of the initial position with the camera remaining fixed. Long exposure images capturing a large number of bubbles passing through the measurement volume were recorded. From these images, the average location of the centre of the interference pattern was found, which represented the location of the centre of the laser beam for each mirror position. By dividing the pixel shift in the image by the set mirror movement, the magnification factor expressed in px/mm was determined.

Calibration of the angular wavelength constant A was performed using the method described by Russell et al. (2020b). A 0.5 mm thick masking plate with two holes was placed in between the lens and the beam at the glass-water interface. The holes were 6 mm in diameter, with the centers 14 mm apart. The plate was used to mask the interference pattern and produce a diffraction pattern from which the distance between the hole centers in pixels (D_{px}) could be measured. An example of the resulting image is shown in Fig. 5.6a. With the distance between the masking plate and the beam known, the angular constant A can be calculated from basic trigonometry as

$$A = \frac{2 \cdot \tan^{-1}\left(\frac{\text{Hole Distance}}{2 \cdot \text{Beam Distance}}\right)}{D_{px}}. \tag{5.3}$$

A sample of 60 bubble instances was used to measure A, and to estimate the uncertainty. From Fig. 5.6b, $D_{\text{px}} = 260$ px and has an estimated uncertainty of 10 pixels. D_{px} does not change appreciably across the measurement beam length. A was calculated to be $A = 0.0123\ \text{px} \cdot \text{deg}^{-1}$. Linearised uncertainty in d has been tabulated for a small and large bubble (Table 1), and overall uncertainty from this calibration remains a constant 3.85% from this source.

The effective measurement volume for MSI is dependent on bubble size and characteristics of the optical setup. The scattered light intensity of a bubble is nominally dependent on the square of the diameter. Therefore, for a Gaussian beam profile the scattered light intensity will depend on the bubble size and its location in the beam profile. Consequently,

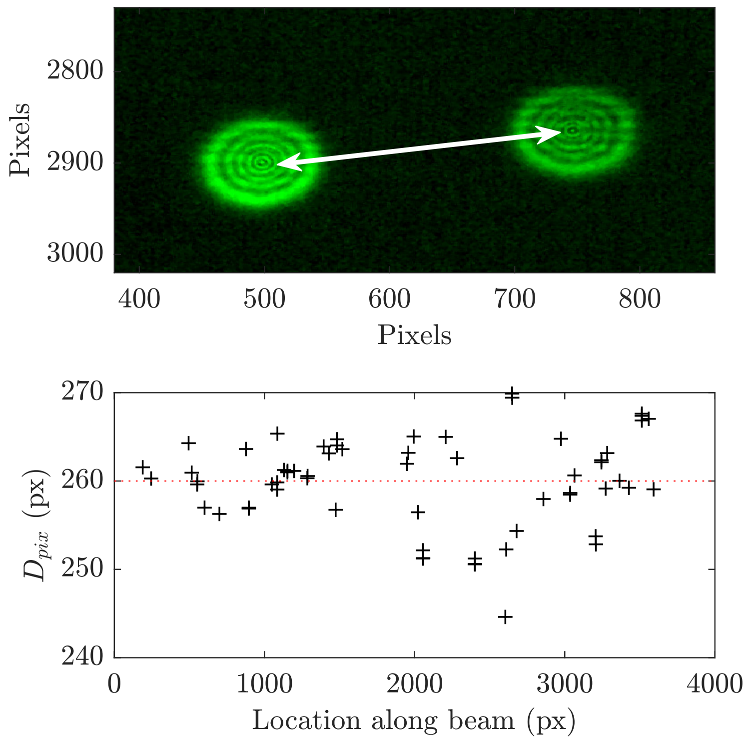

Figure 5.6: a) An example of the two hole calibration pattern image obtained using a masking plate, from which D_{pix} is measured. b) A scatter of D_{pix} values across 60 bubble instances, with average value denoted with a dashed line.

Table 5.1: Tabulated values of the calculated diameter uncertainty due to a 10 pixel variation in A for a small and a large bubble.

Diameter (µm)	Uncertainty (µm)	Uncertainty %
20	± 0.77	$\pm 3.85\%$
150	± 5.77	$\pm 3.85\%$

larger bubbles are measured across a wider area as less incoming light will be required to produce an interference pattern that is above the lower limit of camera sensitivity. However, a large bubble may also saturate the camera sensor so that the interference pattern cannot be discerned, so a portion at the centre of the beam may have to be excluded. Using this approach, the dynamic range of the technique is optimised at the expense of more complex measurement volume calculation.

To detail the volume correction calculation a camera-beam based coordinate system was introduced: the x-axis was placed along the beam center-line and the y-axis across one dimension of the beam profile, where both x and y were parallel to the focal plane of the camera. The z axis was normal to the focal plane of the camera.

As a bubble moves in the $x - y$ plane of the beam the centroid of the interference pattern shifts in the MSI image. Pattern intensity depends on a bubble's y and z location in the beam profile. By plotting y position against measured intensity for a narrow size range, an estimate of the size-dependent maximum intensity at each y location with size was obtained (Fig. 5.7). For these data, bubbles were grouped into $d = \pm 2.5$ µm size bins and then sub-grouped into $y = \pm 0.5$ µm location bins. The 95$^{\text{th}}$ percentile of a single diameter/location bin was used to estimate the maximum intensity $I_{\text{max}}(d, y)$ and is plotted with a red line in Fig. 5.7.

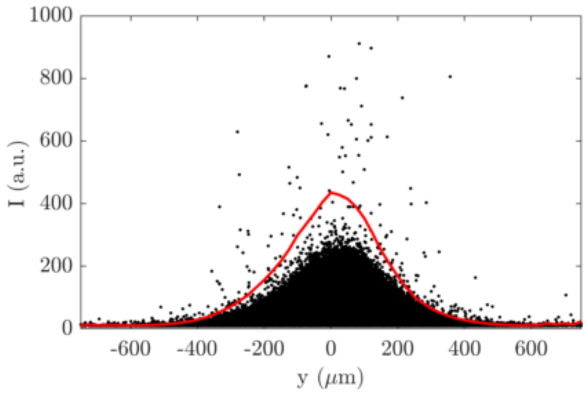

Figure 5.7: A scatter of y-location and intensity of all bubble detections in 20-25 µm range ($\approx$ 30000 detections). A red line representing the 95th percentile calculated for 1 µm bins is plotted. This curve used to estimate the maximum intensity $I_{\text{max}}(d, y)$.

As discussed by Ebert (2015), it is very unlikely that a bubble measurement is observed in the exact centre of the beam for each size and y location, but with enough data the described process provides a reasonable estimate. By using all the data from an experimental campaign a large number of detections can be compiled. In the present experiment 2.46 million bubbles were detected. A minimum intensity threshold ($I_{min} = 50$) was applied to establish the maximum radius for effective measurement for each bubble size. A maximum intensity threshold $I_{max} = 400$ was also applied to ensure that bubble patterns too bright to be accurately sized were removed. This resulted with an annular area of effective measurement for some bubbles. In Fig. 5.8a the maximum intensity curve for two bubble size ranges, 20-25 µm and 80-85 µm, is plotted across the beam y-position. By plotting the intensity with colour, and stacking the intensity curves for each bubble size range horizontally, a contour plot showing the measurement area limits can be assembled, as shown in (Fig. 5.8b). Multiplying the effective area by the beam length measured by the MSI camera gives the effective measurement volume, this is plotted against diameter in Fig. 5.8c. The comparatively low number of detections for bubbles $d > 150$ µm introduces scatter in the estimated measurement volume. A smoothing spline was used to calculate the final size dependent volume.

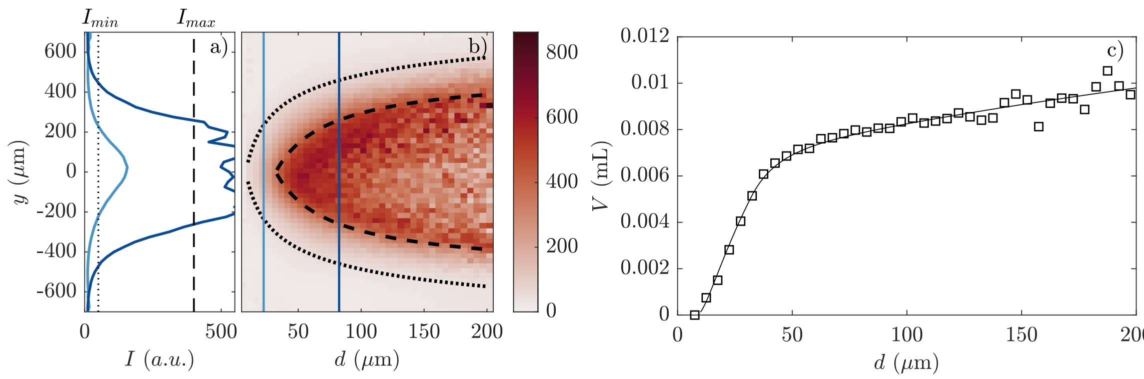

Figure 5.8: a) The maximum intensity of interference patterns intensity for two bubble size ranges (d =20–25 µm and 80–85 µm) plotted against the vertical location of the bubble in the beam. b) A colour map of the interference intensity mapped for a range of locations and measured diameters. The dotted contour is the minimum intensity threshold and the dashed line the maximum intensity threshold. The blue lines represent the data presented in a). c) The dependence of effective measurement volume on bubble size.

5.4.3 Convergence of concentrations and histograms

A study was performed to determine the number of bubble detections required to obtain a converged statistic for bubble size distribution. For this purpose a sample of 40000 detections was recorded. To calculate the total bubble concentration, the detection volume for each bubble was determined by interpolation of the fitted curve in Fig. 5.8c. The total bubble concentration was then calculated by

$$C = \left(\sum_{i=1}^{N_{bubbles}} \frac{1}{v_i} \right) / N_{images}, \tag{5.4}$$

where v_i is the size dependent measurement volume for the i^{th} bubble detection. To view these data as a distribution of bubble sizes, the nuclei number density distribution function $\frac{dC}{dd}$, referred to here as the size distribution, can be calculated (Brennen, 2014). Bubble counts corrected by measurement volume are grouped into a histogram with logarithmic bin width. By dividing bin counts by the bin width, concentrations are expressed as $\frac{dC}{dd}$ at the bin centers. Integration between any two points on this curve estimates the concentration of bubbles within the sub-range. The total concentration was estimated using all 40000 detections. Total concentration was then iteratively calculated including one extra detection each time. Total concentration with each added bubble is plotted in Fig. 5.9a and the percent difference from the final estimate is plotted in Fig. 5.9b. The total concentration converges quickly so that a crude estimate to within 10% of the final concentration can be obtained with only 100 detections. To remain within 1% of the final estimated concentration 10000 detections are required. A similar number is required for convergence of the bubble size histogram with a bin size of 2 µm. This is presented visually in Fig. 5.10. A histogram was calculated with the addition of each bubble.

Each histogram was normalised by its highest bin count. The normalised histogram was converted to colour and stacked horizontally. The distribution shape remained similar for $N > 10000$.

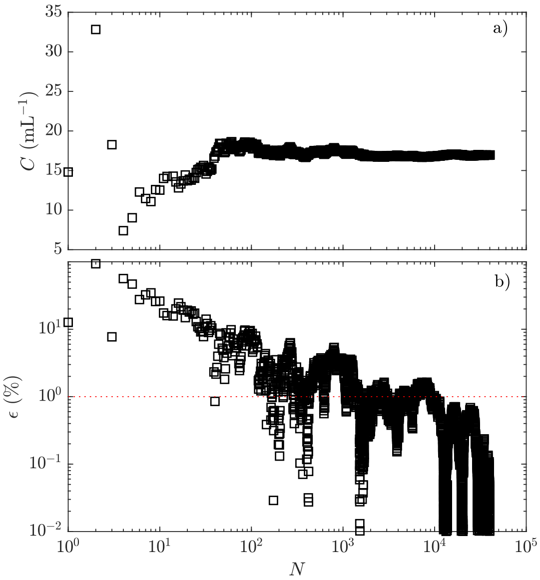

Figure 5.9: a) Bubble total concentration (C) as a function of number of bubbles counted (N). b) Percent difference from the final concentration for large N. The difference is less than 1% which has been marked in red for $N > 10^4$.

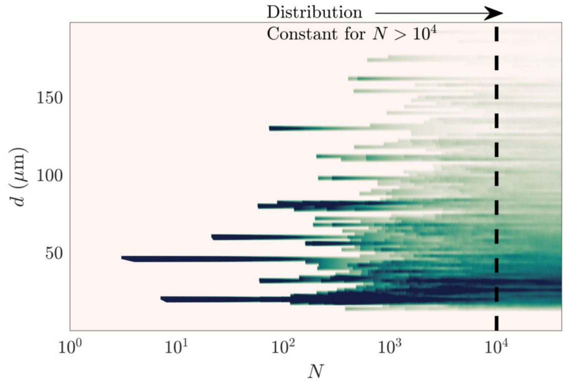

Figure 5.10: Normalised histograms of the bubble distribution are oriented vertically and are presented as colour for an increasing number of bubble counts. The bin width is 2 µm. The population distribution converges for $N > 10^4$ detected bubbles for the presented bubble concentration.

An important consideration for implementation of MSI technique during the hydrodynamic facility operation is the time required to obtain the nuclei size distribution result. The time required to acquire and process images using the full camera sensor, as it was done for calibration and convergence analysis , while reasonable, still proved to be somewhat prohibitive during testing work-flow. To facilitate faster result turnaround, the images obtained for the analysis of the effect of tunnel operating conditions on the nuclei population were down sampled by the ratio of 2 in the direction of the fringe pattern. Additionally, the images were acquired over a reduced sensor area covering only the horizontal region illuminated by the laser beam. The camera's native resolution is 7920×6004, these steps led to a measurement resolution of 4096×512 pixels. After applying these modifications the time required to acquire a set of images needed for the converged result was in order of a few minutes, and therefore, the described MSI technique can be considered as a near real-time measurement. An example image captured by the measurement system is presented in Fig. 5.11.

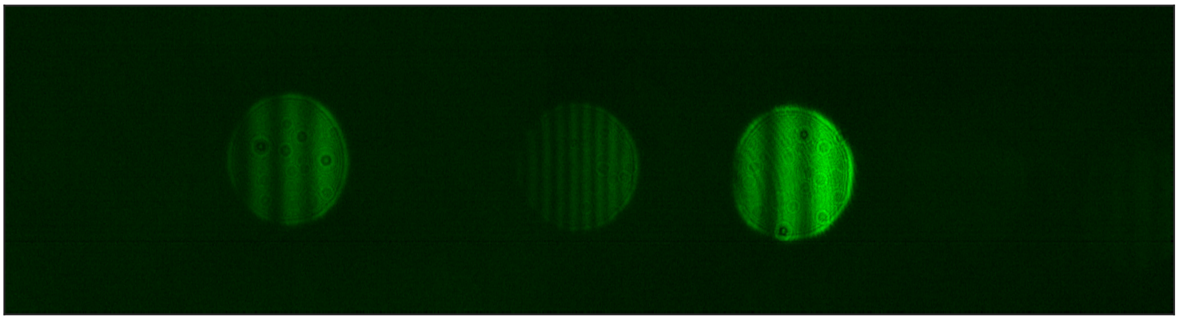

Figure 5.11: An example image captured with MSI measurement system after a logarithmic intensity filter has been applied to enhance visibility of the interference patterns is presented. Bubble diameters observed in the image from left to right are 16 µm, 39 µm, and 14.5 µm respectively.

5.5 Tunnel Nuclei Results

5.5.1 Generator parameters

For constant tunnel operating conditions, the test-section nuclei content can be altered by varying nuclei generator parameters, namely the generator driving pressure Δp_{gen} and cavitation number σ_{gen}. To assess the influence of each of these parameters, bubble populations in the test-section were measured for a tunnel velocity of 7 m/s, while Δp_{gen} and σ_{gen} were varied independently of each other. Both generator parameters are coupled to tunnel operating conditions through the pressure in the plenum (p_p) where,

$$\Delta p_{gen} = p_s - p_p, \tag{5.5}$$

and

$$\sigma_{gen} = \frac{p_p - p_v}{p_s - p_p} = \frac{p_p - p_v}{\Delta p_{gen}}. \tag{5.6}$$

Therefore the tunnel pressure (p_t) was varied in conjunction with the saturation vessel pressure (p_s) to keep one generator parameter fixed while the other varied. Observations are made with the knowledge that tunnel pressure will influence dissolution processes. In Fig. 5.12a the total concentration of bubbles 10-200 µm in size are plotted for fixed $\Delta p_{gen} = 400$ kPa and varying σ_{gen}. Bubble concentration remains similar for $\sigma_{gen} \leq 0.41$, but decrease rapidly as σ_{gen} is further increased such that very few if any bubbles are measured for $\sigma_{gen} \geqslant 0.55$. Bubble size distributions for the data points shown in Fig. 5.12a are plotted in Fig. 5.12b. The distribution shape remains similar for low σ_{gen}, however a roll-off in the number of large bubbles produced can be observed. This roll-off shifts towards the smaller sizes as σ_{gen} increases. It is hypothesised that this trend would continue as σ_{gen} increases further, however this cannot be supported by experimental data as the roll-off moves below the minimum measured size. Irrespective of this, for $\sigma_{gen} > 0.55$ only a low concentration of very small bubbles remains.

In Fig. 5.13a the total bubble concentration is plotted for a constant $\sigma_{gen} = 0.25$, while the Δp_{gen} was varied. An increase can be observed in the total concentration with increasing Δp_{gen} , however C plateaus as Δp_{gen} increases above approximately 600 kPa. In contrast to the results for constant driving pressure the overall distribution shape remained identical Fig. 5.13b. The increase in concentration is mostly associated with the population of smaller bubbles, but the distributions suggest a more global increase in all bubble sizes is produced. This behaviour is consistent with the premise that for constant σ_{gen} the bubble production mechanism remains the same, but due to higher flow-rates through the generator the number of bubbles produced will increase. In both Fig. 5.12 and Fig. 5.13 the low number of detections introduces scatter into distributions for large bubble sizes. For the data in Fig. 5.12 and Fig. 5.13, the tunnel pressure is labelled with the additional horizontal axis above the graph. Note, that due to the contraction, at 7 m/s tunnel velocity, the pressure in the plenum will be $p_p = p_t + 35$ kPa.

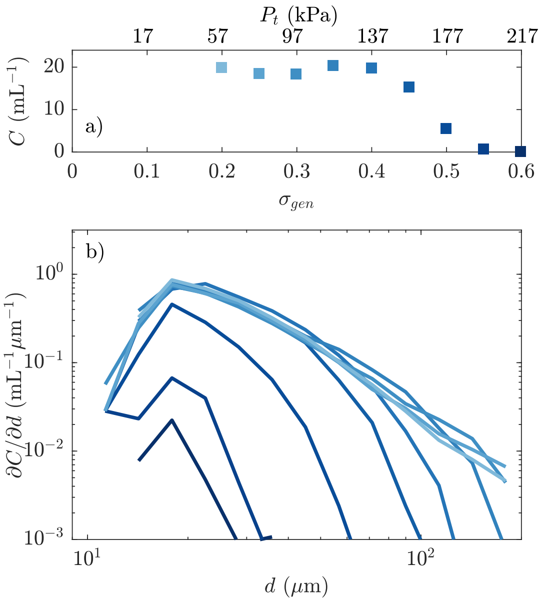

Figure 5.12: a) Total bubble concentration plotted against σ_{inj}. The tunnel pressure was varied in conjunction with p_s to maintain constant driving pressure, $\Delta p_{inj} = 400$ kPa, with a constant tunnel velocity $U_t = 7$ m/s. b) A plot of size distributions for the examined range of σ_{inj}. For $U_t = 7$ m/s, pressure drop through the contraction leads to $p_p = p_t + 35$ kPa.

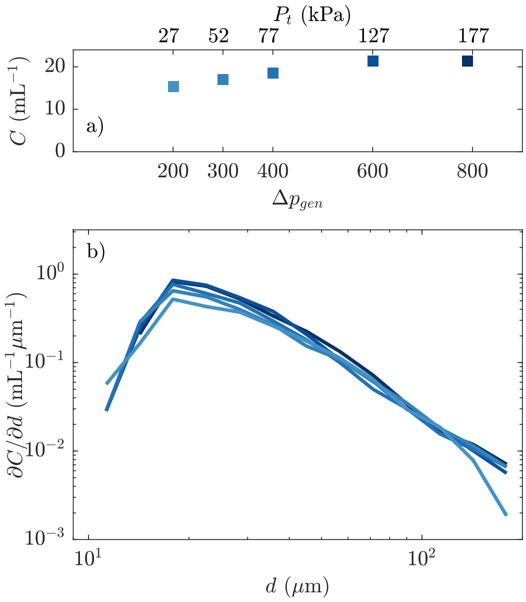

Figure 5.13: a) Total bubble concentration plotted against Δp_{gen}. The tunnel pressure was varied in conjunction with p_s to maintain constant $\sigma_{gen} = 0.25$, with a constant tunnel velocity $U_t = 7$ m/s. b) A plot of size distributions for the examined range of Δp_{inj}. For $U_t = 7$ m/s, pressure drop through the contraction leads to $p_p = p_t + 35$ kPa.

The measurements of bubble population for varying σ_{gen} were performed for a range of driving pressures 100 kPa $\leq \Delta p_{gen} \leq$ 800 kPa, for tunnel velocity of 7 m/s. Resulting total bubble concentrations and size distributions are presented in Fig. 5.13. From the plot of total concentration (Fig. 5.14a), it can be seen that the critical cavitation number at which the concentration begins to reduce, increases with increasing driving pressure. In addition, the maximum concentration increases with increasing driving pressure. The distribution trends remain similar when comparing between driving pressures. It is observed that as the total bubble concentration increases the size distribution approaches a power law like behaviour. This power law distribution may be linked to the turbulent processes in the generator outlet, rather than the result of equilibrium processes on injected bubbles as they are advected through the plenum and contraction section. This is also true of distribution roll-off as dissolution processes in the tunnel are more likely to impact smaller bubbles due their increased surface area to volume ratio. The distributions move closer to the annotated power law across Fig. 5.14b-g as the driving pressure increases. This is the manifestation of the increase in total concentration with increasing driving pressure.

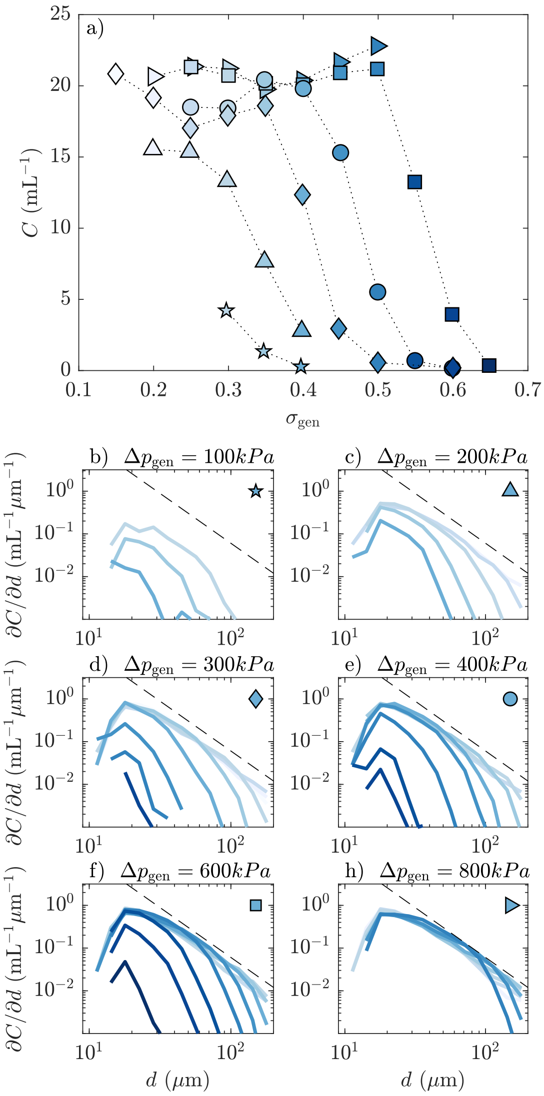

Figure 5.14: a) Total concentrations plotted against σ_{gen} for various $\Delta_{P_{gen}}$. Each subplot (b-g) represents bubble size distributions for different σ_{gen} for a particular value of $\Delta_{p_{gen}}$. σ_{gen} is represented by the colour in each subplot that corresponds to the colours in a). The plots are for a fixed U_t = 7 m/s, while the dissolved oxygen content was in range DO_2 = 26–34% of saturated concentration at atmospheric pressure. As a visual aid a curve denoting an approximate power law has been annotated on distribution plots.

5.5.2 Dissolved Oxygen Content

As previously mentioned the tunnel is designed to operate with a dissolved oxygen content (DO_2) of 30% of saturation concentration at atmospheric pressure, to ensure that all injected microbubbles dissolve and do not complete the tunnel circuit. Low DO_2 content promotes dissolution of the generated microbubble populations between the point of injection and measurement location in the tunnel test-section. To assess the extent of the dissolution related to the low DO_2 content. Nuclei populations were measured with DO_2 varied between 2 and 10 ppm for constant test section parameters (p_t = 77 kPa, U_t = 7 m/s, σ_{gen} = 0.25, and Δp_{gen} = 400 kPa). The measured concentration and distribution of bubbles are plotted in Fig. 5.15. A non-linear increase in total bubble concentration is observed with increasing DO_2, which is predominantly associated with an increase in the number of smaller bubbles. An approximate power law was again observed, the exponent of which increased with increasing DO_2 content.

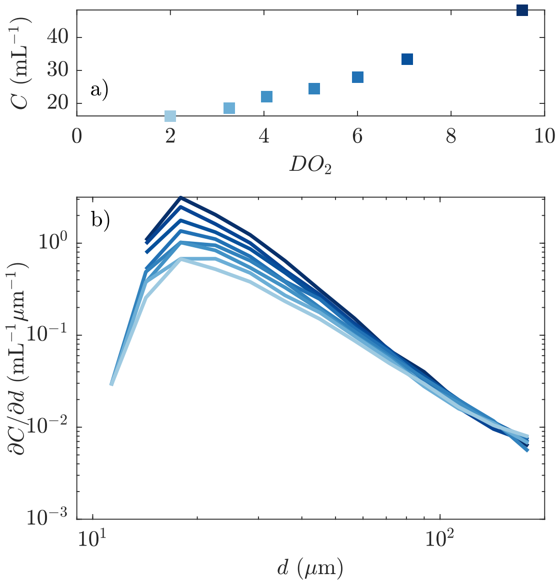

Figure 5.15: a) Total bubble concentration (C) as a function of the dissolved gas level in the test section, for constant injector (σ_{gen} = 0.25 and $\Delta_{p_{gen}}$ = 400 kPa) and tunnel parameters (p_t = 77 kPa and U_t = 7 m/s). Injector parameters are σ_{gen} = 0.25 and Δp_{gen} = 400 kPa. Test section parameters are p_t = 77 kPa and U_t = 7 m/s. The corresponding size distributions are plotted in b).

5.5.3 Tunnel operating parameters

The influence of the tunnel parameters on the injected bubble population is difficult to assess, as generator parameters cannot be kept fixed while independently varying the tunnel conditions. To gain some insights, one generator parameter was fixed, while the variation of the other was coupled to the matrix of prescribed tunnel conditions. Seven tunnel pressures, in the range between 20 kPa $\leq P_{\text{t}} \leq$ 200 kPa, and five tunnel velocities

, in the range between 3 m/s $\leq U_\infty \leq$ 11 m/s were tested. A map of total concentration across the complete range of tunnel conditions for a fixed $\sigma_{gen} = 0.25$ is presented in Fig. 5.16a, and again for fixed $\Delta p_{gen} = 400$ kPa in Fig. 5.16b. Contours of the unconstrained generator parameter are superimposed on the concentration map for reference. The empty triangle markers in Fig. 5.16b denote the data that was rejected due to the visible presence of large millimetre size bubbles in the test-section, generated from gross audible cavitation in the generators operating at low σ_{gen}. In addition to this test matrix, measurements were made along the curve where the pressure in the plenum remained constant and the generators were operated with fixed $\sigma_{gen} = 0.25$ and $\Delta p_{gen} = 400$ kPa. The variation in dynamic pressure imposed by the changing test section velocity was compensated by changing the tunnel static pressure. These data, denoted by squares, are common to the two maps in Fig. 5.16.

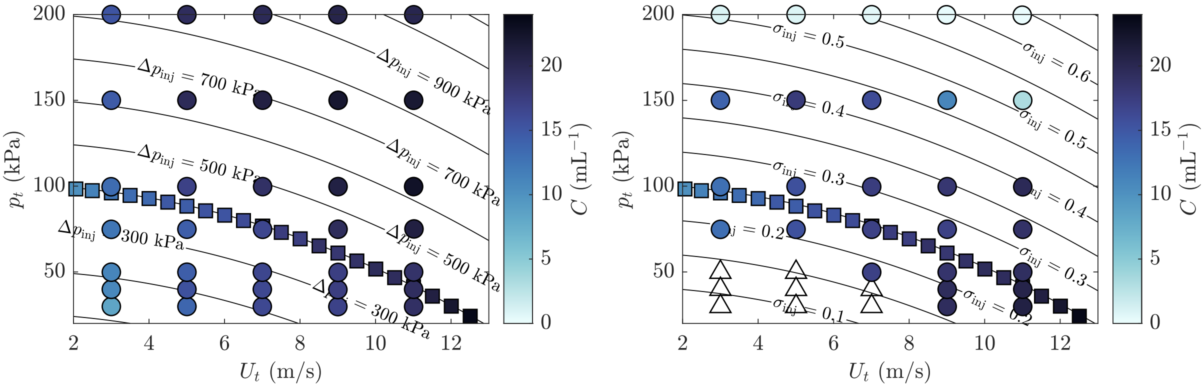

Figure 5.16: Total bubble concentration as a function of test section velocity and pressure. In (a), the injector cavitation index is constant at 0.25, and the driving pressure is represented by the contour levels. In (b), the driving pressure is constant at 400 kPa. The injector cavitation number is given by the contour levels. Triangle points indicate where the injectors were suffering gross cavitation. The squares are the same data as Fig. ref and are all $\Delta p_{\mathrm{gen}} = 400$ kPa.

For constant $\sigma_{gen} = 0.25$ bubble concentrations increased with an increase in tunnel velocity for a fixed tunnel pressure. The concentration also increased with tunnel pressure. The latter observation is in contrast with the expectation that higher tunnel pressure would aid bubble dissolution and result with a lower bubble concentration. However, an explanation for this behaviour can be found in the coupling of Δp_{gen} to the tunnel pressure. To maintain constant σ_{gen}, an increase in the tunnel pressure requires increased driving pressure, and consequent increase in bubble production.

In the case where the driving pressure was held constant, the changes resulting from the variation in the tunnel parameters were masked by the more dominant effects of σ_{gen}. Strong similarity was observed in the concentration within a σ_{gen} contour band. An increase in bubble concentration was observed with increasing tunnel velocity and decreasing tunnel pressure. The variability in bubble concentration between the contours followed similar trends to those presented in Fig. 5.14a for the $\Delta p = 400$ kPa series (marked with circles). When operating correctly the generators produced a high concentration of bubble population until $\sigma_{gen} \approx 0.4$. The concentration transitioned between $0.4 < \sigma_{gen} \leq 0.5$ and diminished until very few bubbles for $\sigma_{gen} > 0.5$ were produced. These observations foster the premise that the changes in the measured bubble concentrations are, to a large extent, a result of variation in σ_{gen}.

In order to assess the effect of the tunnel operating conditions on bubble population in isolation of the generator parameters, the testing has to be performed with a fixed injected population. A fixed nuclei population can be generated by maintaining a constant plenum and saturation pressure (p_p,p_s) to produce constant Δp_{gen} and σ_{gen}. With this test the opposing effects of residence time and pressure on the bubble population evolution between the plenum and test-section can be examined. The tests were conducted for the test-section velocity varied between 2–13 m/s and a constant plenum pressure of 102 kPa. To account for the change in dynamic pressure with variable velocity, the test-section static pressure was varied between 20–100 kPa. The results for both the bubble total concentration and size distribution are presented in Fig. 5.17. In the absence of dissolution, it would be expected that the measured concentration would decrease six times as the flow velocity increases from 2 to 12 m/s, due to a fixed bubble population being injected for a higher water flow-rate. In addition, the dynamic pressure change between the plenum and the test-section should induce a growth in bubble size as the reduction in pressure between the plenum and test-section becomes larger as velocity increases. Neither of these changes are observed in the results, which indicates that the dissolution dominates the bubble population evolution as increasing pressure and longer residence times lead to a decrease in the total concentration. From the size distribution plot, it can be observed that the decrease in total bubble concentration is mostly associated with dissolution of the small bubbles due to their large surface to volume ratio. These process do not have a prominent effect on the concentration for bubbles larger than 50 µm.

These results are encouraging as together they show that the measured population in the tunnel is fairly insensitive to tunnel operating conditions. In general then, dense bubble populations can be produced for the majority of tunnel conditions by maintaining $0.15 < \sigma_{gen} < 0.3$ and a driving pressure $\Delta p \geq 300$ kPa. This produces bubble concentrations $C \approx 15 - 20$ mL^{-1}. For very low tunnel speeds and pressures, a reduced σ_{gen} is required to avoid gross cavitation in the generator outlet. Intermediate distributions are obtained by increasing the cavitation number of the generators until they reach the edge of their operational range. The critical σ_{gen} varies with the driving pressure Δp, a pseudo-measure for the generator Reynolds number. Operation in this range enables production of bubble concentrations $C = 0 - 15$ mL^{-1} where the distribution of bubble sizes changes slightly with tunnel conditions. Lower dissolved oxygen concentrations also reduces the number of bubbles observed in the test section.

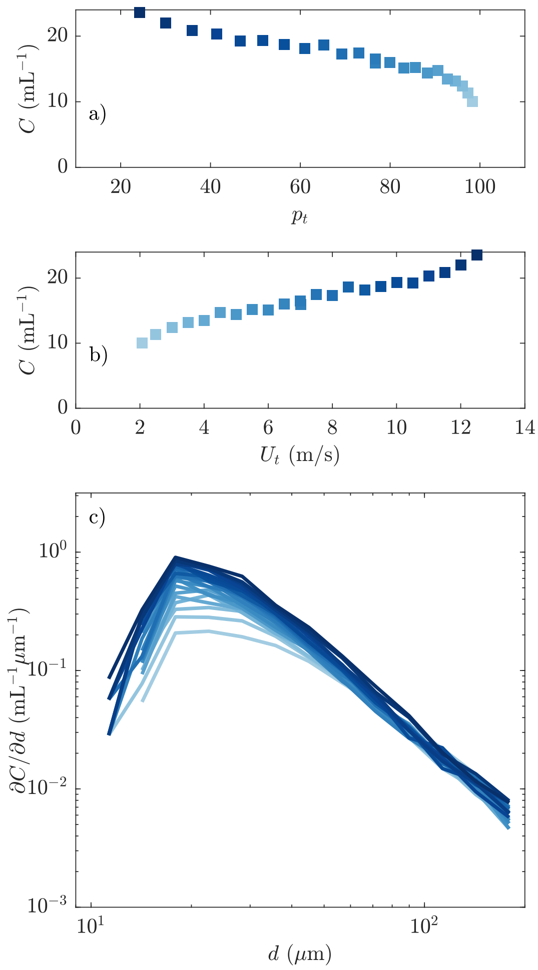

Figure 5.17: Bubble concentrations presented for the case where the generator parameters, $\sigma_{gen} = 0.25$ and $\Delta_{p_{gen}} = 400$ kPa, and plenum pressure, $p_p = 102$ kPa, remained fixed while tunnel parameters vary. For the same data, total concentration is plotted against σ_t in a), and against U_t in b). The distributions for these data are shown in c). The colour of data in all three plots are linked so that the tunnel conditions for each size distribution in c) is identified by its colour in plots a) and b).

5.6 Theoretical Dissolution

To contextualise the observed population, a quasi-steady model of bubble dynamics coupled with a diffusion model was applied to microbubbles of different sizes as they are advected from the injection point, through the tunnel contraction, to the test section entrance. Numerous models have been developed to account for the diffusion of gas between phases (Azbel, 1981), and studies such as Yu and Ceccio (1997) compare the congruence of select models to results obtained from experiments. Applicability of a model is usually assessed in terms of two limiting cases, with the understanding that most flows are a balanced combination of the two. In a stationary environment the problem is analogous to that of heat transfer in solid materials, where the ‘film model’ considers concentration gradients near the phase interface, and the related development of a diffusive boundary layer (Brennen, 2014). In turbulent flow the 'penetration model' considers the rate at which dissolved gas is convected from an interface by flow eddies (Azbel, 1981). Characterisation of the flow by Schmidt(Sc) and Sherwood(Sh) numbers aids in the selection and development of models. The majority of model validation has been performed on bubbles ~ 1 mm in diameter, using parameters such as the rise velocity to determine Sc and Sh numbers. The low Stokes number for bubbles on the order of micrometres in size makes determination of these values difficult and extrapolation of model results to microbubbles dubious. In addition, for the present work, Sc and Sh will vary as the level of turbulence changes between the location of bubble injection and the tunnel test section. Consequently, the film model (Brennen, 2014) was used to qualitatively discuss the effects of dissolution on the injected bubble population, where the magnitude of changes in bubble size with dissolution could vary.

As the flow approaches the tunnel test section, the change in the tunnel cross-section leads to an increase in the flow velocity and decrease in pressure. Presented in Brennen (2014), the familiar Rayleigh-Plesset equation for isothermal growth of a bubble is

$$\frac{p_v - p(t)}{\rho_l} + \frac{p_{G0}}{\rho_l}\left(\frac{r_0}{r}\right)^3 = r\ddot{r} + \frac{3}{2}\dot{r}^2 + \frac{3\nu_l}{r}\dot{r} + \frac{2\gamma}{\rho_l r}, \tag{5.7}$$

for a bubble of radius r with initial radius r_0 and surface tension γ. The initial pressure of gas inside the bubble is p_{G0}, p_v vapour pressure, and $p(t)$ the pressure experienced by the bubble at time t. During this process bubbles are assumed to grow or shrink rapidly to permit a quasi-steady solution. That is the time scale for inertial growth is protracted such that derivative terms in equation (5.7) are negligible. Omitting these terms and multiplying by r^3/ρ_l yields the equation

$$(p(t) - p_{\mathrm{v}})r^3 + 2\gamma r^2 - p_{G0}r_0^3 = 0, \tag{5.8}$$

which has been used to model bubble growth due to pressure change. Together with the 'film model' for dissolution presented in Brennen (2014), a marching scheme for small dt is developed. Once the change in radius with external fluid pressure is calculated from (5.8), the gas pressure inside the bubble is calculated using

$$p_b = 2\frac{\gamma}{r} + p(t) - p_v. \tag{5.9}$$

Bubbles contain a mixture of gasses, but are mostly comprised of nitrogen and oxygen liberated upon condensation of vapour cavities. In the solution, oxygen constitutes approximately 20% of the dissolved gases. It is assumed that the injected bubbles are comprised of a similar mixture. Together with Henry's Law

$$c_s = \frac{p}{H}, \tag{5.10}$$

where c_s is the concentration of gas inside the bubble, p the ambient pressure and H the Henry diffusion constant for a species of gas, the concentration of a single gas species inside a bubble can be calculated from its partial pressure. In practice the various gasses will dissolve at different rates but for simplicity it has been assumed that oxygen is representative of the general dissolution process. Diffusive processes will usually grow a concentration boundary layer around the bubble (the 'film model') that may be stripped away by small scale turbulence, and relative motion between the bubble and the bulk flow (the 'penetration model'). As has been discussed, the determination of turbulence intensity and its effect on bubbles of this size is unclear. The model described in Brennen (2014) with a fully developed diffusive boundary layer was then applied to calculate the diffusive growth of a bubble in the given time step.

$$R = \sqrt{R_0^2 + \frac{2D(c_\infty - c_{sO_2})\Delta t}{\rho_g}}. \tag{5.11}$$

The water temperature during these experiments was typically $T = 15$–$17°$, slightly less than Standard Temperature and Pressure $T_{STP} = 25°$, however for these calculations the typical diffusion coefficient of $D = 2 \times 10^{-5}$ cm^2/s was used. It should be noted that the derivation of (5.7) assumes no mass transfer occurs across the phase interface. While this is obviously not true in this setting, the time scale for diffusion is much greater such that this discrepancy will have little impact on the inertial bubble dynamics. In Fig. 5.18a the ambient pressure history experienced by a bubble between the injection point and the test section entrance is plotted for the tunnel velocity $U_t = 7$ m/s and the tunnel pressure $p_t = 78$ kPa. Bubbles spend the majority of their residence time in the slow moving plenum before being advected quickly through the contraction where the ambient pressure decreases by 20 kPa. In Fig. 5.18b the evolution of the bubble diameter calculated using the described model, with and without diffusion, and the pressure history from Fig. 5.18a has been plotted. The dissolved oxygen concentration was set to be $DO_2 = 30\%$ atmospheric saturation. Without diffusion a bubble 40 µm in size grows approximately 9% between the injection point and the test section. With diffusion, steady dissolution of the bubble causes it to shrink so that even after the pressure induced growth its size upon reaching the test section (d_t) is 5% lower than its original size (d_p). Dissolution occurs primarily during the extended residence in the plenum, with dynamic growth in the contraction occurring quickly at the end.

The balance of dissolution and dynamic growth depends on the bubble size and relative strength of surface tension during this process. The evolution of a range of bubble sizes

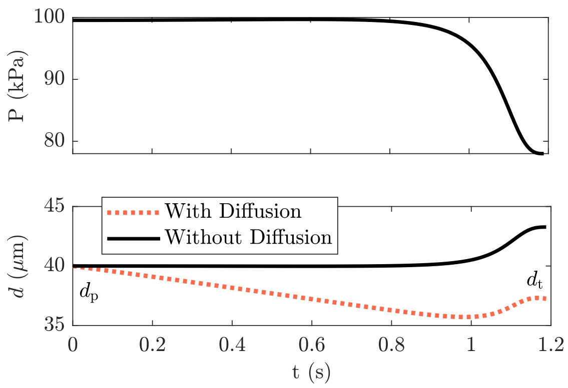

Figure 5.18: a) The pressure history of a single bubble injected at the centreline of the tunnel is plotted as calculated from Bernoulli's equation upstream of the test section through the contraction for a tunnel speed $U_t = 7$ m/s, $P_t = 78$ kPa, $DO_2 = 30\%$ atmospheric saturation. b) The evolution of the bubble size under these conditions as modelled with and without the effects of diffusion.

using the model with the diffusion effect included, normalised by the bubble original size, is plotted in Fig. 5.19. Bubbles larger than 50 µm grow in size, while the increase in internal pressure due to surface tension caused bubbles ≤ 21 µm to completely dissolve.

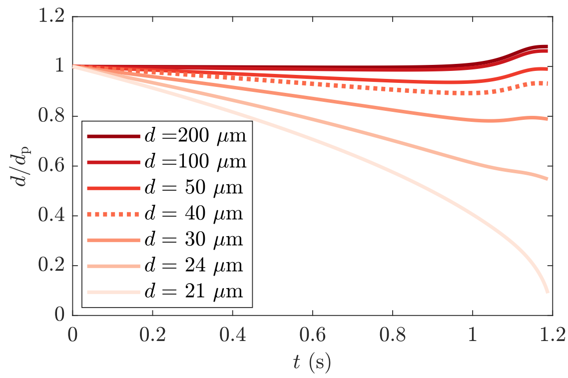

Figure 5.19: Evolution of bubble size for the range of initial bubble diameters as they are advected towards the test section for $U_t = 7$ m/s, $P_t = 78$ kPa, $DO_2 = 30\%$ atmospheric saturation.

The effect of tunnel conditions on the injected population is examined by using the theoretical model to calculate the bubble sizes upon reaching the test-section across the range of tunnel velocities and pressures. The ratio of the calculated and initial bubble size is then plotted against the initial bubble size. In Fig. 5.20, the effect of tunnel velocity on bubble size ratio is presented for velocities between 2 and 12 m/s while the test section pressure is held constant. Due to reduced residence time, the minimum bubble size at the injection point d_p required for a bubble to avoid being dissolved before the test-section, i.e. $d_t/d_p \geq 0$, decreases as the tunnel velocity is increased. For $U_t = 2$ m/s the pressure change through the contraction is so small that the effects of dissolution cause all bubbles to reduce in size. As the tunnel velocity increases the pressure change effect becomes increasingly dominant and at 12 m/s all but the smallest bubbles increase from their initial size.

For a fixed velocity of $U_t = 7$ m/s the tunnel pressure was varied from 10 to 200 kPa and the resulting effect on the bubble sizes is plotted in Fig. 5.21. Low test section pressures amplified bubble growth stemming from pressure change through the contraction. This was the result of increased tension applied to the bubbles as pressure in the tunnel approached their critical pressure. Decrease in the ambient pressure also resulted in a decrease in the minimum bubble size that completely dissolved.

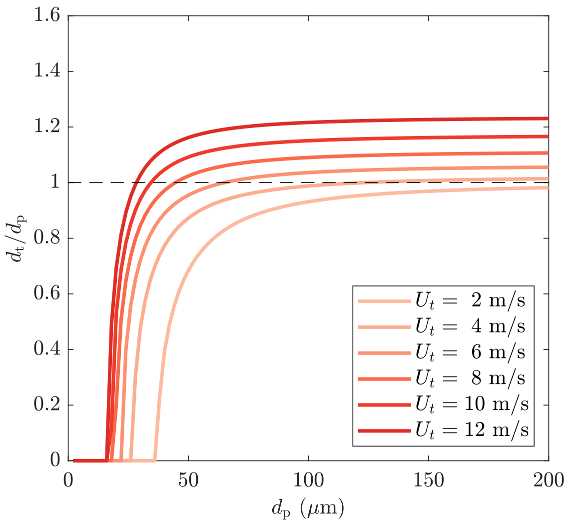

Figure 5.20: The ratio of the final versus initial bubble size, across the range of initial bubble sizes, plotted for various tunnel velocities. The tunnel pressure is kept constant at $P_t = 78$ kPa, with dissolved oxygen concentration of $DO_2 = 30\%$ atmospheric saturation.

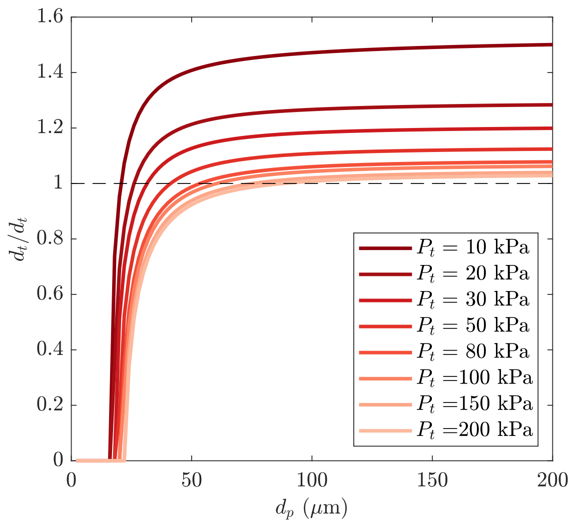

Figure 5.21: The ratio of the final versus initial bubble size, across the range of initial bubble sizes, plotted for various tunnel pressures. The tunnel velocity is kept constant at $U_t = 7$ m/s, with dissolved oxygen concentration of $DO_2 = 30\%$ atmospheric saturation.

In experimental data, tunnel parameters could not independently varied without affecting generator parameters. A useful capability of the model is that it can be used to predict the effect of changing only one tunnel parameter for a set initial bubble population. The model was used to calculate a theoretical bubble population in the plenum from a bubble distribution measured in the test-section. This theoretical initial bubble population was then forward mapped to the test-section population while changing only one of the tunnel parameters. In Fig. 5.22 the simulated effect of changing tunnel pressure for a constant tunnel velocity is plotted. In Fig. 5.23 the results of the same manipulation, but for changing tunnel velocity and constant pressure, are presented.

From Fig. 5.22 an increase in the concentration of larger bubbles can be seen as the pressure in the tunnel is reduced, while the concentration of small bubbles decreased. This is in contrast to the measurements presented in Fig. 5.17. The reason for this discrepancy stems from the model mapping principle. As the model functions by only mapping an initial bubble size to a final bubble size, the bubble size distribution curve can only be shifted and stretched along the horizontal axis, i.e. bubble diameter axis, while the curves remain unaffected along the concentration axis. In Fig. 5.23, it can be seen that the concentration of large bubbles increased following an increase in the tunnel velocity. The shift in size, in particular for small bubbles, is more pronounced at the lower tunnel velocities due to increased dissolution with extended residence time in the plenum.

There are two caveats to these simulated results. The first is that this modelling technique does not fundamentally alter the observed distribution, but rather maps the observed bubble size to a new diameter. It is then unable to capture non-linear change that is probabilistic in nature. For example, different bubbles within a population may experience random pressure histories imposed by the flow turbulence that would cause even a mono-disperse population to result in a distribution of resultant diameters. The second caveat, is that the consistent roll-off in concentration as the bubble size decreases below 15 µm might be artefact of optical measurement techniques at the edge of their dynamic range. It is possible that the power law like behaviour observed for larger sizes continues well below the lower limit of the MSI technique. The observed roll-off has been reported in numerous studies that utilise optical bubble/particle measurement (Liu et al., 1993; Russell et al., 2016; Mées et al., 2010). The fact that these mapped distributions do not concur with the measured data in Fig. 5.17 is therefore not surprising.

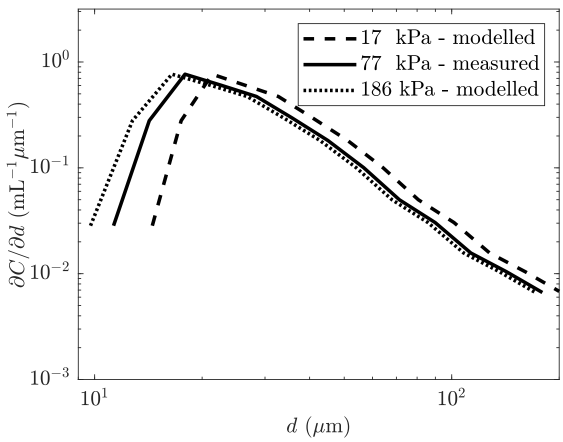

Figure 5.22: A plot of modelled test-section populations for different tunnel pressures (p_t =17 and 186 kPa), obtained using backward mapping of the test-section population measured in the experiment (p_t = 77 kPa) to the plenum, and then forward mapped back to the test-section for different tunnel conditions. The experimental measurements were obtained for U_t = 7 m/s, σ_{gen} = 0.25 and $\Delta_{p_{gen}}$ = 400 kPa.

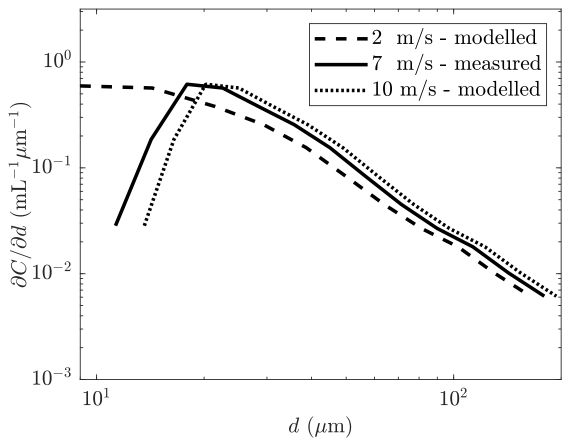

Figure 5.23: A plot of modelled test-section populations for different tunnel velocities (U_t =2 and 10 m/s), obtained using backward mapping of the test-section population measured in the experiment (U_t = 7 m/s) to the plenum, and then forward mapped back to the test-section for different tunnel conditions. The experimental measurements were obtained for p_t = 77 kPa, σ_{gen} = 0.25 and $\Delta_{p_{gen}}$ = 400 kPa.

As discussed above, while an extensive body of literature exists with alternate model formulations, the more refined of these require knowledge of flow properties currently unavailable. In particular, determination of the Schmidt and Sherwood numbers is recommended (Azbel, 1981). Acknowledging that these characteristic values are expected to vary between the plenum and the test section, their measurement at even one location upstream of the test section would enable the use of improved modelling methods. In light of this, while the above model offers some insight about the populations that have been measured in the test section, definitive conclusions about the modelled upstream population are reserved until these improvements are made.

5.7 Conclusions

It has been demonstrated that injected nuclei populations can be measured for experiments in hydrodynamic test facilities with the MSI technique. Populations of 10–200 µm in diameter were measured with concentrations of 0–60 bubbles/mL. This system forms a vital component in the measurement of cavitation nuclei in hydrodynamic test facilities, capable of measuring semi-sparse bubble populations.

The acquisition and processing of microbubble measurements with MSI have a fast turn-around such that nuclei concentration measurements are approaching real-time. The method presented to calibrate the size dependent detection volume is of benefit as it is an *in-situ* calibration, which also extends the dynamic range of the technique. Estimation of the total bubble concentration was within 5% of the sampled concentration after only 100 bubbles were counted, but it was found that 10^4 detections were necessary for convergence of bubble size histograms. The large number of detections led the uncertainty in the total concentration measurements to be within 1%.

Tunnel velocity, pressure and dissolved oxygen concentration, as well as microbubble generator feed pressure (and hence saturation pressure) were varied, and the resultant concentration of bubbles measured in the test section. Low dissolved oxygen content in the tunnel led the measured population to decrease as they dissolved in the under-saturated environment between injection upstream and measurement in the test section. This dissolution is also a function of residence time, so that the measured population increases with tunnel speed. Generator parameters are coupled to tunnel operating conditions through the pressure in the plenum where nuclei are injected. This produces a complex balance between bubble production and dissolution processes. Similar distributions are produced in high concentrations for low generator cavitation numbers. These distributions follow a power law suggesting that the generated populations also follow a power law. Intermediate concentrations are achieved at higher generator cavitation numbers, but exhibit a different distribution of bubble sizes. The critical cavitation number at which the generators begin to produce high concentrations increases with the driving pressure. It is reasoned that that this is an effect of increased generator Reynolds number but also the total gas content available to be liberated from the injected fluid. To decouple the microbubble production and dissolution processes, and to develop a model for predicting the population in the test section, measurements of the population upstream in the plenum are required.

5.8 Acknowledgements

This project was supported by the Australian Defence Science and Technology Group (Dr. Dev Ranmuthugala) through the 2017 U.S. Multidisciplinary University Research Initiative (Dr David Clarke), and the US Office of Naval Research (Dr. Ki-Han Kim, Program Officer) and ONR Global (Dr. Sung-Eun Kim) through NICOP S&T Grant no. N62909-15-1-2019. The authors are grateful for the technical assistance provided by Mr. Steven Kent and Mr. Robert Wrigley when conducting these experiments.

Chapter 6

General Conclusions and Recommendations

This research has been guided by the following questions:

- How do the Reynolds and cavitation numbers influence the development of sheet cavitation geometry and topography, and subsequent breakup and microbubble generation?
- How does free-stream seeding concentration affect cavity geometry and topography, and subsequent microbubble generation?
- Can off-the-shelf imaging components be used to produce a rigorously calibrated interferometric microbubble measurements system suitable to measure semi-sparse populations in a cavitation water tunnel or other hydrodynamic test facilities?
- With such an interferometric method, what seeding populations are produced in the CRL hydrodynamic test facilities with changing tunnel operating conditions?

From this research the following conclusion are drawn in answer of these questions.

6.1 Conclusions

The influence of Reynolds and cavitation numbers on the development of sheet cavity geometry and topography, and subsequent breakup and microbubble generation has been studied experimentally both qualitatively and quantitatively, with and without free-stream cavitation nuclei.

In the unseeded flow the cavity leading edge is composed of laminar cells resulting from a complex interaction between the separating unstable laminar boundary layer and inter-facial effects. Wider cells grow preferentially with smaller neighbours reducing in size until ultimately these smaller cells are washed downstream by the inter-cellular flow of their larger neighbours. However, wider cells have an increasing chance to undergo division so that an equilibrium between these processes occurs. The average of the cell widths tends to reduce with Reynolds number converging for values greater than about 1.3×10^6. Waves develop in the overlying laminar boundary layer due to Kelvin-Helmholtz instabilities driving coherent breakup of the cavity trailing edge into cavitating vortical filaments. With downstream advection the filaments condense and break up into microbubbles of incondensable gas in the far wake. The scale or wavelength of the instabilities is mildly dependent on the Reynolds and cavitation numbers. In the wake, the volume of shed vortices and concentrations of the microbubbles generated increase with Reynolds number. For the measured range, bubble sizes and concentrations decreased as the cavitation number decreased whereas the measured void fraction increased, indicating a greater production of larger diameter bubbles.

With the addition of free-stream microbubbles the leading edge cell structure is broken up by the activation of nuclei, and the steady cavity interface is 'washed away' by the disturbance introduced from the travelling bubble cavitation. When nuclei are sparsely distributed bubble activations remain discrete, but, for higher seeding densities bubbles growth is confined by neighbouring activations to form a cellular but almost continuous cavity. Consequently, the condensation and breakup region of the cavity changes with the nuclei concentration. The number of activations about the hydrofoil have been related to the seeding concentration measured using IMI/MSI with a approximately linear trend. From high resolution still photography that captures the overall flow features it is observed that wake bubble populations increase with seeding concentration. However, shadowgraphy reveals that microbubble concentration in the range of 5-50 µm increases for low seeding levels but decrease with further increase in seeding concentration. In this range wake microbubble concentrations for low seeding concentrations are highly sensitive to small changes in the active freestream nuclei population but become only mildly sensitive to order of magnitude changes for higher upstream concentrations. In these later shadowgraphy results it was recognised that the low detection rate of larger bubble sizes caused higher uncertainty in concentration measurements. Conservatively, results were then limited to bubbles less than 50µm in size. For these measurements a high magnification factor was chosen to resolve small bubbles in fine detail. A 5µm bubble covered 17 pixels on the image sensor. With a lower magnification factor, and by accepting small bubbles to be less well resolved, the depth of field of images could be greatly increased in order to capture increased detection counts of larger bubbles.

To measure the upstream population over a wide range of sizes and refine concentration measurements, the MSI technique was investigated using simultaneous shadow imaging of mono-disperse microbubbles in a test chamber separate from the tunnel but possessing similar optical access. Theoretical and experimental calibration of MSI for the measurement of microbubbles was demonstrated at the experimentally convenient scatter angle of 90°, and the congruence between MSI bubble sizing theory and experimental results validated. This required the determination of two constants, calculated independently of one another. The constant of proportionality between the scattering bubble diameter and the angular wavelength was determined from Lorentz Mie theory and is independent of the experimental optics. The second constant relates to the specific optical arrangement used in a measurement. The constant serves to describe the proportionality between the interference pattern measured in pixels and the angular distance in the scattering plane this represents, and a practical calibration was demonstrated. The comparison of the measured diameters by shadow and MSI by this approach within the range 30–150 µm is less than 1 µm, validating the agreement between MSI theory and its practical application.

The experiment could position and measure the location of bubbles within the MSI measurement beam. In addition, the spacing between bubbles could be altered to enable individual bubble measurements. This was used to analyse and experimentally validate the size dependent effective measurement volume of the technique. A rationalised approach for the application of the MSI technique in water tunnels or other hydrodynamic test facilities using conventional laser diagnostic equipment was demonstrated. Although bubbles below 30 µm were not tested the method is applicable to sizes below 10 µm but with increased uncertainty. The approach is applicable for measurement of microbubbles in the diameter range 10–175 µm and for concentration ranges up to 10–100 bubbles per millilitre.

To demonstrate the refined technique's suitability for the measurement of nuclei in hydrodynamic test facilities the method has been applied to better understand the range of seeded nuclei that can be modelled in the cavitation tunnel at University of Tasmania and analyse the effect of variable operating conditions on the populations present in the test section. Populations of 10–200 µm in diameter were measured with concentrations of 0–60 bubbles/mL. Tunnel velocity, pressure and dissolved oxygen concentration, as well as microbubble generator feed pressure (and hence saturation pressure) were varied, and the resultant concentration of bubbles measured in the test section.

Low dissolved oxygen content in the tunnel led the measured population to decrease as they dissolved in the under-saturated environment between injection upstream and measurement in the test section. This dissolution is also a function of residence time so that the measured population concentration in the test section increased with tunnel speed. This is despite the diluting effect of an increased velocity where the injected population will be dispersed throughout a greater volume. Generator parameters are coupled to tunnel operating conditions through the pressure in the plenum where nuclei are injected. This produces a complex balance between bubble production and dissolution processes. Similar distributions of seeded nuclei size are produced in high concentrations for low generator cavitation numbers, approximately $\sigma = 0.25$. For these high concentrations the distributions measured in the test section follow a power law suggesting that the generated populations also follow a power law. Intermediate microbubble concentrations $C = 5$–$15\ \mathrm{mL}^{-1}$ are achieved at higher generator cavitation numbers, but exhibit a different distribution of bubble sizes. The critical cavitation number at which the generators begin to produce high concentrations increases with the driving pressure. It is reasoned that this is an effect of increased generator Reynolds number but also the total gas content available to be liberated from the injected fluid. To decouple the microbubble production and dissolution processes and to develop a model for predicting the population in the test section, measurements of the population upstream in the plenum would be required.

The acquisition and processing of microbubble measurements with MSI have a fast turn-around such that nuclei concentration measurements are approaching real-time. The method presented to calibrate the size dependent detection volume is of benefit as it is an *in-situ* calibration, which also extends the dynamic range of the technique. Estimation of the total bubble concentration is rapid requiring very few detections, but $\mathcal{O}(10^4)$ detections were necessary for convergence of bubble size histograms.

In total this work provides a greater understanding of the processes that occur involving microbubbles about cavitation hydrofoils both in terms of nucleation and the generated wake populations. These flows remain a challenge due to the large range of length and times scales involved, and as has been demonstrated the large range of microbubble concentration and sizes. To study these flows rigorously requires examination of not just how they behave but also the complex diagnostics required to measure them. These new insights open up further opportunities to re-examine these physics in many contexts armed with the techniques to measure them. The efficiency of pump and turbomachinery can benefit greatly by knowing the susceptibility of the incoming flow. In addition, commercial freight and transport vessels are under constant pressure to increase fuel efficiency and component lifespan, while decreasing emissions – both chemical and acoustic – in which cavitation is a prescient concern. Finally, the development of modern naval vessels are at the forefront of these effort, which demand fast, quiet vessels where an understanding of both developed cavitation the inception characteristics of a vessel are critical.

6.2 Future Work

Measurements of the wake concentration presented in this work focussed on bubbles typically 10–100 µm in diameter that contribute to the long lived wake behind surface vessels. However, it has been discussed that while larger bubbles are present in the cavity wake, lower magnifications are required to effectively resolved these sizes with shadowgraphy microscopy. An investigation with multiple magnifications would be of significant value, being able to resolve the complete spectrum of sizes produced by the attached cavity in order to investigate total void fraction and the splitting/coalescence of bubbles in the far wake. Testing was also performed with a low dissolved oxygen concentration that was nominally fixed. Typical concentrations were approximately 30% of the saturation concentration at atmospheric pressure. However, the relative saturation concentration will therefore changed with pressure during testing. Given the matrix of measurement locations and test conditions in Chapter 2, maintaining a fixed relative concentration was unfeasible. Repeat testing with a limited set of conditions maintaining the relative concentration to minimise difference in diffusive rates would be valuable.

In addition, the effects of nuclei on cavitation were investigated at four seeding concentrations including testing without the activation of freestream nuclei. Cavitation behaviour was found to be sensitive to low seeding concentrations and so further testing with an increased number of seeding concentrations would be of interest to explore this relationship further. Methods to generate these populations and the techniques to measure them with the required precision in cavitation tunnels has been demonstrated in the later half of this work but their application to such measurements have not yet been undertaken.

While populations in the test section of the cavitation tunnel can be measured in near real-time, measurements of both the bubble populations in the test section and in the plenum are required to further develop the modelling of dissolution for predicting bubble concentrations and distributions in the test section for proposed test conditions prior to testing. It would also be of great benefit if the speed of acquisition and processing of MSI technique could be further developed to provide real-time monitoring of nuclei populations. While injected nuclei seeding populations within the tunnel are quasi-steady, it would enable refined matching of test conditions between full scale results or results from other facilities. In addition, for complex test geometries the local seeding concentrations may differ from the otherwise homogenous population in the test section. Such a technology would also be advantageous for naval vessels which could adjust and optimise their performance in accordance with the measured nuclei population.

Bibliography

H.-E. Albrecht, N. Damaschke, M. Borys, and C. Tropea. Laser Doppler and phase Doppler measurement techniques. Springer Science & Business Media, 2013. ISBN 3662051656.

S. Ata. Coalescence of bubbles covered by particles. Langmuir, 24(12):6085–6091, 2008.

D. Azbel. Two phase flows in chemical engineering. Cambridge University Press, 1981.

S. Balachandar and J. K. Eaton. Turbulent dispersed multiphase flow. Annual review of fluid mechanics, 42:111–133, 2010.

M. Billet. Cavitation nuclei measurements with an optical system. Journal of fluids engineering, 108(3):366–372, 1986.

M. L. Billet and E. M. Gates. A comparison of two optical techniques for measuring cavitation nuclei. Journal of Fluids Engineering, 103(1):8–13, 1981.

M. Birvalski and M. X. van Rijsbergen. Application of interferometric particle imaging to cavitation nuclei measurements in a ship model basin. In Proceedings of the 19th 2018 International Symposium on the Application of Laser and Imaging Techniques to Fluid Mechanics, Lisbon, 2018.

D. Blanchard and A. Woodcock. Bubble formation and modification in the sea and its meteorological significance. Tellus, 9(2):145–158, 1957.

C. F. Bohren and D. R. Huffman. Absorption and scattering of light by small particles. John Wiley & Sons, 2008.

R. Boucheron, V. Aumelas, M. Donnet, D. Fréchou, and A. Poidatz. Comparative study of optical experimental methods for micro-bubble sizing. In 19th International Symposium on Applications of Laser Techniques to Fluid mechanics, page Paper 40, Lisbon, Portugal, July 16-19 2018.

P. A. Brandner. Microbubbles and cavitation: Microscales to macroscales. In Proceedings of the 10th International Symposium on Cavitation (CAV2018). ASME Press, 2018.

P. A. Brandner, Y. Lecoffre, and G. J. Walker. Development of an australian national facility for cavitation research. In Sixth International Symposium on Cavitation, pages 1–9, 2006.

P. A. Brandner, Y. Lecoffre, and G. J. Walker. Design considerations in the development of a modern cavitation tunnel. In Australasian Fluid Mechanics Conference, pages 630–637, 2007.

P. A. Brandner, G. J. Walker, P. N. Niekamp, and B. Anderson. An experimental investigation of cloud cavitation about a sphere. Journal of Fluid Mechanics, 656:147–176, 2010a.

P. A. Brandner, G. Wright, B. W. Pearce, L. Goldsworthy, and G. J. Walker. An experimental investigation of microbubble generation in confined turbulent jet. In 17th Australasian Fluid Mechanics Conference, 2010b.

P. A. Brandner, B. W. Pearce, and K. L. De Graaf. Cavitation about a jet in crossflow. Journal of Fluid Mechanics, 768:141–174, 2015.

N. Breitz and H. Medwin. Instrumentation for insitu acoustical measurements of bubble spectra under breaking waves. The Journal of the Acoustical Society of America, 86 (2):739–743, 1989.

C. E. Brennen. Fission of collapsing cavitation bubbles. Journal of Fluid Mechanics, 472: 153–166, 2002.

C. E. Brennen. Fundamentals of multiphase flow. Cambridge university press, 2005.

C. E. Brennen. Cavitation and bubble dynamics. Cambridge University Press, 2014.

L. Briançon-Marjollet, J. P. Franc, and J. M. Michel. Transient bubbles interacting with an attached cavity and the boundary layer. Journal of Fluid Mechanics, 218:355–376, 1990. doi: 10.1017/S0022112090001033.

M. Brunel and H. Shen. Design of ILIDS configurations for droplet characterization. Particuology, 11(2):148–157, 2013. ISSN 1674-2001. doi: https://doi.org/10.1016/j.partic.2012.06.014. URL `http://www.sciencedirect.com/science/article/pii/S1674200112001927`.

P. Carrica, D. Drew, F. Bonetto, and R. Lahey Jr. A polydisperse model for bubbly two-phase flow around a surface ship. International journal of multiphase flow, 25(2): 257–305, 1999.

A. M. Castro and P. M. Carrica. Eulerian polydispersed modeling of bubbly flows around ships with application to athena r/v. International Shipbuilding Progress, 60(1-4): 403–433, 2013.

A. M. Castro, J. Li, M. Hyman, and P. M. Carrica. Turbulent and cavity free surface bubble entrainment with application to ship hydrodynamics. In 30th Symposium on Naval Hydrodynamics, 2014.

A. M. Castro, J. Li, and P. M. Carrica. A mechanistic model of bubble entrainment in turbulent free surface flows. International Journal of Multiphase Flow, 86:35–55, 2016.

S. L. Ceccio and C. E. Brennen. Observations of the dynamics and acoustics of travelling bubble cavitation. Journal of Fluid Mechanics, 233:633–660, 1991.

G. L. Chahine and R. Duraiswami. Dynamical interactions in a multi-bubble cloud. Journal of fluids engineering, 114(4):680–686, 1992.

G. L. Chahine and K. M. Kalumuck. Development of a near real-time instrument for nuclei measurement: the ABS Acoustic Bubble Spectrometer®. In ASME/JSME 2003 4th Joint Fluids Summer Engineering Conference, pages 183–191. American Society of Mechanical Engineers, 2003.

G. L. Chahine, K. M. Kalumuck, L. Y. Cheng, and F. G. Validation of bubble distribution measurements of the abs acoustic bubble spectrometer with high speed video photography. In 4th International Symposium on Cavitation, California Institute of Technology, Pasadena, CA., 2001.

H. Chanson and P. D. Cummings. Effects of plunging breakers on the gas contents in the oceans. Marine Technology Society Journal, 28(3):22–32, 1994.

N. Damaschke, H. Nobach, and C. Tropea. Optical limits of particle concentration for multi-dimensional particle sizing techniques in fluid mechanics. Experiments in Fluids, 32(2):143–152, 2002. ISSN 1432-1114. doi: 10.1007/s00348-001-0371-x. URL `https://doi.org/10.1007/s00348-001-0371-x`.

Y. K. De Chizelle, S. Ceccio, and C. Brennen. Observations and scaling of travelling bubble cavitation. Journal of Fluid Mechanics, 293:99–126, 1995.

K. L. De Graaf, G. A. Zarruk, P. A. Brandner, and B. W. Pearce. Microbubble content in the wake of a cavitating hydrofoil. In 19th Australasian Fluid Mechanics Conference, pages 1–4, 2014.

K. L. De Graaf, B. W. Pearce, and P. A. Brandner. The influence of nucleation on cloud cavitation about a sphere. In 16th International Symposium on Transport Phenomena and Dynamics of Rotating Machinery, volume 17, pages 1–7, 2016.

K. L. de Graaf, P. A. Brandner, and B. W. Pearce. Spectral content of cloud cavitation about a sphere. Journal of Fluid Mechanics, 812, 2017.

G. B. Deane and M. D. Stokes. Scale dependence of bubble creation mechanisms in breaking waves. Nature, 418(6900):839, 2002.

S. Dehaeck and J. P. A. J. van Beeck. Designing a maximum precision interferometric particle imaging set-up. Experiments in Fluids, 42(5):767–781, 2007. ISSN 1432-1114. doi: 10.1007/s00348-007-0286-2. URL `https://doi.org/10.1007/s00348-007-0286-2`.

C. Doolan, P. A. Brandner, D. Butler, B. W. Pearce, D. Moreau, and L. Brooks. Hydroacoustic characterisation of the amc cavitation tunnel. In Acoustics 2013, pages 1–7, 2013.

C. Dunker, C. Roloff, and A. Graßmann. Interferometric laser imaging for in-flight cloud droplet sizing. Measurement Science and Technology, 27(12):124004, 2016. ISSN 0957-0233. URL `http://stacks.iop.org/0957-0233/27/i=12/a=124004`.

R. Duraiswami, S. Prabhukumar, and G. L. Chahine. Bubble counting using an inverse acoustic scattering method. The Journal of the Acoustical Society of America, 104(5): 2699–2717, 1998.

E. Ebert. Optische Messtechnik zur Charakterisierung maritimer Kavitationskeime. Thesis, Rostock University, 2015.

E. Ebert, A. Kleinwächter, R. Kostbade, and N. Damaschke. Interferometric particle imaging for particle characterization in the wake flow of a ferry ship and in cavitation tunnels. In Proceedings of Lisbon 17th 2014 International Symposium On Applications of Laser Techniques to Fluid Mechanics, Lisbon, 2014.

E. Ebert, W. Kröger, and N. Damaschke. Hydrodynamic nuclei concentration technique in cavitation research and comparison to phase-doppler measurements. Journal of Physics: Conference Series, 656(1):012111, 2015. ISSN 1742-6596. URL `http://stacks.iop.org/1742-6596/656/i=1/a=012111`.

E. Ebert, A. Kleinwächter, R. Kostbade, and N. Damaschke. HDNC - Nuclei size and number concentration estimation with detection volume correction. In 31st Symposium on Naval Hydrodynamics, Monterey, California, 2016.

R. J. Etter, J. M. Cutbirth, S. L. Ceccio, D. R. Dowling, and M. Perlin. High Reynolds number experimentation in the US Navy's William B Morgan large cavitation channel. Measurement Science and Technology, 16(9):1701, 2005.

R. O. Fox. Large-eddy-simulation tools for multiphase flows. Annual Review of Fluid Mechanics, 44:47–76, 2012.

H. Ganesh, S. A. Mäkiharju, and S. L. Ceccio. Partial cavity shedding due to the propagation of shock waves in bubbly flows. In Proceedings of the 30th symposium on naval hydrodynamics, 2014.

H. Ganesh, S. A. Mäkiharju, and S. L. Ceccio. Bubbly shock propagation as a mechanism for sheet-to-cloud transition of partial cavities. Journal of Fluid Mechanics, 802:37–78, 2016.

B. Gindroz. Propeller cavitation characteristics: the practical interest of nuclei measurements in test facilities and at sea. In Proceedings of the ASME FED Symposium on Cavitation, 1995.

B. Gindroz and M. L. Billet. Influence of the nuclei on the cavitation inception for different types of cavitation on ship propellers. Journal of fluids engineering, 120(1):171–178, 1998.

D. Giosio, B. Pearce, and P. Brandner. Influence of pressure on microbubble production rate in a confined turbulent jet. In 20th Australasian Fluid Mechanics Conference (20AFMC), pages 1–4, 2016.

A. Glover, S. Skippon, and R. Boyle. Interferometric laser imaging for droplet sizing: a method for droplet-size measurement in sparse spray systems. Applied Optics, 34(36): 8409–8421, 1995.

A. Gnanaskandan and K. Mahesh. Large eddy simulation of sheet to cloud cavitation. In Proceedings of the 30th Symposium on Naval Hydrodynamics, pages 1–13, 2014.

A. Gnanaskandan and K. Mahesh. A numerical method to simulate turbulent cavitating flows. International Journal of Multiphase Flow, 70:22–34, 2015.

A. Gnanaskandan and K. Mahesh. Large eddy simulation of the transition from sheet to cloud cavitation over a wedge. International Journal of Multiphase Flow, 100(83): 86–102, 2016a.

A. Gnanaskandan and K. Mahesh. Numerical investigation of near-wake characteristics of cavitating flow over a circular cylinder. Journal of Fluid Mechanics, 790:453–491, 2016b.

S. Gowing and Y. Shen. Nuclei effects on tip vortex cavitation scaling, 2001.

S. Gowing, L. Briançon-Marjollet, D. Frechou, and V. Godeffroy. Dissolved gas and nuclei effects on tip vortex cavitation inception and cavitating core size. In Proceedings of 5th international symposium on cavitation, pages 173–180, 1995.

A. Graßmann and F. Peters. Size measurement of very small spherical particles by Mie Scattering Imaging (MSI). Particle & Particle Systems Characterization, 21(5):379–389, 2004. doi: doi:10.1002/ppsc.200400894. URL `https://onlinelibrary.wiley.com/doi/abs/10.1002/ppsc.200400894`.

K. H. Hesselbacher, K. Anders, and A. Frohn. Experimental investigation of gaussian beam effects on the accuracy of a droplet sizing method. Applied Optics, 30(33):4930–4935, 1991. doi: 10.1364/AO.30.004930. URL `http://ao.osa.org/abstract.cfm?URI=ao-30-33-4930`.

J. W. Holl and J. A. Carroll. Observations of the various types of limited cavitation on axisymmetric bodies. Journal of Fluids Engineering, 103(3):415–424, 1981.

C.-T. Hsiao and G. L. Chahine. Scaling of tip vortex cavitation inception noise with a bubble dynamics model accounting for nuclei size distribution. Journal of fluids engineering, 127(1):55–65, 2005.

C.-T. Hsiao, J. Ma, and G. L. Chahine. Numerical study of bubble cloud dynamics near a rigid wall. In Proceedings of the 31st Symposium on Naval Hydrodynamics. Office of Naval Research Science and Technology, 2016.

C.-T. Hsiao, J. Ma, and G. L. Chahine. Multiscale tow-phase flow modeling of sheet and cloud cavitation. International Journal of Multiphase Flow, 90:102–117, 2017.

C.-T. Hsiao, J. Ma, and G. L. Chahine. 3d simulations of cavitation bubble breakup over a lifting surface. In Proceedings of the Sixth International Symposium on Marine Propulsors - smp'19, 2019.

B. Huang, A. Ducoin, and Y. L. Young. Physical and numerical investigation of cavitating flows around a pitching hydrofoil. Physics of Fluids, 25(10):102109, 2013.

H. C. Hulst and H. C. van de Hulst. Light scattering by small particles. Courier Corporation, 1981.

B. Ji, X. Luo, Y. Wu, X. Peng, and Y. Duan. Numerical analysis of unsteady cavitating turbulent flow and shedding horse-shoe vortex structure around a twisted hydrofoil. International Journal of Multiphase Flow, 51:33–43, 2013.

B. Ji, X. X. Peng, X. P. Long, X. W. Luo, and Y. L. Wu. Numerical evaluation of cavitation shedding structure around 3d hydrofoil: Comparison of pans, les and rans results with experiments. In Journal of Physics: Conference Series, volume 656, page 012127. IOP Publishing, 2015.

A. Karn, C. Ellis, J. Hong, and R. E. Arndt. Investigations into the turbulent bubbly wake of a ventilated hydrofoil: Moving toward improved turbine aeration techniques. Experimental Thermal and Fluid Science, 64:186–195, 2015.

J. Katz and J. Sheng. Applications of holography in fluid mechanics and particle dynamics. Annual Review of Fluid Mechanics, 42:531–555, 2010.

J. Katz, S. Gowing, T. O'Hern, and A. Acosta. A comparative study between holographic and light-scattering techniques of microbubble detection. In Measuring Techniques in Gas-Liquid Two-Phase Flows, pages 41–66. Springer, 1984.

T. Kawaguchi and M. Maeda. Measurement technigure for analysis in two-phase flows involving distributed size of droplets and bubble sizing using interferometric method - planar simultaneous measurement of size and velocity vector field. Multiphase Science and Technology, 17(1-2):57–77, 2005. doi: 10.1615/MultScienTechn.v17.i1-2.40. URL `http://dl.begellhouse.com/journals/5af8c23d50e0a883,704df4bb0366a0d1,3e6dc3021653`

M. Khoo, J. Venning, B. Pearce, P. Brandner, and Y. Lecoffre. Development of a cavitation susceptibility meter for nuclei size distribution measurements. In 20th Australasian Fluid Mechanics Conference (20AFMC), pages 1–4, 2016.

M. Khoo, J. Venning, K. Takahashi, J. Ari, T. Mori, B. Pearce, P. Brandner, and D. Ranmuthugala. Joint research between australia and japan on the cavitation inception of marine propellers and control surfaces. In MAST Asia 2017, pages 1–6, 2017.

M. Khoo, J. Venning, B. Pearce, and P. Brandner. Nucleation effects on hydrofoil tip vortex cavitation (under review). 2019.

K. T. Kiger and J. H. Duncan. Air-entrainment mechanisms in plunging jets and breaking waves. Annual Review of Fluid Mechanics, 44:563–596, 2012.

D. Kim, A. Mani, and P. Moin. Investigation of bubble formation by breaking waves in turbulent two-phase couette flows. In 30th Symposium on Naval Hydrodynamics, 2014.

M. Kjeldsen, R. E. A. Arndt, and M. Effertz. Spectral characteristics of sheet/cloud cavitation. Journal of Fluids Engineering, 122(3):481–487, 2000.

T. Kobayashi, T. Kawaguchi, and M. Maeda. Measurement of spray flow by an improved interferometric laser imaging droplet sizing (ILIDS) system. In 10th International Symposium on the Application of Laser Techniques to Fluid Mechanics, Lisbon, Portugal, paper, volume 10, 2000.

G. König, K. Anders, and A. Frohn. A new light-scattering technique to measure the diameter of periodically generated moving droplets. Journal of aerosol science, 17(2): 157–167, 1986.

G. Lacagnina, S. Grizzi, M. Falchi, F. Di Felice, and G. P. Romano. Simultaneous size and velocity measurements of cavitating microbubbles using interferometric laser imaging. Experiments in fluids, 50(4):1153–1167, 2011.

D. Lebrun, D. Allano, L. Méès, F. Walle, F. Corbin, R. Boucheron, and D. Fréchou. Size measurement of bubbles in a cavitation tunnel by digital in-line holography. Applied optics, 50(34):H1–H9, 2011.

Y. Lecoffre. Cavitation: bubble trackers. CRC Press, 1999.

Y. Lecoffre, P. Chantrel, and J. Teiller. Le Grand Tunnel Hydrodynamique (GTH): France's New Large Cavitation Tunnel for Hydrodynamics Research. In International Symposium on Cavitation Research Facilities and Techniques, pages 13–18, 1987.

A. T. Leger, L. P. Bernal, and S. L. Ceccio. Examination of the flow near the leading edge of attached cavitation. part 2. incipient breakdown of two-dimensional and axisymmetric cavities. Journal of Fluid Mechanics, 376:91–113, 1998.

J. Li, B. Yuan, and P. M. Carrica. Modeling bubble entrainment and transport for ship wakes: Progress using hybrid rans/les methods. Journal of Ship Research, 2019.

Y. Liao and D. Lucas. A literature review of theoretical models for drop and bubble breakup in turbulent dispersions. Chemical Engineering Science, 64(15):3389–3406, 2009.

Y. Liao and D. Lucas. A literature review on mechanisms and models for the coalescence process of fluid particles. Chemical Engineering Science, 65(10):2851–2864, 2010.

H. Lindgren. Cavitation inception on head forms ittc comparative experiments. In Swedish State Shipbuilding Experimental Tank, Göteborg, Sweden, Proceedings of the 11th International Towing Tank Conference, ITTC'66, Tokyo, Japan, Subject Performance, pp. 219-233. Paper: P1966-4 Proceedings., 1966.

Z. Liu and C. E. Brennen. Cavitation nuclei population and event rates. Journal of fluids engineering, 120(4):728–737, 1998.

Z. Liu, K. Sato, and C. E. Brennen. Cavitation nuclei population dynamics in a water tunnel. In ASME, number 153, pages 119–124. American Society of Mechanical Engineers, 1993.

J. Ma, C.-T. Hsiao, and T. Chahine G. A physics based multiscale modeling of cavitating flows. Computers & Fluids, 145:68 – 84, 2017. ISSN 0045-7930. doi: https://doi.org/10.1016/j.compfluid.2016.12.010. URL http://www.sciencedirect.com/science/article/pii/S0045793016303930.

M. Maeda. Laser holography measurement of bubble population in cavitation cloud on a foil section. Cavitation 91, ASME, FED, 116:67, 1991.

M. Maeda, T. Kawaguchi, and K. Hishida. Novel interferometric measurement of size and velocity distributions of spherical particles in fluid flows. Measurement Science and Technology, 11(12):L13, 2000. ISSN 0957-0233. URL http://stacks.iop.org/0957-0233/11/i=12/a=101.

N. Masnadi, M. A. Erinin, N. Washuta, F. Nasiri, E. Balaras, and J. H. Duncan. Air entrainment and surface fluctuations in a turbulent ship hull boundary layer. Journal of Ship Research, 2019.

C. Mätzler. Matlab functions for mie scattering and absorption, version 2. IAP Res. Rep, 8(1):9, 2002.

I. M. Mazzitelli, D. Lohse, and F. Toschi. The effect of microbubbles on developed turbulence. Physics of fluids, 15(1):L5–L8, 2003.

L. Mées, D. Lebrun, D. Allano, F. Walle, Y. Lecoffre, R. Boucheron, and D. Fréchou. Development of interferometric techniques for nuclei size measurement in cavitation tunnel. In Proceedings of the 28th Symposium on Naval Hydrodynamics, 2010.

R. S. Meyer, M. L. Billet, and J. W. Holl. Freestream nuclei and traveling-bubble cavitation. Journal of fluids engineering, 114(4):672–679, 1992.

K. Mørch. Cavitation inception from bubble nuclei. Interface Focus, 5(5), 2015.

C. Mounaïm-Rousselle and O. Pajot. Droplet sizing by mie scattering interferometry in a spark ignition engine. Particle & Particle Systems Characterization: Measurement and Description of Particle Properties and Behavior in Powders and Other Disperse Systems, 16(4):160–168, 1999.

S. Nagaya, R. Kimoto, K. Naganuma, and T. Mori. Observation and scaling of tip vortex cavitation on elliptical hydrofoils. In ASME-JSME-KSME 2011 Joint Fluids Engineering Conference, pages 225–230. American Society of Mechanical Engineers Digital Collection, 2011.

T. O'Hern, L. d'Agostino, and A. Acosta. Comparison of holographic and coulter counter measurements of cavitation nuclei in the ocean. Journal of Fluids Engineering, 110(2): 200–207, 1988.

T. J. O'Hern. Cavitation inception scale effects: I. Nuclei distributions in natural waters. II. Cavitation inception in a turbulent shear flow. PhD thesis, California Institute of Technology, 1987.

J. Park and W. Seong. Experimental study on the effect of number of bubble occurrences on tip vortex cavitation noise scaling law. Journal of Fluids Engineering, 139(6):061303, 2017.

S. Pu. Developpement de methodes interferometriques pour la caracterisation des champs de particules. Thesis, Rouen, 2005.

D. Qian, J. McLaughlin, K. Sankaranarayanan, S. Sundaresan, and K. Kontomaris. Simulation of bubble breakup dynamics in homogeneous turbulence. Chemical Engineering Communications, 193(8):1038–1063, 2006.

L. Qieni, W. Xiang, L. Tong, L. Zhen, and Z. Yimo. Linear interferometric image processing for analysis of a particle in a volume. Journal of Optics, 16(4):045703, 2014. ISSN 2040-8986. URL `http://stacks.iop.org/2040-8986/16/i=4/a=045703`.

Q. Qin, C. C. Song, and R. E. Arndt. A numerical study of the unsteady turbulent wake behind a cavitating hydrofoil. Bulletin of the American Physical Society, 48(10):107, 2003a.

Q. Qin, C. C. Song, and R. E. Arndt. Incondensable gas effect on turbulent wake behind a cavitating hydrofoil. In The 5th International Symposium on Cavitation, Osaka, Japan, 2003b.

A. Quérel, P. Lemaitre, M. Brunel, E. Porcheron, and G. Gréhan. Real-time global interferometric laser imaging for the droplet sizing (ILIDS) algorithm for airborne research. Measurement Science and Technology, 21(1):015306, 2010. ISSN 0957-0233. URL `http://stacks.iop.org/0957-0233/21/i=1/a=015306`.

B. Ran and J. Katz. Pressure fluctuations and their effect on cavitation inception within water jets. Journal of Fluid Mechanics, 262:223–263, 1994.

K. Randolph, H. M. Dierssen, M. Twardowski, A. Cifuentes-Lorenzen, and C. J. Zappa. Optical measurements of small deeply penetrating bubble populations generated by breaking waves in the southern ocean. Journal of Geophysical Research: Oceans, 119 (2):757–776, 2014.

P. S. Russell, D. R. Giosio, J. A. Venning, B. W. Pearce, P. A. Brandner, and S. L. Ceccio. Microbubble generation from condensation and turbulent breakup of sheet cavitation. In 31st Symposium on Naval Hydrodynamics, Monterey, California, 2016.

P. S. Russell, J. A. Venning, P. A. Brandner, B. W. Pearce, D. R. Giosio, and S. Ceccio. Microbubble disperse flow about a lifting surface. In 32nd Symposium of Naval Hydrodynamics, Hamburg Germany, 2018.

P. S. Russell, L. Barbaca, J. A. Venning, B. W. Pearce, and P. A. Brandner. Measurement of nuclei seeding in hydrodynamic test facilities. Experiments in Fluids, 61(79), 2020a. doi: https://doi.org/10.1007/s00348-020-2911-2.

P. S. Russell, J. A. Venning, B. W. Pearce, and P. A. Brandner. Calibration of mie scattering imaging for microbubble measurement in hydrodynamic test facilities. Experiments in Fluids, 61(93), 2020b. doi: https://doi.org/10.1007/s00348-020-2927-7.

N. Semidetnov and C. Tropea. Conversion relationships for multidimensional particle sizing techniques. Measurement Science and Technology, 15(1):112, 2003.

M. P. L. Sentis, F. R. A. Onofri, L. Mées, and S. Radev. Scattering of light by large bubbles: Coupling of geometrical and physical optics approximations. Journal of Quantitative Spectroscopy and Radiative Transfer, 170:8–18, 2016. ISSN 0022-4073. doi: https://doi.org/10.1016/j.jqsrt.2015.10.007. URL `http://www.sciencedirect.com/science/article/pii/S0022407315300650`.

G. S. Settles. Schlieren and shadowgraph techniques: visualizing phenomena in transparent media. Springer Science & Business Media, 2012.

H. Shen, S. Coetmellec, and M. Brunel. Simultaneous 3D location and size measurement of spherical bubbles using cylindrical interferometric out-of-focus imaging. Journal of Quantitative Spectroscopy and Radiative Transfer, 131:153–159, 2013. ISSN 0022-4073. doi: https://doi.org/10.1016/j.jqsrt.2013.04.009. URL `http://www.sciencedirect.com/science/article/pii/S0022407313001441`.

S. M. Skippon and Y. Tagaki. ILIDS measurements of the evaporation of fuel droplets during the intake and compression strokes in a firing lean burn engine. SAE transactions, pages 1111–1126, 1996.

R. Smith and R. Peterson. Dynamic and diffusive growth of microbubbles near a two-dimensional hydrofoil. IEEE journal of oceanic engineering, 9(2):93–97, 1984.

H. Takahira. Growth of traveling bubbles near an axisymmetric body in a potential flow. JSME International Journal Series B Fluids and Thermal Engineering, 40(2):240–249, 1997.

E. J. Terrill, W. K. Melville, and D. Stramski. Bubble entrainment by breaking waves and their influence on optical scattering in the upper ocean. Journal of Geophysical Research: Oceans, 106(C8):16815–16823, 2001.

C. Tropea. Optical particle characterization in flows. Annual Review of Fluid Mechanics, 43:399–426, 2011.

M. C. Trump, K. L. De Graaf, B. W. Pearce, and P. A. Brandner. An experimental investigation of the optical measurement of microbubbles in a confined radial jet. In 7th Australian Conference on Laser Diagnostics in Fluid Mechanics and Combustion, pages 29–34, 2015.

M. X. Van Rijsbergen and T. J. C. Van Terwisga. High-speed micro-scale observations of nuclei-induced sheet cavitation. In WIMRC 3rd international cavitation forum, pages 4–6, 2011.

J. Vejražka, M. Zedníková, and P. Stanovskỳ. Experiments on breakup of bubbles in a turbulent flow. AIChE Journal, 64(2):740–757, 2018.

J. Venning, S. Smith, P. Brandner, D. Giosio, and B. Pearce. The influence of nuclei content on cloud cavitation about a hydrofoil. In 17th International Symposium on Transport Phenomena and Dynamics of Rotating Machinery, pages 1–6, 2017.

J. A. Venning, M. T. Khoo, B. W. Pearce, and P. A. Brandner. Background nuclei measurements and implications for cavitation inception in hydrodynamic test facilities. Experiments in Fluids, 59(4):71, 2018.

T. A. Waniewski, C. E. Brennen, and F. Raichlen. Measurements of air entrainment by bow waves. J. Fluids Eng., 123(1):57–63, 2000.

N. Washuta, N. Masnadi, and J. H. Duncan. The turbulent boundary layer on a horizontally moving, partially submerged, surface-piercing vertical wall. arXiv preprint arXiv:1606.05035, 2016.

E. Weitendorf, J. Friesch, and C. Song. Considerations for the New Hydrodynamics and Cavitation Tunnel (HYKAT) of the Hamburg Ship Model Basin (HSVA). In Int'l. Symposium on Cavitation Research Facilities and Techniques, ASME, New York, NY, 1987.

R. Xu. Particle characterization: light scattering methods, volume 13. Springer Science & Business Media, 2001.

P.-W. Yu and S. L. Ceccio. Diffusion induced bubble populations downstream of a partial cavity. Journal of fluids Engineering, 119(4):782–787, 1997.

L. Zhang, L. Chen, and X. Shao. The migration and growth of nuclei in an ideal vortex flow. Physics of Fluids, 28(12):123305, 2016.

Appendices

Appendix A

Towards Real-time Optical Measurement of Microbubble Content in Hydrodynamic Test Facilities

This paper was presented at the (peer-reviewed) 16^{th} *International Symposium on Cavitation*, Baltimore, Maryland, US, 14-16 May 2018.

The citation for the conference paper is:

Russell, P. S., Giosio, D. R., Venning, J. A., Pearce, B. W., Brandner, P. A., Aumelas, V., and Maj, G., (2018). Towards real-time optical measurement of microbubble content in hydrodynamic test facilities. *In 10th Symposium on Cavitation (CAV2018)* (pp. 1056-1061).

Towards real-time optical measurement of microbubble content in hydrodynamic test facilities

[1]Patrick S. Russell*; [1]Dean R. Giosio; [1]James A. Venning; [1]Bryce W. Pearce; [1]Paul A. Brandner
V. Aumelas[2] and G. Maj[2]

[1]Cavitation Research Laboratory, University of Tasmania, Launceston, Tasmania, Australia
[2]YLEC Consultants, Grenoble, France

Abstract

Real-time measurement of microbubble concentrations is desirable in order to inform experimental results, particularly in studies of cavitation physics. To develop these capabilities a controlled experiment using a micro-fluidic T-junction to produce mono-disperse microbubbles was devised with the size and frequency of microbubbles measured using a line-scan camera capable of acquiring 45k images per second. Measurements were able to be obtained and reported in under 3 seconds from the triggering time. Tests were carried out in quiescent water and implementation in non-stationary environments would extend the operational range. The principal operating mode produced microbubbles on the order of 80 to 130 µm in size at frequencies ranging from 750 to 3200 bubbles per second across the range of air and water pressures tested.

Keywords: microbubbles; cavitation

Introduction

Even small concentrations of microbubbles present within a fluid can greatly impact upon its mechanical properties. In particular the inception of cavitation inside facilities and on board vessels is often controlled by the largest microbubble which will pass through a region of low pressure. Consequently, real-time measurement of these concentrations is desirable in order to inform predicted performance and experimental results.

In hydrodynamic flows of practical interest cavitation nucleation is invariably heterogeneous where microbubbles entrained in the flow or ejected from surface hydrophobic crevices provide sites of weakness, or nuclei, for the initiation of phase change from liquid to vapour [1, 2]. The equilibrium of a microbubble becomes unstable below a critical pressure, depending on its diameter, after which it will grow explosively. Once activated bubbles fill with vapour and interact with the surrounding stationary or flowing liquid developing into macroscopic cavitation phenomena. Rigorous experimental modelling of the inception and dynamics of hydrodynamic cavitation in water tunnels thus requires control and measurement of the microbubble population. The variable pressure water (cavitation) tunnel within the Cavitation Research Laboratory (CRL) at the Australian Maritime College has been developed with ancillary systems for continuous artificial seeding and removal of microbubbles to provide controlled nuclei populations in the test flow [3, 4]. To date this capability has been developed using direct or dilute injection of poly-disperse microbubble populations generated through the rapid de-pressurisation and cavitation of supersaturated water [5]. Whilst poly-disperse populations (typically 10 to 100 µm in diameter) are always required to model real flows the use of mono-disperse nuclei provides several advantages for basic research and for comparative experimental and computational work.

Microfluidic or lab-on-chip devices have been developed for mono-disperse generation of micro, or nano-bubble populations for sono-fluidic or sono-chemical processes such as contrast agents or drug delivery vectors in medical applications [6]. These devices typically generate smaller bubbles than those suitable for nuclei and may involve the use of surfactants [7]. Commercial devices using common materials and simple experimental set-ups generating microbubbles of order 10 to 100 µm at rates of order 10^3 to 10^4 have been developed by YLEC Consultants, France. The present work is a collaboration between the CRL and YLEC Consultants to investigate the operational range and use of these devices for mono-disperse cavitation nuclei seeding.

*Corresponding Author, Patrick Russell: Patrick.Russell@utas.edu.au

To characterise such devices, or measure populations within the CRL hydrodynamic test facility long range microscopy-shadowgraphy is typically used. With the use of PIV cameras and dual pulse lasers bubble velocities may also be measured. However, the processing of these high resolution image pairs is demanding such that results can not, at present, be obtained in real-time. To address this problem a line-scan camera with a single row of densely spaced pixels was used. The reduced number of pixels allowed the acquisition speed of the camera to be high and the spatial resolution to be increased from standard PIV cameras in one dimension at the sacrifice of the second spatial dimension. When stacked these line measurements produce a space-time plot from which size and frequency information is readily extracted.

Experimental overview

The L10 device from Ylec Consultants was mounted within a quiescent tank at atmospheric pressure and supplied by independently pressurised air and water lines. The size and frequency of bubbles produced was dependent on the balance of these pressures. The device was deemed to be in its principal operating mode when the standard deviation of the bubble size was 10% of the measured mean, with a single production frequency.

The T-junction device was tested in a 0.05 m square acrylic tank filled with distilled water. The junction was fitted through the base of the tank on a mount to which was connected the 4 mm pressurised air and water supply lines. Air pressure was regulated then conditioned through a 1.0 µm filter before it reached the device. Water was supplied from a reservoir of distilled water pressurised by air connected to a second regulator. Water and air pressures ranging between 1.5 and 7 bar absolute in 0.5 bar increments were tested, measured using two Siemens Sitrans P DS III, Range: 0-500 kPa, Model number: 7MF4333-1GA02-2AB1 absolute pressure transducers. These were connected to a National Instruments 6366 USB-DAQ which sampled the pressures for 1 second during image acquisition at a rate of 1000 Hz. The mean and standard deviation of these measurements were recorded. The standard deviation of all pressure measurements was below 0.01 bar and the mean within 0.05 bar of the nominal pressure.

Bubbles were illuminated using a Constellation 120 W white 5600K LED light positioned directly behind the acrylic tank. Images were captured using a Teledyne DALSA Linea Mono linescan camera with 8192$\times$1 pixel resolution. The single line of pixels was sampled 10000 times at a rate of 45 kHz. These rows of pixels when stacked produced a space-time plot which was recorded on board the camera and then transmitted as a single frame to MATLAB for processing. The camera was coupled to a Questar QM100 long-range microscope using a 1.5$\times$ Barlow lens then bellows giving a field of view of approx 900 µm with a spatial resolution of 0.121 µm/pixel. A schematic of the overall experimental set-up is shown in figure 1. For each condition 4 ensemble images were collected and processed separately. All data is presented as the mean of these measurements with error bars of two standard deviations applied where appropriate.

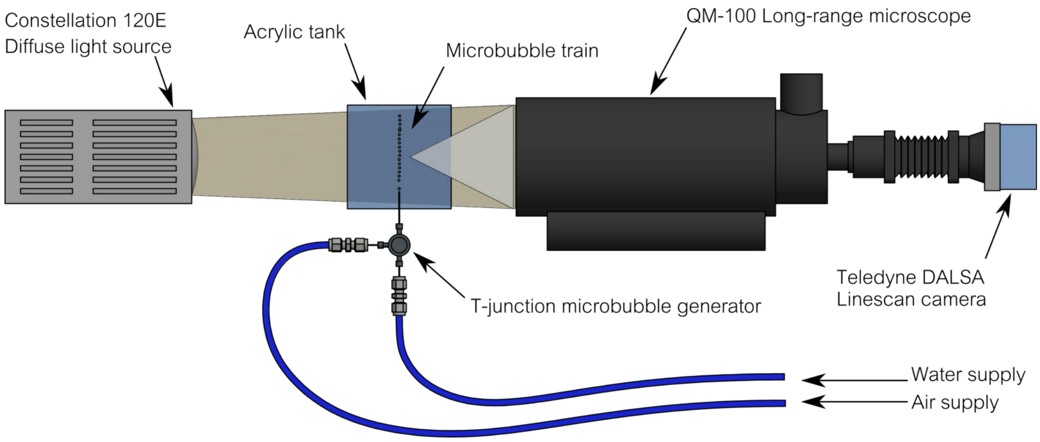

Figure 1: Schematic of experimental setup for the measurement of microbubble size and production rate using shadowgraphy

*Corresponding Author, Patrick Russell: Patrick.Russell@utas.edu.au

Processing method

A small portion of an image frame is shown in figure 2. Images were acquired using the MATLAB image acquisition toolbox. Once in MATLAB each row of pixels was summed together to create a time series of integral intensity. Peaks extracted from the series correspond to the passage of a bubble through the measurement area. The single row of pixels corresponding to the maximum of each peak was extracted and the diameter of the bubble calculated via thresholding of the smoothed pixel intensity. Two methods were used to collect bubble production frequency. The first was extracted from the fast Fourier transform (FFT) of the intensity time series. In periodic production regimes this was sufficient to assess production frequency. As the device reached the limits of its operating envelope the size and frequency of the bubble produced fluctuated. The second method simply estimated the integral production frequency by dividing the number of bubbles observed in the intensity time series by the length of the sample. Comparison of this frequency estimate with the peak frequency observed in the FFT of the series allowed immediate determination of when the device was operating in its intended manner. Table 1 shows a summary of the differences between these frequencies. Large numbers signalled that the device was no longer producing mono-disperse bubbles.

Frequency Difference	Δf (hz)	p_{air} (bar)											
		1.5	**2.0**	**2.5**	**3.0**	**3.5**	**4.0**	**4.5**	**5.0**	**5.5**	**6.0**	**6.5**	**7.0**
p_{water} (bar)	**1.5**	-	-	-	-	-	-	-	-	-	-	-	-
	2.0	-	-	-	-	-	-	-	-	-	-	-	-
	2.5	-	-	-	-	-	-	-	-	-	-	-	-
	3.0	-	-	-	-	1	2	3	1	3	776	-	-
	3.5	-	-	77	1	1	0	1	1	1083	68	-	-
	4.0	-	-	116	2	2	1	3	2	3	378	-	-
	4.5	-	26	3	13	2	1	1	1	2	2	2	-
	5.0	-	-	-	1	0	1	3	1	373	17	594	-
	5.5	-	-	-	633	1	1	0	2	37	1723	1334	-
	6.0	-	-	-	-	-	-	1	5	15	1	21	897

Table 1: For each condition the table shows the absolute difference (in Hz) between two measures of the production frequency. The first measure uses the dominant bubble production frequency from largest peak in the FFT of pixel row intensity. The second measure of frequency is gathered by dividing the total number of bubbles observed over the acquisition time. Large values in this table indicates that the device was operating outside the intended principal operating mode. Conditions whose frequency measures are in agreement, $\Delta f < 50\ Hz$, have been highlighted in blue. A difference in frequency greater than 50 Hz is marked in red. A dash indicates that for this pressure combination the device either did not produce bubbles or was not tested.

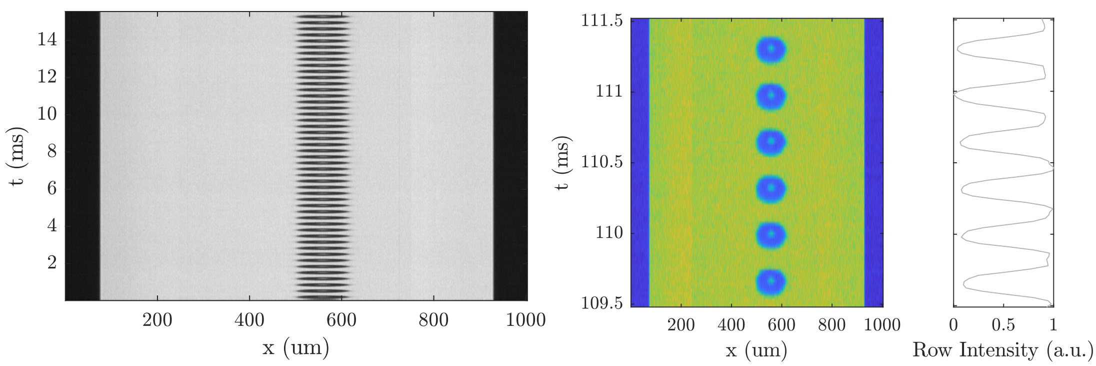

Figure 2: A sample image (left) - $p_{air} = 5$ bar, $p_{water} = 4.5$ bar - showing 700 lines from the line-scan camera. Here the vertical axis is time, with spatial coordinates on the horizontal axis to produce a space time plot. A portion of the regular stream of similarly sized bubbles observed in the image has been enlarged and stretched (centre). Each row of pixels in this centre image has been summed and non-dimensionalised by the minimum and maximum value of the overall series to produce the plotted row intensity time series (right). This time series is used to detect bubbles and find the centre location of each bubble for sizing.

*Corresponding Author, Patrick Russell: Patrick.Russell@utas.edu.au

Results

The range of the principal operating mode can be established from examination of Table 1. For convenience the pressure ratio is defined with the air pressure as the numerator. It was observed that a pressure ratio near unity is required to remain inside the principal operating mode. The device remained stable over the largest range when an air pressure of 3-5 bar(abs) was used. At low pressure ratios there was a rapid cessation of production with the device simply ejecting water upon exceeding the critical ratio. In contrast, the breakdown of consistent production at high ratios was more subtle. The device would continue to operate but sporadically shift in and out of periodic production into a chaotic production mode. Qualitatively it was observed that this transition is often due to the disturbances created by coalescence further up in the bubble train, however this is not revealed in the data presented here.

With the conditions of interest established, the relevant data was plotted in terms of the size and frequency in figure 3. Naturally, lower air pressures produced smaller bubbles. Lower air pressures also produced bubbles at lower frequencies. As water pressure increased the bubble size reduced and the production frequency increased. This indicates bubble pinch-off occurred quicker inside the junction at these pressures. The largest bubbles of consistent size were 133 µm in diameter, produced at an air pressure of 5 bar and water pressure of 4 bar. While the smallest bubble size was approximately 70 µm, the two conditions where this size was observed were very close to device breakdown ($p_{Air} = 3$ bar, $p_{water} = 5.5$ bar & $p_{air} = 5$ bar, $p_{water} = 6$ bar). The smallest stable condition then was 83 µm at an air pressure of 3 bar and water pressure of 5 bar.

Bubble production rates were of order 10^3 to 10^4 bubbles per second. In contrast to bubble diameter production frequency increased with water pressure but also with air pressure. The lowest production frequency was 770 Hz ($p_{air} = 3$ bar, $p_{water} = 3.5$ bar), while the highest consistent frequency was 3200 Hz ($p_{air} = 5$ bar, $p_{water} = 5.5$ bar). Higher, stable, mono-disperse production frequencies were achieved, but they were very close to device breakdown and could not be repeated when the combination was later re-tested. Further extreme cases were found that produced bubbles outside of these size and frequency bounds but they were either inconsistent or likely to disappear during testing.

A plane was fitted through the size data as a function of water and air pressure.

$$Size(p_{air}, p_{water}) = 110 + 13.4\ p_{air} - 13.83\ p_{water} \quad (\mu m) \tag{1}$$

In equation form it is clear that the mean bubble size produced was 110 µm and that variation of water and air have similar influence but opposite effects. The size reduced or increased by approximately 13.5 µm as the difference between these two pressures increases by 1 bar.

The adjusted R-squared residual of this fit was 0.76. Consequently approximately 24% variation in the size was left unexplained. This result is not as strong as would be desired. To improve this result, due to the speed with which measurements may be collected, electronically controlled pressure regulators could be used to conduct a more detailed sweep with increased repetition of tests. However, before testing it was assumed that the device was operating independent of its supply pressure history. Observations during testing indicate that this may not be true across short time periods at all conditions. Acquisition of samples were slowed to give time for these effects to decay - approximately 2 minutes for each pressure combination - but this effect may have contributed to errors observed here. The cause for this effect may lie in the pressure supply system. Detailed tracking of the evolving production characteristics following large pressure changes is to be conducted and compared to the supply pressure measurements in time.

Conclusion

Bubble sizes were measured using a linescan camera to collect size and frequency measurements in near real time. Tests were carried out in quiescent water and implementation in non-stationary environments would extend the operational range. However, in this environment the principal operating mode produced microbubbles on the order of 80–130 µm in size at frequencies ranging from 750–3200 bubbles per second were produced across the range of air and water pressures tested. Bubbles near these sizes could be used as seeded cavitation nuclei within hydrodynamic test facilities through dilute or direct injection.

*Corresponding Author, Patrick Russell: Patrick.Russell@utas.edu.au

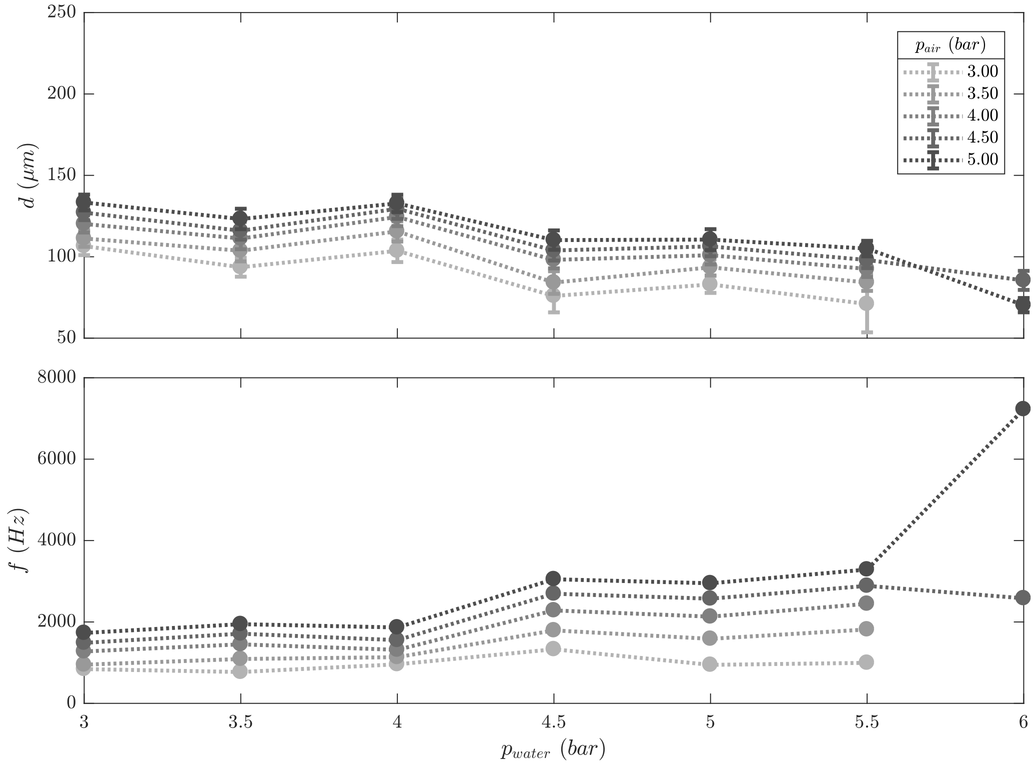

Figure 3: The diameter of bubbles produced (top) decreases as water pressure increases for a constant air supply pressure. Diameters increase with air pressure. Error bars denote two standard deviations. (bottom) Bubble production frequency increases both with air and water pressure.

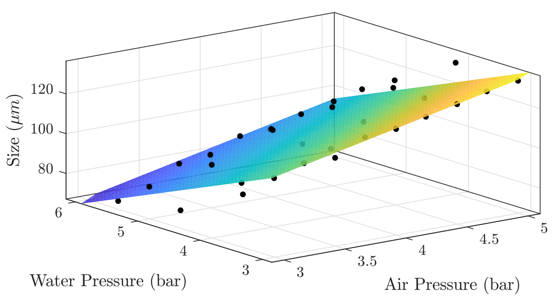

Figure 4: Size is plotted against both air and water supply pressures. A plane of best fit using least square residuals is created though the data.

*Corresponding Author, Patrick Russell: Patrick.Russell@utas.edu.au

Acknowledgements:

This project was supported by the Defence Science and Technology Group (Mr. Brendon Anderson and Dr. David Clarke), the University of Tasmania, and the US Office of Naval Research (Dr. Ki-Han Kim, Program Officer) and ONR Global (Dr. Woei-Min Lin) through NICOP S&T Grant no. N62909-15-1-2019.

References

[1] Christopher E. Brennen. *Cavitation and bubble dynamics*. Cambridge University Press, 2013.

[2] Jean-Pierre Franc and Jean-Marie Michel. *Fundamentals of Cavitation*. Springer Science & Business Media, 2006.

[3] PA Brandner, Y Lecoffre, and GJ Walker. *Development of an Australian National Facility for Cavitation Research*. In Sixth International Symposium on Cavitation, 2006.

[4] P. A. Brandner, Y. Lecoffre, and G. J. Walker. *Design Considerations in the Development of a Modern Cavitation Tunnel*. In 16th Australasian Fluid Mechanics Conference, 2007.

[5] D Giosio, BW Pearce, and PA Brandner. Influence of pressure on microbubble production rate in a confined turbulent jet. In *20th Australasian Fluid Mechanics Conference*, 2016.

[6] Joshua Owen, Paul Rademeyer, Daniel Chung, Qian Cheng, David Holroyd, Constantin Coussios, Peter Friend, Quentin A Pankhurst, and Eleanor Stride. *Magnetic targeting of microbubbles against physiologically relevant flow conditions.* Interface focus, (5), 2015.

[7] Shelley Lynn Anna. *Droplets and Bubbles in Microfluidic Devices*. Annual Review of Fluid Mechanics, 48(1), 2016.

*Corresponding Author, Patrick Russell: Patrick.Russell@utas.edu.au

Appendix B

Additional Photos

Table B.1: The images below have the following conditions in common. For convenience, details of the hydrofoil geometry are repeated here.

Profile	NACA63A015
Planform	Elliptical
Span	200 mm
Chord	120 mm
Angle of Incidence	3.5

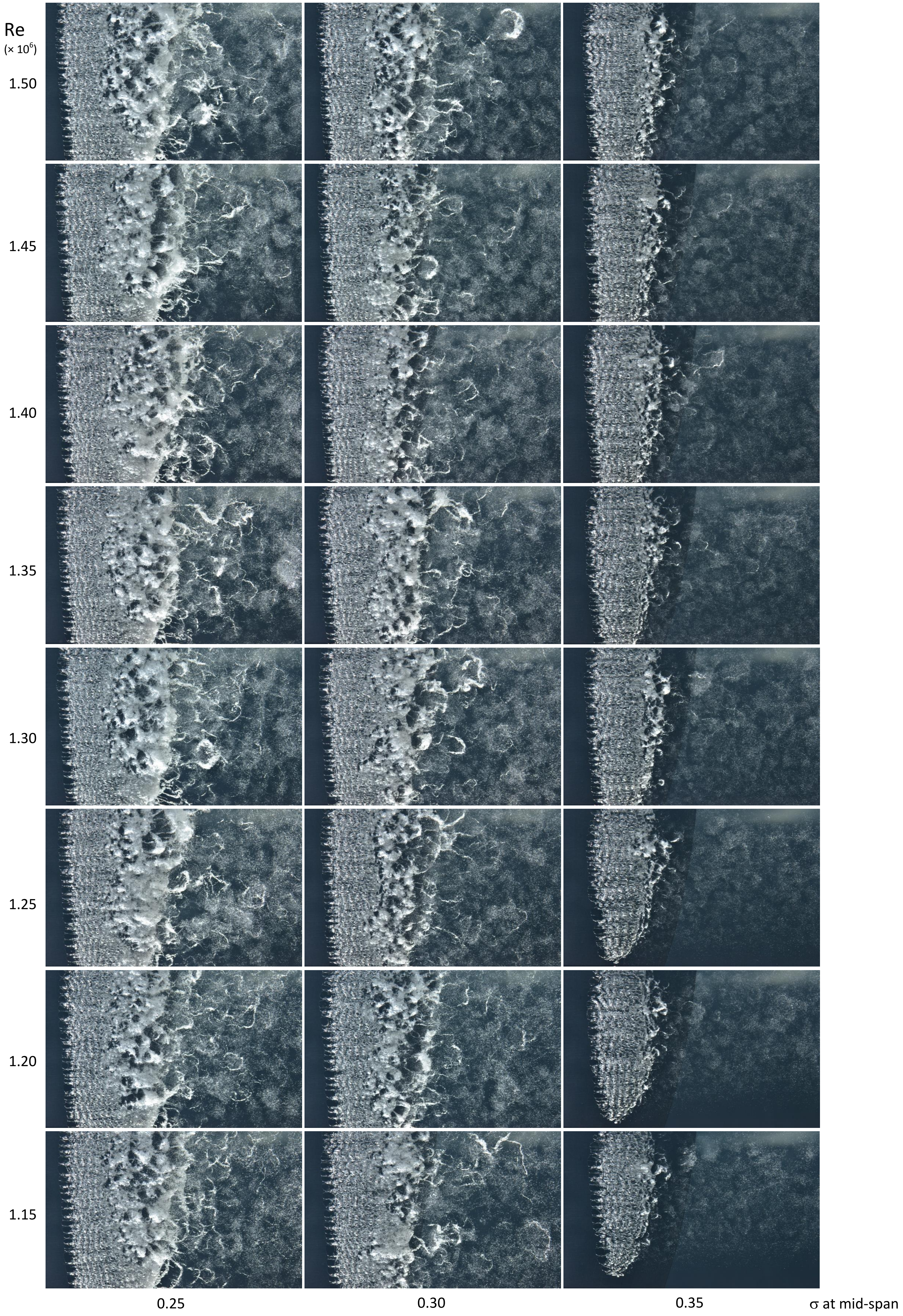
Re
(× 10^6)
1.50
1.45
1.40
1.35
1.30
1.25
1.20
1.15
0.25
0.30
0.35
σ at mid-span

The following select cases where $\sigma_{\text{mid-span}} = 0.25$ are at increased in magnification.

Figure B.1: $Re = 0.60 \times 10^6$

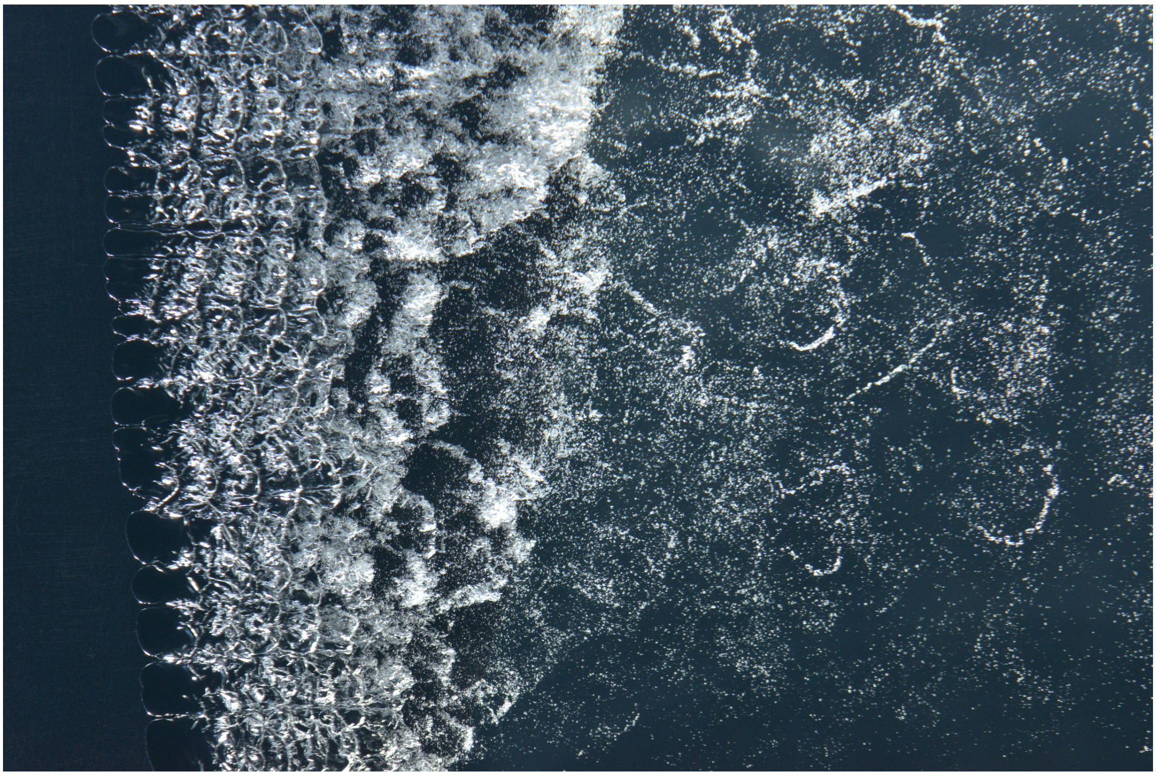

Figure B.2: $Re = 0.70 \times 10^6$

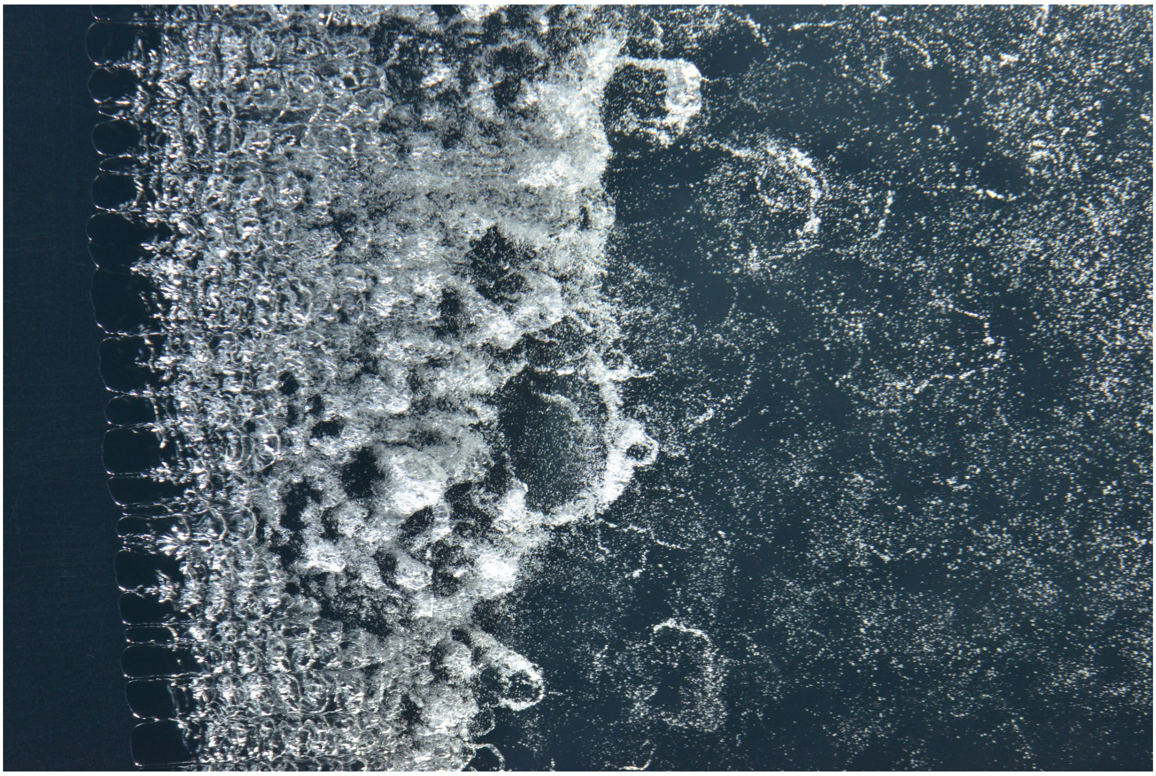

Figure B.3: $Re = 0.80 \times 10^6$

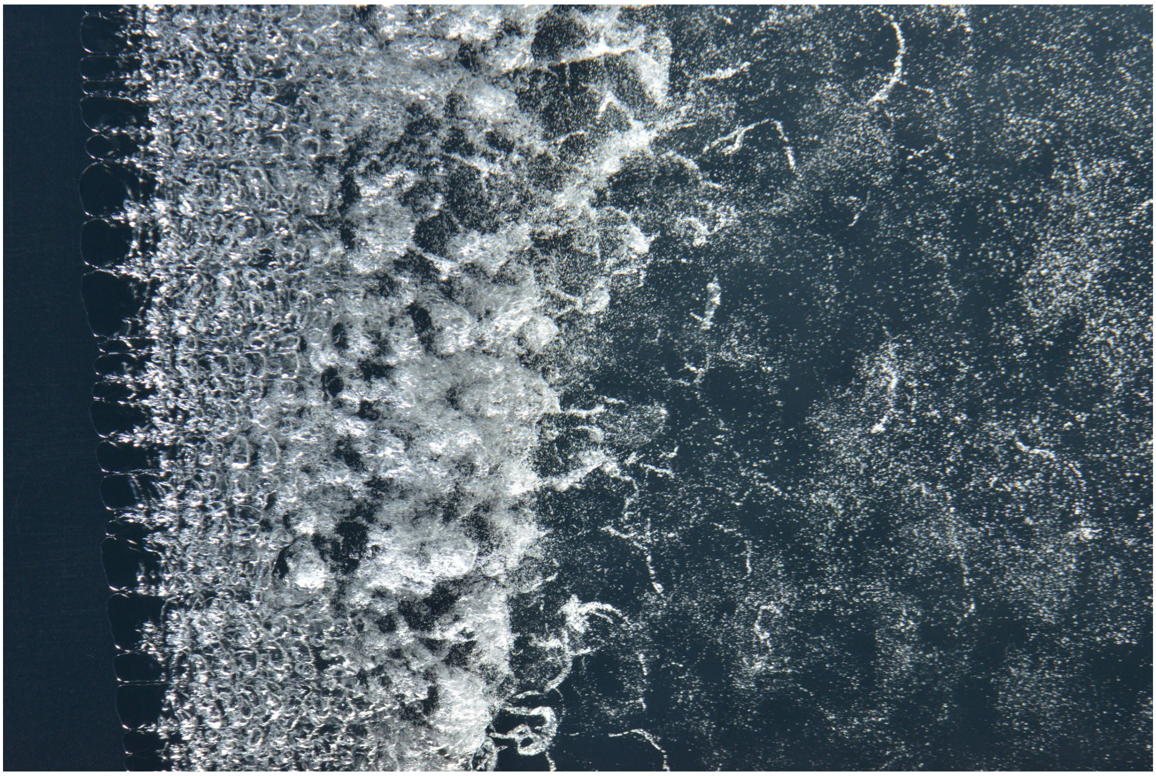

Figure B.4: $Re = 0.90 \times 10^6$

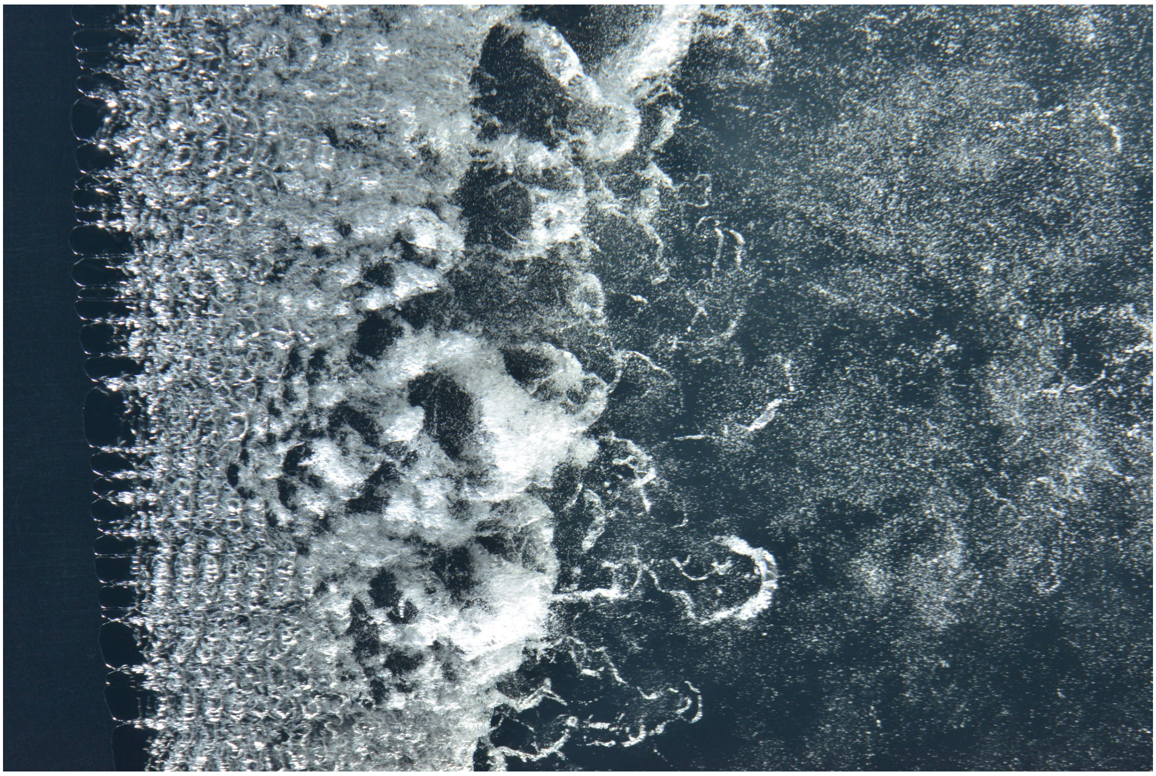

Figure B.5: $Re = 1.05 \times 10^6$

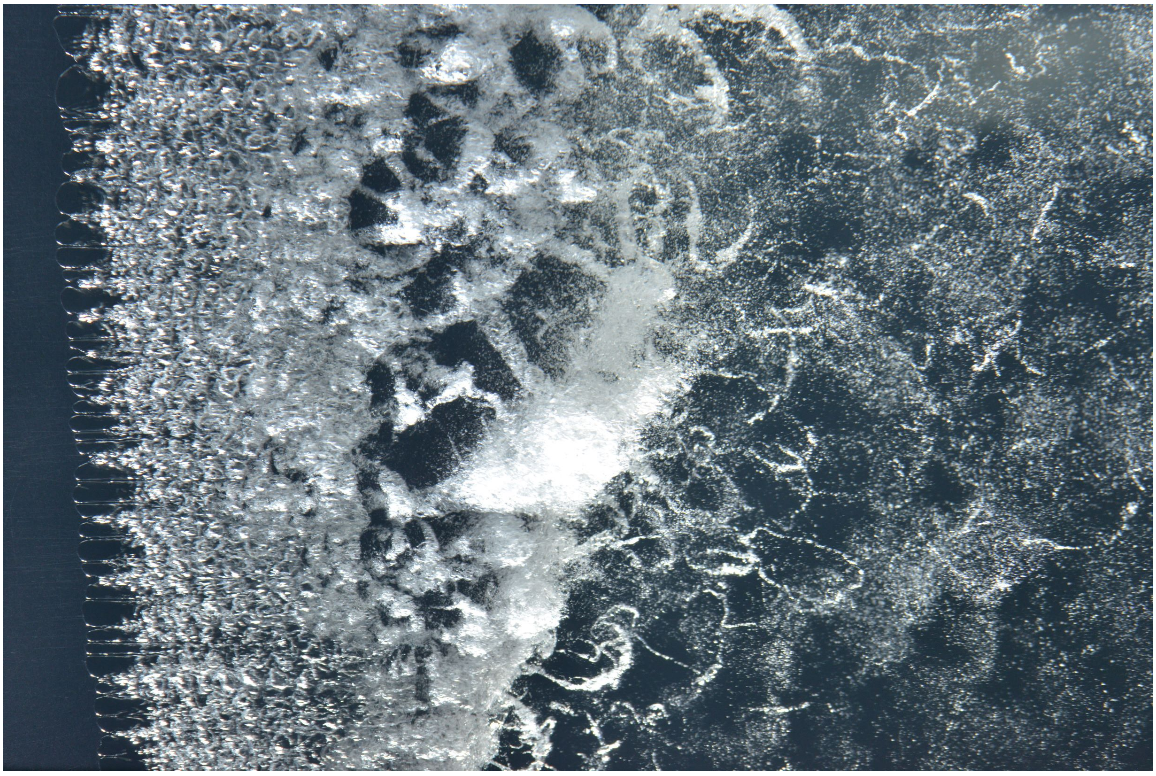

Figure B.6: $Re = 1.15 \times 10^6$

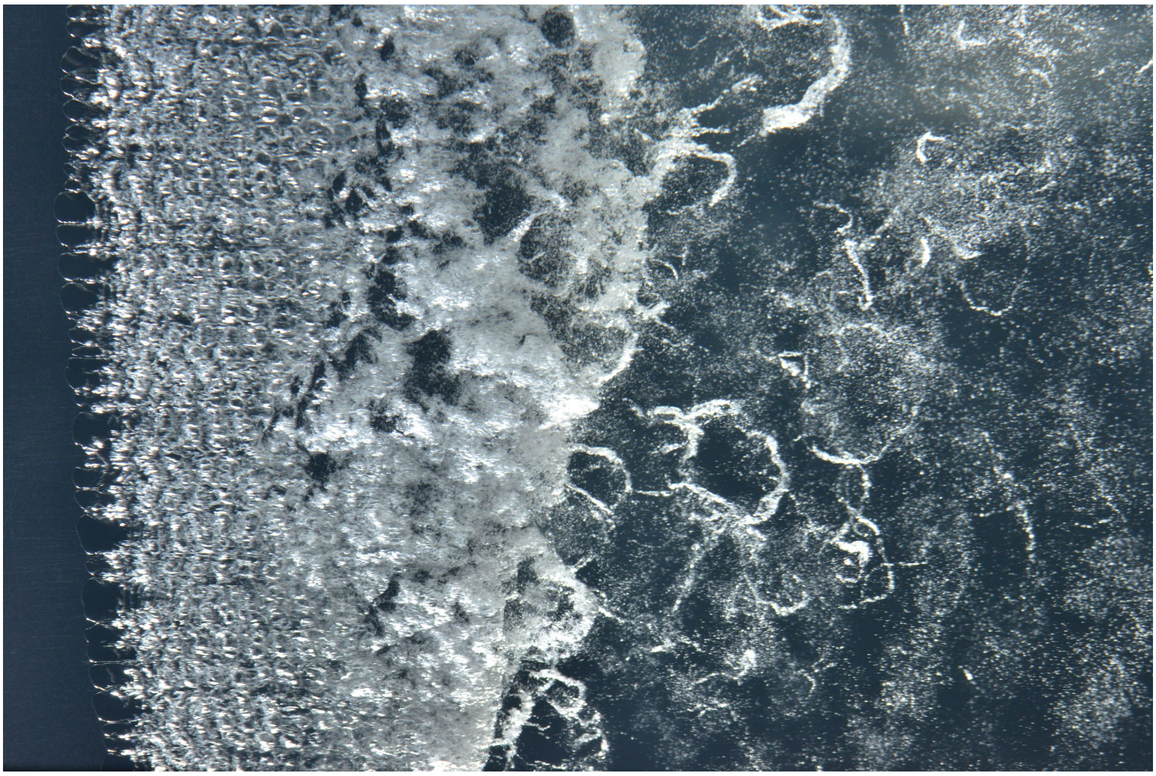

Figure B.7: $Re = 1.20 \times 10^6$

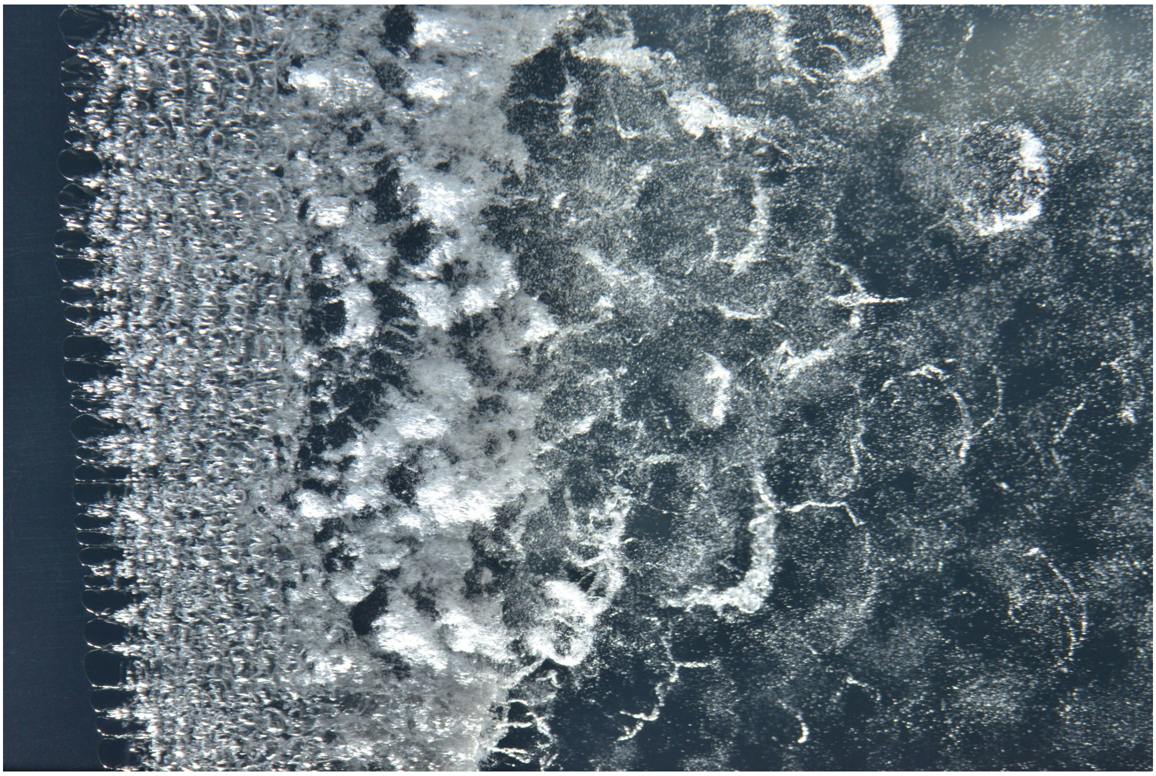

Figure B.8: $Re = 1.25 \times 10^6$

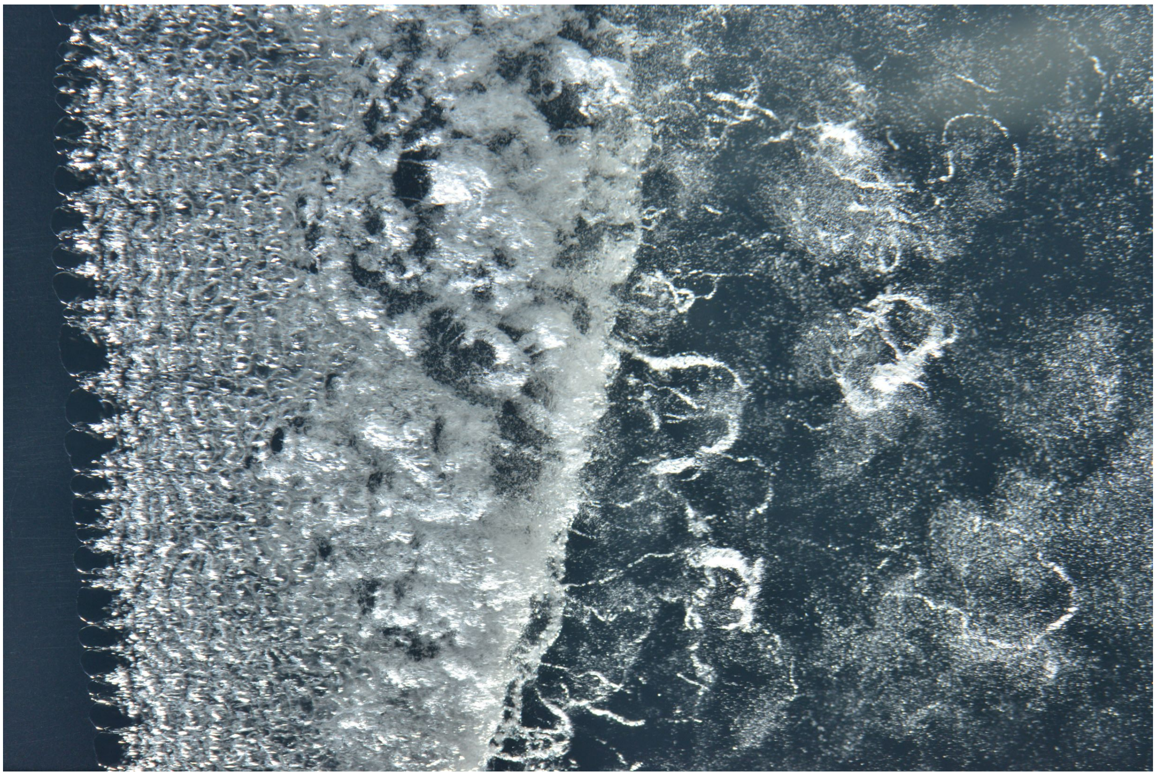

Figure B.9: $Re = 1.30 \times 10^6$

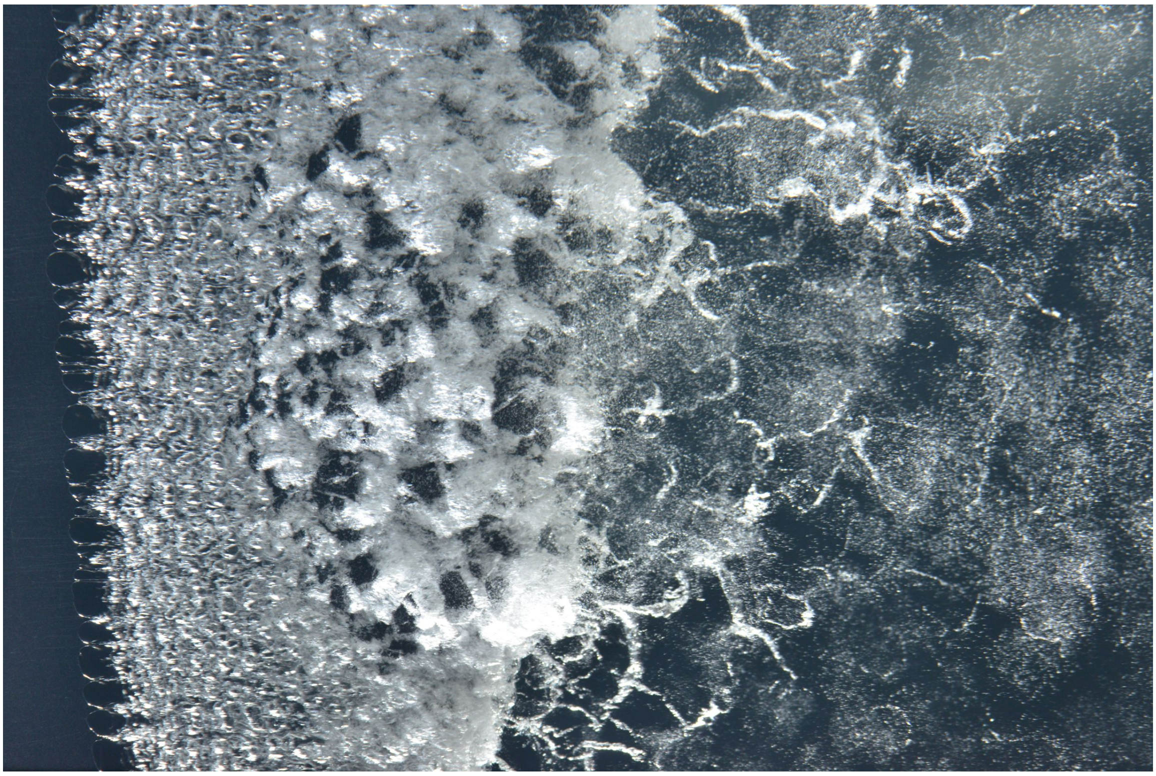

Figure B.10: $Re = 1.35 \times 10^6$

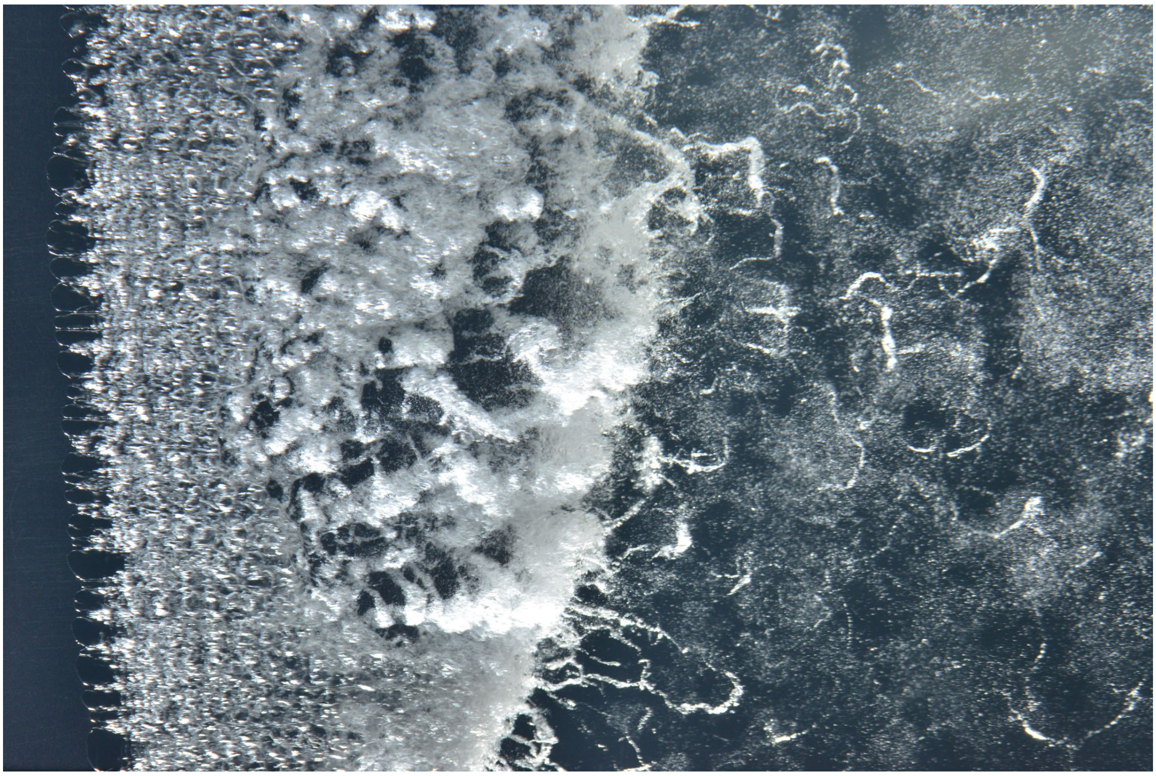

Figure B.11: $Re = 1.40 \times 10^6$

Figure B.12: $Re = 1.45 \times 10^6$

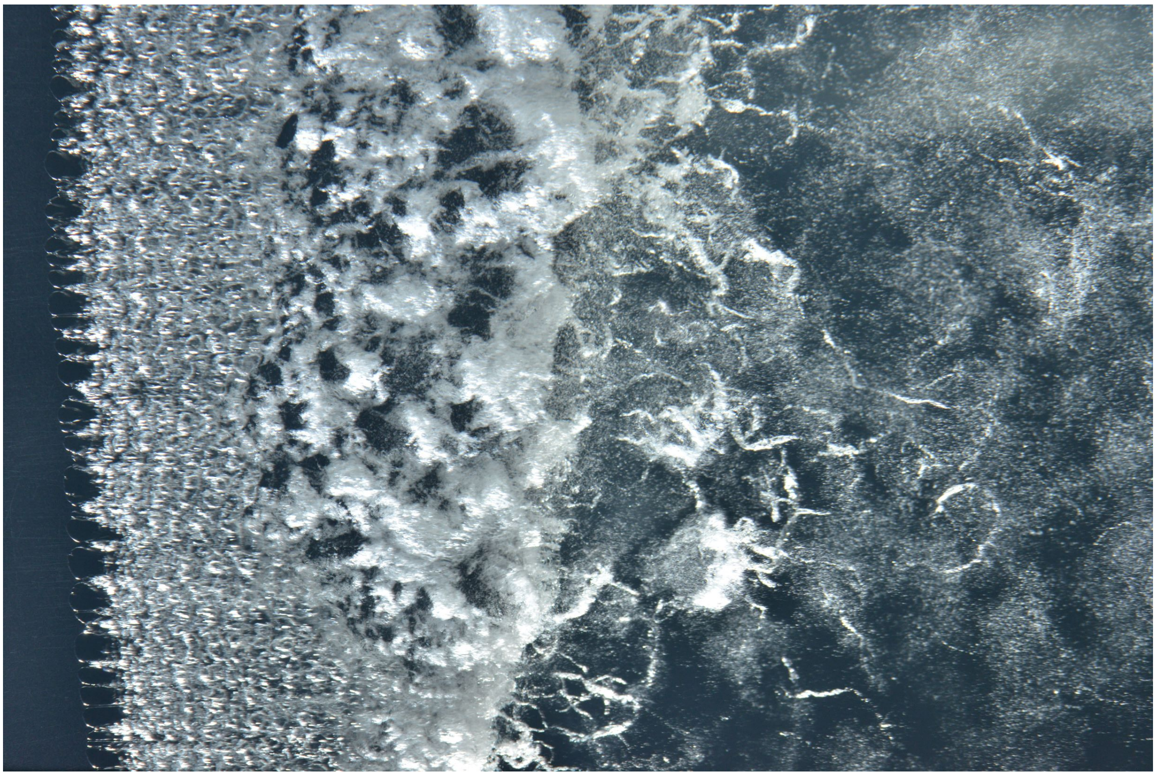

Figure B.13: $Re = 1.50 \times 10^6$